

## A MODEL OF THE 8–25 MICRON POINT SOURCE INFRARED SKY

RICHARD J. WAINSCOAT<sup>1</sup>

NASA Ames Research Center and SETI Institute

MARTIN COHEN<sup>2</sup>Jamieson Science and Engineering Inc., and Radio Astronomy Laboratory,  
University of California, Berkeley

AND

KEVIN VOLK,<sup>3</sup> HELEN J. WALKER,<sup>4</sup> AND DEBORAH E. SCHWARTZ<sup>5</sup>

NASA Ames Research Center and SETI Institute

Received 1991 May 9; accepted 1992 April 29

## CONTENTS

1. Introduction	112	58–D12	3.1. Colors and Luminosity Functions	125	58–E13
2. The Galaxy	113	58–D13	3.2. Low-Resolution Spectrometer Spectra of Galaxies	127	58–F1
2.1. Galactic Structure	113	58–D13	3.3. Integration of Galaxies through Space	128	58–F2
2.1.1. The Exponential Disk	113	58–D13	4. Comparison with Observations and Discussion	128	58–F2
2.1.2. The Bulge	114	58–D14	4.1. Comparison with the PSC	128	58–F2
2.1.3. The Stellar Halo	114	58–D14	4.2. Comparison with the Faint Source Survey	133	58–F7
2.1.4. The Spiral Arms	114	58–D14	4.3. Comparison with the Serendipitous Survey	136	58–F10
2.1.5. The Molecular Ring	115	58–E1	4.4. Comparison with the Deep <i>IRAS</i> Survey	137	58–F11
2.2. Source Tables	115	58–E1	4.5. Comparison with 2.2 Micron Source Counts	137	58–F11
2.2.1. Stars	116	58–E2	4.6. Comparison with <i>V</i> Star Counts at the North Galactic Pole	139	58–F13
2.2.2. Nonstellar Sources	118	58–E4	5. Conclusions	139	58–F13
2.2.3. Synthesized Luminosity Functions	119	58–E5	Appendix. Modeling the Asymptotic Giant Branch Stars	140	58–F14
2.2.4. Normalization	119	58–E5	A1. Parameters from Stellar Evolution Models	140	58–F14
2.3. Low-Resolution Spectrometer Spectra	121	58–E9	A2. The Mass-Loss Formula	141	58–G1
2.3.1. Stars	121	58–E9	A3. Other Observational Constraints	142	58–G2
2.3.2. Galactic Nonstellar Objects	122	58–E10	A4. Parameters of the Models	143	58–G3
2.3.3. Use of Nonstandard Filters	122	58–E10	A5. Results of the Models	143	58–G3
2.4. Interstellar Extinction	122	58–E10			
2.5. Integration through the Galaxy	124	58–E12			
3. The Extragalactic Sky	125	58–E13			

## ABSTRACT

We present a detailed model for the infrared point source sky that comprises geometrically and physically realistic representations of the Galactic disk, bulge, stellar halo, spiral arms (including the “local arm”), molecular ring, and the extragalactic sky. We represent each of the distinct Galactic components by up to 87 types of Galactic source, each fully characterized by scale heights, space densities, and absolute magnitudes at *BVJHK*, 12, and 25  $\mu\text{m}$ . Our model has been guided by a parallel Monte Carlo simulation of the Galaxy at 12  $\mu\text{m}$ . The content of our Galactic source table constitutes an excellent match to the 12  $\mu\text{m}$  luminosity function in the simulation, as well as to the luminosity functions at *V* and *K*. We are able to produce differential and cumulative infrared source counts for any bandpass lying fully within the *IRAS* Low-Resolution Spectrometer’s range (7.7–22.7  $\mu\text{m}$ ) as well as for the *IRAS* 12 and 25  $\mu\text{m}$  bands. These source counts match the *IRAS* observations extremely well. The model can be used to predict the character of the point source sky expected for observations from future infrared space experiments (e.g., ISO, SIRTf, LDR, 2MASS).

*Subject headings:* Galaxy: structure — infrared: general

<sup>1</sup> Institute for Astronomy, 2680 Woodlawn Drive, Honolulu, HI 96822.

<sup>2</sup> Radio Astronomy Laboratory, University of California, Berkeley, CA 94720.

<sup>3</sup> Department of Physics and Astronomy, University of Calgary, 2500 University Drive N.W., Calgary, Alberta, Canada T2N1N4.

<sup>4</sup> Rutherford Appleton Laboratory, R68, Chilton, Didcot, Oxon OX11 0QX, England, UK.

<sup>5</sup> NASA Ames Research Center, Mail Stop 239-12, Moffett Field, CA 94035.

## 1. INTRODUCTION

In 1983, the *IRAS* satellite surveyed the sky at wavelengths of 12, 25, 60, and 100  $\mu\text{m}$ . At 12 and 25  $\mu\text{m}$ , many of the point sources seen by *IRAS* are red giant stars with mass loss (Hacking et al. 1985); these stars are very luminous in the mid-infrared and can therefore be seen at great distances. The extinction at these wavelengths is relatively small, so these stars are seen even at low Galactic latitudes. The *IRAS* Point Source Catalog (1988, hereafter PSC) therefore offers a valuable tool for studying the structure of our Galaxy.

The comparison of star counts with models for Galactic structure has a long history. Bahcall (1986) provides a recent review of modern star count models based primarily on visible wavelengths. These counts are restricted to higher Galactic latitudes where the extinction is small. Eaton, Adams, & Giles (1984), Kawara et al. (1982), and Ruelas-Mayorga (1986) have obtained 2.2  $\mu\text{m}$  star counts at low latitudes and compared them with simple models for Galactic structure. Japanese astronomers have published an extensive series of near-IR balloon-borne observations of the Galactic plane (summarized by Okuda 1981). While these measurements are primarily of the diffuse emission from the plane at 2.4  $\mu\text{m}$ , Kawara et al. (1982) have shown that 2.2  $\mu\text{m}$  star counts mimic (if not explain completely) this diffuse emission. Models for the Galaxy were presented by Maihara et al. (1978) who examined the bulge in some detail, by Kawara et al. (1982) who modeled the exponential disk, and Mikami et al. (1982) who used an exponential disk, a (molecular) ring with 5 kpc radius, and a bulge. Habing (1986, 1988) and Garwood & Jones (1987) have modeled subsets of the *IRAS* star counts. The first attempt to model the entire *IRAS* sky (Volk et al. 1992; see also Cohen et al. 1990) used a Monte Carlo approach to simulate the geometrical and luminosity distributions of 12  $\mu\text{m}$  *IRAS* sources. In this paper, we describe a more versatile model which can predict source counts not only in the *IRAS* 12  $\mu\text{m}$  passband, but also in the *IRAS* 25  $\mu\text{m}$  passband and in any passband lying within the *IRAS* Low-Resolution Spectrometer (LRS) range of wavelengths (7.7–22.7  $\mu\text{m}$ ). The predictions available from this model will clearly be of great value to the design and operation of future infrared space observatories (e.g., ISO, SIRTf, LDR, 2MASS). In addition to predicting differential and cumulative source counts at 12 or 25  $\mu\text{m}$ , our model also operates at *JHK* and *BV* (visible light) wavelengths, permitting self-consistency checks.

The model was developed to extrapolate *IRAS* 12 and 25  $\mu\text{m}$  observed source counts to much fainter levels and to interpolate counts to spectral bands within the LRS range. We judiciously selected luminosity and spatial distribution parameters of the model to provide best fits (perhaps subjective) to *IRAS* source counts. Because our selections were based on limited examination of visible and near-infrared source counts too, the model can predict source counts in reasonable agreement with these other investigations (see §§ 4.5 and 4.6). In this paper we pursue the model development and explore limits to its utility.

In order to allow our model to predict source counts through any bandpass lying in the LRS wavelength range, we have made use of the *IRAS* LRS spectra. This necessitated the representation of Galactic sources through a large source table (with each class of source having its own representative LRS spec-

trum), rather than using the classical luminosity function approach (e.g., Bahcall & Soneira 1984). Our method is, therefore, similar to that used by Jones et al. (1981).

A prerequisite for any model which represents the sky by a specific set of categories of Galactic source is a complete data base in which are assembled: the absolute magnitudes in a “reference” passband; broad-band colors for other “standard” passbands relative to the reference; full spectral representations across any wavelength domain where a “nonstandard” passband will be used; space densities; and geometrical information such as scale height, radial scale length, and whether the sources are found in the disk, stellar halo, bulge, arms, and/or ring. In § 2.2 we treat the construction of such a data base for our model.

Extragalactic sources have extreme colors compared with stars. For example, the nearby galaxy NGC 253 has  $V - [25] \approx 10$  (cf., an A0 star has  $V - [25] = 0$ ). Therefore, especially at the longer of the two *IRAS* wavelengths that we model, 25  $\mu\text{m}$ , and at the higher Galactic latitudes, galaxies make an important contribution to the source counts. We have, therefore, included the prediction of galaxy counts in our model for these mid-infrared wavelengths. As we will see later, at relatively modest flux levels, not far below the *IRAS* threshold, galaxies actually become the dominant source at high latitudes at 25  $\mu\text{m}$ . In the Galactic plane, Galactic sources dominate at all wavelengths and at all practical flux levels.

It is clearly important to represent the Galaxy with as much physical realism as possible. The new sources discovered by *IRAS* show strong color dependence on Galactic latitude (Walker et al. 1989). These effects speak for the importance of an accurate representation of the disk, spiral arms, and bulge, in which reside almost all of the extremely red Galactic objects.

In a series of papers we have explored the broad-band *IRAS* colors of normal (Cohen et al. 1987) and AGB stars (Walker & Cohen 1988), and of nonstellar *IRAS* sources (Walker et al. 1989). Histograms of *IRAS* color indices, e.g.,  $[12] - [25]$ , show that there is a strong concentration of most very red *IRAS* sources to the Galactic plane (Walker et al. 1989). This is suggestive of contributions from both the intermediate-mass AGB population and from the traditional high-mass optical tracers of spiral structure (H II regions and reflection nebulae), all of which are very red to *IRAS*. These red objects become increasingly important to models of the infrared sky as the wavelength increases. Such studies of the *IRAS* color-color planes are crucial since they often reveal that optically defined populations may have more than one infrared representation. For example, carbon stars are found in two color-color domains depending on their visual detectability (Cohen et al. 1989b); likewise, planetary and reflection nebulae, and “normal” galaxies occur in distinct “red” and “blue” varieties as mapped in the 12–25–60  $\mu\text{m}$  color-color planes (Walker et al. 1989).

Once these various populations are considered, there seems no reason to conclude that *IRAS* detected any other abundant population, at least as indicated by the sample of sources newly discovered by *IRAS* that were bright enough to be well detected at 12, 25, and 60  $\mu\text{m}$  (Walker et al. 1989). This conclusion is in part supported by ground-based optical spectroscopy of some 450 *IRAS* objects having optical counterparts but not associated in pre-existing catalogs (e.g., Cohen et al. 1989b).

One might worry about the possible contributions from

small extended sources to our representation of the point source infrared sky. However, Walker et al. (1989) have found only small color differences for individual galaxies and nebulae between the PSC and *IRAS* Small-Scale Structure Catalog (1988) measurements, all of which are understandable in terms of either the different beam sizes inherent in the *IRAS* survey at 25 and 60  $\mu\text{m}$ , or spatially extended emission by PAH molecules. These slight differences do not justify the definition of different colors for members of these nonstellar populations unresolved and spatially resolved by *IRAS* since the emphasis of our model is on point sources. Therefore, we adopt the infrared colors ( $[12] - [25]$ ,  $[25] - [60]$ ) of the basic populations as defined by Walker et al. (1989) for our purposes.

For  $V - [12]$  colors we follow Cohen et al. (1987) for stars with standard spectral types and luminosity classes. For more exotic objects we describe below our methods for relating  $V$  to  $[12]$ . To relate the near-infrared wavelengths to one another we have relied upon the literature to provide basic photometry (and sometimes colors) for broad classes of object, as described in § 2.2.

The detailed spectral characterization of our model in the mid-infrared has required extensive use of data from the Low-Resolution Spectrometer (LRS). These spectra have been available to us from two sources: the *IRAS* Atlas of Low Resolution Spectra (1986; hereafter the Atlas), which is a collection of average spectra for 5425 sources and is the official *IRAS* product; and the complete LRS extracted data base, which is the much larger ( $\sim 170,000$  spectra) data base from which the Atlas was drawn.

Throughout this paper, all fluxes have been color corrected by assuming that the source is a 10,000 K blackbody. The zero points for the magnitudes are defined by equation (VI.C.1) in the *IRAS* Explanatory Supplement (1988); the color corrections are in Table VI.C.6. We define:

$$[12] = 4.034 - 2.5 \log_{10} F_\nu(12 \mu\text{m}), \quad (1)$$

$$[25] = 2.444 - 2.5 \log_{10} F_\nu(25 \mu\text{m}), \quad (2)$$

$$[60] = 0.490 - 2.5 \log_{10} F_\nu(60 \mu\text{m}), \quad (3)$$

where  $F_\nu$  is from the PSC, and  $[P]$  is the magnitude in pass-band  $P$ . In this representation,  $\alpha$  Lyr has  $[12] = -0.01$  which is consistent with the general definitions of magnitudes found in the literature. (Note that for  $\alpha$  Lyr,  $[25] = -0.16$ , and  $[60] = -1.96$ —these anomalous values at longer wavelengths are due to cool dust around this star.) This representation of *IRAS* magnitudes is identical to that used by Cohen et al. (1987). We define corresponding absolute magnitudes  $M_{12}$ ,  $M_{25}$ , and  $M_{60}$ , which are simply the above definitions of  $[12]$ ,  $[25]$ , and  $[60]$  for the source located at a distance of 10 pc.

## 2. THE GALAXY

### 2.1. Galactic Structure

Our treatment of Galactic structure closely follows that of Volk et al. (1992), who simulated the observed *IRAS* 12  $\mu\text{m}$  structure of the Galaxy using Monte Carlo techniques. Below, we describe in detail the five geometrical components which we found were necessary to model properly the source counts

in the Galaxy. Our model differs from the traditional optical star count models (e.g., Bahcall & Soneira 1980) through the necessary inclusion of the Galactic bulge and sources in the spiral arms and molecular ring. Optical star counts are only useful for  $|b| \gtrsim 20^\circ$  due to extinction; our model must also work at low Galactic latitudes.

Both the halo and thick disk are relatively insignificant in the infrared. We chose to include the halo because of the desire to retain in our model the ingredients and therefore the capability of the Bahcall-Soneira code to predict the visible sky. The thick disk remains controversial. Bahcall et al. (1985) absorb it into their spheroid, but Gilmore & Reid (1983) argue that a distinct component exists. More recently, Fenkart (1989a–d), in a series of four papers, finds “comfortable confirmation” for the thick disk in analyses of Basle star counts. Kinematics and spectroscopy favor its existence (Carney, Latham, & Laird 1989), but it may contribute only 2% to counts in the local neighborhood. Counts alone cannot determine whether the thick disk is kinematically or chemically distinct from the thin (Gilmore, Wyse, & Kuijken 1989). We omitted the thick disk from our model because of the controversy surrounding its existence and because of the difficulty of choosing a widely acceptable parametric representation of it.

We have chosen to represent Galactic sources by a series of classes rather than by a luminosity function. This has the advantage of allowing much greater versatility in selecting pass-bands, but is computationally more cumbersome. The aggregate of all the classes that we represent in this way, expressed in terms of  $(\text{mag}, \log \phi)$ , is simply the luminosity function.

Throughout this paper, we will use a cylindrical coordinate system  $(R, \theta, z)$ , where  $R$  is distance from the Galactic center within the plane,  $\theta$  is the angular coordinate in the plane, with origin at  $l = 0$  and handedness such that  $\sin l \leq 0$  implies  $0 \leq \theta \leq \pi$ , and  $z$  is distance from the plane. We use  $R_0$  to represent Galactocentric distance and have assumed  $R_0 = 8.5$  kpc.

#### 2.1.1. The Exponential Disk

Our treatment of the exponential disk closely follows that of Bahcall & Soneira (1980). We assume that

$$\rho(R, z, S) = \begin{cases} \rho_D(S) \exp [-(R - R_0)/h - |z|/h_z(S)] & R \leq R_{\max} \\ 0 & R > R_{\max} \end{cases}, \quad (4)$$

where  $S$  has been used to denote spectral class,  $h$  is the radial scale length,  $\rho_D(S)$  is the number density in the solar neighborhood of stars of class  $S$ ,  $h_z(S)$  is their scale height, and  $R_{\max}$  is a truncation in the disk.

The radial exponential decline in the disks of spiral galaxies is well established in the literature (see e.g., de Vaucouleurs 1959; Freeman 1970; Kormendy 1977). Bahcall & Soneira (1980) discuss in detail a number of determinations of  $h$ , and adopted  $h = 3.5$  kpc. More recent determinations of  $h$  ( $4.4 \pm 0.3$  kpc, Lewis & Freeman 1989;  $5.5 \pm 1.0$  kpc, van der Kruit 1986) have yielded larger values (see Kent, Dame, & Fazio (1991) for a useful summary of some of these values). However, it is noteworthy that the determinations based on near-infrared data all suggest smaller values, from the extremely small 1 kpc determined from the



Two Micron Sky Survey by Mikami & Ishida (1981), through the more typical 2.3 kpc length of Maihara et al. (1978) and of Mikami et al. (1982), up to the 3.0 kpc of Eaton et al. (1984). Our model is not very sensitive to the choice of  $h$ ; we have adopted  $h = 3.5$  kpc for consistency with the Bahcall & Soneira model. The truncation seen in the disks of external galaxies is discussed in detail by van der Kruit & Searle (1982), who find that the truncation distance has a mean and scatter of  $R_{\text{max}}/h = 4.2 \pm 0.6$ . We will assume that such a truncation exists in our Galaxy also, at a distance of  $R_{\text{max}} = 15.0$  kpc. A possible explanation for the truncation is furnished by Seiden, Schulman, & Elmegreen (1984), within the framework of stochastic star formation.

Van der Kruit & Searle (1981a, b, 1982) have proposed a locally isothermal disk model with vertical distribution  $L(z) \propto \text{sech}^2(z/z_0)$ . We have chosen instead to use  $L(z) \propto \exp[-|z|/h_z(S)]$ . The choice of the exponential instead of the isothermal distribution is motivated by recent observations of edge-on galaxies in the near-infrared (Wainscoat, Freeman, & Hyland 1989; Wainscoat 1992). At  $K$  ( $2.2 \mu\text{m}$ ), the vertical light distribution in these galaxies is seen to persist as an exponential to very small values of  $z$ .

It is well known that the older stars in the disk have larger scale heights than the younger stars (collisions with clouds are expected to cause an increase in velocity dispersion over time). We have, therefore, assigned a scale height to each class of star in our source table (see Table 2, discussed in more detail below in § 2.2). We have adopted scale heights ranging from  $h_z = 90$  pc for the youngest stars to  $h_z = 325$  pc for the oldest.

Habing (1988) modeled the disk of the Galaxy using *IRAS* source counts. His best-fitting model contained a substantial thick disk component. We did not find it necessary to include such a component to produce a satisfactory fit to the *IRAS* source counts.

The exponential disk is the most important point source component of the Galaxy at the shorter *IRAS* wavelengths (12 and  $25 \mu\text{m}$ ) and at *IRAS* flux levels ( $F_\nu > 0.1$  Jy) everywhere in the Galaxy, except for small  $|b|$ , where the arms and ring components contribute, and near the Galactic center, where the bulge is important.

### 2.1.2. The Bulge

We adopt the structural bulge representation derived by Volk et al. (1992) and proposed by Bahcall (1986; see also Sanders & Lowinger 1972, who first introduced the  $x^{-1.8}$  term). This can be summarized by

$$\rho(x, S) = \rho_B(S)x^{-1.8}e^{-x^3}, \quad (5)$$

where

$$x = \sqrt{R^2 + k_1^2 z^2}/R_1 \quad (6)$$

is a dimensionless number,  $\rho_B(S)$  is the number density of bulge stars of class  $S$  at  $x^{-1.8}e^{-x^3} = 1$  (i.e.,  $x = 0.77338$ ),  $k_1$  is the bulge axis ratio (note that we define  $k_1 = a/b$ , so  $k_1 \geq 1.0$ ), and  $R_1$  is the bulge “radius”—note that the exponential term in equation (5) produces a rapid decline in bulge star density

outside  $R_1$ . We use the values of  $k_1 = 1.6$  and  $R_1 = 2.0$  kpc found by Volk et al., although we had neither the time nor the resources to perform a complete sensitivity analysis of our bulge with respect to axial ratio and radius.

We note that Maihara et al. (1978) used a slightly different analytic formulation to model their bulge/halo and compare with near-infrared diffuse emission. We chose the Bahcall formulation which treats the bulge and halo as separate components in order to retain consistency with the Bahcall & Soneira (1980) model at high latitudes. The actual bulge structure is likely to be more complex than either the Bahcall or Maihara et al. formulations, in light of the intriguing work by Catchpole, Whitelock, & Glass (1990), who found that axial ratio may vary with distance from the center.

We have assumed that the bulge has a similar stellar composition to the disk, except that we have not allowed young massive stars to be present in the bulge. The bulge has low-mass high-metallicity giants which attain high  $[12] - [25]$  colors yet have more modest luminosities than their higher mass disk counterparts. We do not explicitly include these stars in our model.

### 2.1.3. The Stellar Halo

We have assumed that the stellar halo conforms to the  $R^{1/4}$  law (de Vaucouleurs 1959). This is a projected distribution, observed in the spheroidal components of spiral galaxies as well as in elliptical galaxies. It has the form

$$\log_{10} \frac{I(\alpha)}{I(1)} = -3.3307(\alpha^{1/4} - 1), \quad (7)$$

where  $I$  is the observed surface brightness,  $\alpha$  is the dimensionless angular distance defined by

$$\alpha = \sqrt{R^2 + k_e^2 z^2}/R_e, \quad (8)$$

$k_e$  is the halo axis ratio, and  $R_e$  is the “effective radius” of the stellar halo—the constant in equation (7) has been chosen so that half of the total luminosity is enclosed within  $\alpha = 1$ .

Studies of the globular cluster system in our Galaxy (de Vaucouleurs 1977; de Vaucouleurs & Buta 1978) have shown that their distribution closely follows the de Vaucouleurs  $R^{1/4}$  law and that they have an effective radius of  $R_e \approx R_0/3.0$ . We therefore adopt  $R_e = 2.83$  kpc. We use  $k_e = 1.25$  and normalize the halo star density to be  $\rho_S = 0.002\rho_D$  in the solar neighborhood; these values are the same as used by Bahcall & Soneira (1984). We do not allow young massive stars to be present in the halo; due to the halo’s relatively low metallicity, we also decrease the numbers of the redder giant stars.

As will be shown later, the stellar halo is not an important component of the Galaxy anywhere at *IRAS* fluxes and wavelengths. In the  $\log N - \log F$  plane, the halo stars have a steeper slope than the disk stars—this is because their distribution falls off less rapidly than the disk stars. It is only at fainter magnitudes (e.g., in deep optical star counts) that the halo becomes important.

### 2.1.4. The Spiral Arms

Volk et al. (1992) showed that a much better fit to the distribution of low-latitude Galactic point sources was possible

when sources in the spiral arms were included. We have therefore included spiral arm sources in our model. Elmegreen (1985) has summarized the data that favor both two- and/or four-armed spiral patterns in the Galaxy. Her Figure 4, in particular, suggests that a 4-armed pattern provides a better fit to the inner Galaxy whereas a two-armed pattern yields a superior fit to the distribution of canonical spiral arm tracers. We followed the four-armed pattern of Georgelin & Georgelin (1976) on the grounds that it is more challenging to represent the complex inner Galaxy well, than the outer, and perhaps more important for an infrared model. Our spiral arm representation is derived from the data of Georgelin & Georgelin—we use a four arm logarithmic spiral

$$\theta(R) = \alpha \log(R/R_{\min}) + \theta_{\min}, \quad (9)$$

where  $\alpha$  is a winding constant,  $R_{\min}$  is the inner radius and  $\theta_{\min}$  is the angle at that inner radius. The arms are set to be 6 radians long, but are truncated at  $R = R_{\max}$  if they attain that radius. We have used the same exponential radial and vertical distributions for the arms as for the exponential disk component, except that the arms are 750 pc wide (in  $R$ ), centered on the radial locations described by equation (9). We define corresponding arm number density normalization constants  $\rho_A(S)$  which are analogous to the constants  $\rho_D(S)$  in equation (4). Table 1 describes the parameters for the two pairs of arms; in this table,  $\theta_{\min}$  is in radians. Each arm pair consists of an arm and a duplicate,  $\pi$  radians away in  $\theta$ .

The arms are assumed to consist primarily of massive young stars. They therefore represent an enhancement of this type of star over the population present in the smooth exponential disk. We do not include a corresponding enhancement in the lower mass older stars in the arms; these stars are assumed to be old enough that they have diffused away from the spiral arms (if they were formed there) and form part of the smooth exponential disk.

In addition to the four arms described above, we found it necessary to include the types of source found in the spiral arms in the “local arm” too. There is evidence for this feature from H I (Weaver 1989) and CO observations (e.g., Cohen et al. 1980), as well as in observations of high-mass stars (Becker & Fenkart 1970; Blaauw 1985; Weaver 1989). This feature was required to improve the match in number of stars and slope in the  $\log N$ - $\log F$  relation in the region  $50^\circ \lesssim l \lesssim 150^\circ$  for low Galactic latitude. We regarded the local arm as having the same stellar composition and geometrical form as the four main arms (defined by eq. [9]), with parameters shown in Table 1. These parameters reproduce the inherent curvature of the local feature and its abrupt disappearance toward  $l \approx 250^\circ$

(Becker & Fenkart 1970). For the purposes of this paper, we regard this “local arm” as part of the spiral arm structure.

The inclusion of the local spur may seem to be a deviation from our intent to produce a global Galactic model. However, the spur is readily amenable to an analytic representation and its influence is not spatially so restricted. To preserve our analytic approach and maintain computational speed we chose not to incorporate structures that are less readily represented geometrically, such as the Magellanic Clouds and local molecular complexes (for example, those within Gould’s Belt).

The sources in the spiral arms are an important component of the model at low latitudes, but are unimportant at higher latitudes.

### 2.1.5. The Molecular Ring

CO observations of our Galaxy (e.g., Clemens, Sanders, & Scoville 1988) have shown that a “molecular ring” is present at  $R \sim 0.45R_0$ . Volk et al. (1992) found an increase in *IRAS* star counts corresponding to this position and concluded that it was necessary to include sources located in this ring. Volk et al. included mainly high-mass infrared-bright sources in their simulations; because of the large distance from us, *IRAS* could only see very bright sources in the ring. We initially adopted the same strategy, assigning to the ring the same stellar mix as we had assigned the arms. However, comparisons with the *K* star counts of Eaton et al. (1984), which are able to see much less luminous stars at the distance of the ring, suggested that the ring should also contain some of the lower mass, less luminous sources. In this sense, the “molecular ring” could therefore be regarded as a true stellar ring; there are many examples of rings in external galaxies (e.g., Buta 1986, 1987).

The ring was assumed to have a Gaussian distribution of the form

$$\rho(R, S) = \rho_r(S) \exp \left[ \frac{-(R - R_r)^2}{2\sigma_r^2} \right], \quad (10)$$

where the “ring radius”  $R_r = 0.45R_0$ , and  $\sigma_r = 0.064R_0$  corresponds to a half-width for the Gaussian ring of  $0.15R_0$ , and  $\rho_r(S)$  is the density of ring stars of class  $S$  at  $R = R_r$ . The vertical  $z$  distribution of the ring stars was assumed to be the same as that of their disk counterparts.

### 2.2. Source Tables

We now describe in detail our source tables from which the five components of the Galaxy are composed. The basic approach that we have adopted is similar to that of Elias (1978a), Jones et al. (1981), and Garwood & Jones (1987), who chose to represent the luminosity function by breaking it down into stellar classes. Each class of star (or nonstellar source) is represented by an absolute magnitude in a selection of passbands of interest, a dispersion in the absolute magnitude, a number density in the solar neighborhood in the disk, a disk scale height, and a set of numbers showing the relative occurrence of that type of source in each of the five Galactic components. Each class of source is assumed to have a Gaussian distribution

TABLE 1  
SPIRAL ARM PARAMETERS

Arm	$\alpha$	$R_{\min}$	$\theta_{\min}$	Extent
1 .....	4.25	3.48	0.000	6.0
1' .....	4.25	3.48	3.141	6.0
2 .....	4.89	4.90	2.525	6.0
2' .....	4.89	4.90	5.666	6.0
L .....	4.57	8.10	5.847	0.55

with dispersion  $\sigma$ , of the form

$$N(M) \propto \exp \left[ \frac{-(M - M_\lambda)^2}{2\sigma^2} \right], \quad (11)$$

where  $M_\lambda$  is taken from Table 2.

Below, we describe how we calculated the absolute magnitudes, number densities, dispersions, and scale heights in our table. We do not consider that this table should be used as a definitive reference for absolute magnitudes and number densities of Galactic sources; rather it is our best effort at estimating these quantities from the literature. Some of the quantities may have large errors.

### 2.2.1. Stars

Table 2 lists the 87 types of Galactic source that we considered. The first section of the table is very similar to that of Jones et al. (1981). This section of the source table contains all “normal” stars; it consists of 33 classes of star. We have split the F8-G2 V class defined by Jones et al. into two separate classes (F8 V and G0-2 V)—this was done to make the  $V$  luminosity function synthesized from the source table match the observed  $V$  luminosity function more closely. We added the “M late V” class to represent very low mass red dwarfs, and removed the M8+ III class. This class contains evolved stars with mass loss—these stars are very important for *IRAS*, and we devote the second section of Table 2 to characterizing them.

The basic content of the first section of Table 2 originates from Elias (1978a), Jones et al. (1981), Ruelas-Mayorga (1986), and Garwood & Jones (1987), although many of the detailed values are modified. Some of the number density modifications were made to attain better consistency with the observed  $V$  luminosity function and the faint part of the  $12\ \mu\text{m}$  luminosity function derived by Volk et al. (1992). We used  $V - K$ ,  $J - H$ , and  $H - K$  colors from Koorneef (1983) rather than the values of Johnson (1966) used by Elias. Absolute magnitudes at  $V$  came from a variety of sources including Blaauw (1963), Keenan (1963), and other sources listed by Elias. We used the  $V - [12]$  and  $V - [25]$  colors derived by Cohen et al. (1987), except for the K III and K V stars whose  $V - IRAS$  colors appeared to be too blue relative to their  $V - K$  colors, and slightly redder values were used. We have used scale heights which are slightly larger than the values used by Jones et al. Our values are similar to those used by Bahcall & Soneira (1980).

The second section of Table 2 consists of the evolved AGB stars. These stars have mass loss, so are in varying degrees surrounded by dust. They therefore emit a large fraction of their luminosity in the mid-infrared, and warrant careful characterization in a model of the Galaxy at the shorter *IRAS* wavelengths. This section of the table contains O-rich and C-rich stars. The C-rich stars are further subdivided into “optically visible” and “optically invisible” C stars. The  $M_{12}$  and  $M_{25}$  values, the relative  $\log \rho_0$  values, and the dispersions in the table result from a detailed AGB stellar evolution model (see Appendix) for stars in the mass range  $1.25\text{--}8\ M_\odot$  (only stars in the range  $1.25\text{--}4\ M_\odot$  could become carbon stars). Each class in the table represents a range of  $[12] - [25]$  color—e.g., the class

“AGB M 07” represents O-rich stars having  $0.6 < [12] - [25] < 0.8$  and is shown in the table as having  $[12] - [25] = 0.7$ .

For the M stars, we used stars listed in the General Catalog of Variable Stars (Kukarkin et al. 1970, hereafter GCVS) having LRS class 2 or 3, and very red M stars selected from the AFGL Sky Survey (Price & Walker 1976) and studied by Cohen & Kuhl (1976, 1977), to define  $K - [12]$ ,  $V - K$ , and  $B - V$  for each range of  $[12] - [25]$ . The  $B$  magnitudes were taken from the Bright Star Catalog (Hoffleit & Jaschek 1982, hereafter BSC) and from the Smithsonian Astrophysical Observatory Star Catalog (1966, hereafter SAOC); the  $V$  magnitudes were taken from the BSC, the SAOC, or the Two Micron Sky Survey (Neugebauer & Leighton 1969, hereafter TMSS); and the  $K$  magnitudes were taken from the TMSS or from Gezari, Schmitz, & Mead (1987). For the  $[12] - [25]$  color ranges for which no observations existed, plausible estimates were made based on trends in the observed colors. The  $J - H$  and  $H - K$  colors were estimated from the  $V - K$  colors.

The near-infrared carbon star colors were calculated from the tabulations of Claussen et al. (1987). We assigned carbon stars having  $K - [12] \geq 2.4$  to the “infrared” carbon star classes, and others to the “optical” carbon star classes. We obtained  $B$  and  $V$  colors from Stephenson’s (1973) catalog, and corrected them for interstellar extinction using the  $A_K$  values from Claussen et al. For the carbon star classes having large values of  $[12] - [25]$ , shorter wavelength observations are not available; we therefore estimated colors for these stars based upon the colors at smaller  $[12] - [25]$  values.

The relative space densities for the AGB stars were taken from our stellar evolution model, as were the absolute magnitudes and dispersions. The final space densities were subsequently obtained by normalizing the synthesized total  $12\ \mu\text{m}$  luminosity function in the magnitude range  $-14 \leq M_{12} \leq -11$  to the luminosity function derived by Volk et al. (1992).

The third section of Table 2 contains “ultraluminous”  $12\ \mu\text{m}$  sources. It was clear from our parallel Monte Carlo simulations of the Galaxy at  $12\ \mu\text{m}$  that very bright  $12\ \mu\text{m}$  sources are indeed present in the Galaxy and that the luminosity function must extend beyond the luminosities defined by our AGB stars, to at least  $M_{12} = -17$ .

In order to represent these correctly we endeavored to identify individual stars that lay in this very luminous range. One obvious potential source of such objects is the set of OH/IR stars detected by *IRAS* for which OH phase lag or kinematic distances are available so we could determine  $M_{12}$ . We found 46 of these to be in the ultraluminous category. We then searched the literature in an effort to identify other types of star having  $M_{12} < -13$ . An appreciable number of probably very bright stars were identified but estimates of their distance were judged far less secure than the kinematic distances often available through OH radio measurements (or from the known location of an object in one of the Magellanic Clouds). Objects with well-determined distances were as follows, in order of increasing absolute  $12\ \mu\text{m}$  brightness: Hubble-Sandage variables in the LMC (S Dor and R71); the luminous M supergiant, S Per; M hypergiants such as VX Sgr and VY CMa; the B1 hypergiant MWC 300 (Wolf & Stahl 1985); the peculiar object,  $\eta$  Car. All lie in the range  $-18.1 \leq M_{12} \leq -13.5$ .

Based upon the above findings, we populated this region by



TABLE 2  
SOURCE TABLE

Type	$M_B$	$M_V$	$M_J$	$M_H$	$M_K$	$M_{12}$	$M_{25}$	$\sigma$	$h_z$ pc	$\log \rho_0$ kpc <sup>-3</sup>	disk	arms	ring	bulge	halo
B0,1 V	-4.08	-3.80	-3.15	-3.04	-3.00	-2.80	-3.30	0.70	90	2.95	0.2	0.4	0.4	0.0	0.0
B2,3 V	-2.22	-2.00	-1.50	-1.41	-1.38	-1.26	-1.76	0.50	90	3.85	0.2	0.4	0.4	0.0	0.0
B5 V	-1.16	-1.00	-0.65	-0.59	-0.57	-0.50	-1.00	0.50	90	4.10	0.2	0.4	0.4	0.0	0.0
B8-A0 V	0.15	0.20	0.31	0.32	0.33	0.27	0.27	0.50	110	5.35	0.4	0.3	0.3	0.0	0.0
A2-5 V	1.70	1.60	1.42	1.38	1.36	1.33	1.33	0.50	130	5.55	0.6	0.2	0.2	0.0	0.0
F0-5 V	3.32	2.95	2.27	2.09	2.04	2.00	2.00	0.50	160	6.10	0.8	0.1	0.1	0.0	0.0
F8 V	4.54	4.00	3.17	2.94	2.88	2.80	2.78	0.50	270	6.20	1.0	0.0	0.1	1.0	1.0
G0-2 V	5.16	4.55	3.57	3.31	3.24	3.14	3.11	0.50	270	6.30	1.0	0.0	0.1	1.0	1.0
G5 V	5.81	5.15	4.00	3.70	3.61	3.46	3.43	0.50	325	6.50	1.0	0.0	0.1	1.0	1.0
G8-K3 V	6.93	6.10	4.62	4.19	4.08	3.88	3.83	0.50	325	6.80	1.0	0.0	0.1	1.0	1.0
K4-5 V	8.65	7.50	5.37	4.79	4.63	4.35	4.28	0.60	325	6.90	1.0	0.0	0.1	1.0	1.0
M0-1 V	10.45	9.00	6.47	5.82	5.63	5.26	5.16	0.70	325	7.00	1.0	0.0	0.1	1.0	1.0
M2-3 V	11.94	10.40	7.43	6.77	6.53	6.12	6.01	0.80	325	7.10	1.0	0.0	0.1	1.0	1.0
M4-5 V	13.39	11.80	8.33	7.71	7.43	6.98	6.85	1.00	325	7.20	1.0	0.0	0.1	1.0	1.0
M late V	14.91	13.20	9.25	8.67	8.33	7.83	7.65	1.00	325	7.30	1.0	0.0	0.1	1.0	1.0
F8-G2 III	3.10	2.45	1.00	0.56	0.45	0.43	0.41	1.00	325	4.50	1.0	0.0	0.1	1.0	1.0
G5 III	2.89	2.05	0.50	0.05	-0.07	-0.10	-0.13	1.00	325	4.50	1.0	0.0	0.1	1.0	1.0
G8 III	2.55	1.60	0.03	-0.44	-0.56	-0.59	-0.63	0.80	270	5.05	1.0	0.0	0.1	1.0	1.0
K0,1 III	2.37	1.30	-0.45	-0.97	-1.11	-1.18	-1.23	0.70	270	5.40	1.0	0.0	0.1	1.0	1.0
K2,3 III	2.34	1.10	-0.89	-1.50	-1.65	-1.76	-1.82	0.70	270	5.05	1.0	0.0	0.1	1.0	1.0
K4,5 III	1.80	0.35	-2.18	-2.91	-3.10	-3.26	-3.33	0.70	325	4.25	1.0	0.0	0.1	1.0	1.0
M0 III	1.17	-0.40	-3.17	-3.93	-4.14	-4.35	-4.44	0.60	325	3.60	1.0	0.0	0.1	1.0	1.0
M1 III	1.12	-0.50	-3.39	-4.19	-4.40	-4.69	-4.79	0.60	325	3.30	1.0	0.0	0.1	1.0	1.0
M2 III	1.06	-0.60	-3.72	-4.53	-4.76	-5.03	-5.14	0.60	325	3.20	1.0	0.0	0.1	1.0	1.0
M3 III	1.11	-0.60	-4.13	-4.98	-5.23	-5.51	-5.61	0.60	325	3.15	1.0	0.0	0.1	1.0	1.0
M4 III	1.05	-0.70	-4.88	-5.77	-6.04	-6.18	-6.31	0.60	325	3.10	1.0	0.0	0.1	1.0	0.8
M5 III	1.10	-0.70	-5.66	-6.59	-6.90	-6.79	-7.00	0.50	325	3.00	1.0	0.0	0.1	1.0	0.6
M6 III	1.15	-0.70	-6.60	-7.55	-7.90	-8.37	-8.68	0.50	325	2.50	1.0	0.0	0.1	1.0	0.4
M7 III	1.20	-0.70	-7.67	-8.65	-9.04	-9.93	-10.45	0.50	325	2.25	1.0	0.0	0.1	1.0	0.2
YOUNG OB	-5.30	-5.14	-4.78	-4.73	-4.70	-4.64	-4.64	1.20	90	2.30	0.2	0.4	0.4	0.0	0.0
A-G I-II	-5.62	-6.05	-6.73	-6.95	-7.00	-7.30	-7.30	2.00	90	1.50	0.2	0.4	0.4	0.0	0.0
K-M2 I-II	-4.69	-6.34	-8.67	-9.32	-9.50	-10.22	-10.32	1.00	90	1.50	0.2	0.4	0.4	0.0	0.0
M3-4 I-II	-3.89	-5.79	-9.82	-10.72	-11.00	-11.50	-11.70	1.00	90	1.10	0.2	0.4	0.4	0.0	0.0
AGB M 01	2.70	1.19	-3.27	-4.05	-4.38	-4.64	-4.74	0.25	270	-0.79	1.0	0.0	0.1	1.0	1.0
AGB M 03	2.77	1.21	-3.64	-4.49	-4.85	-5.51	-5.81	0.78	270	0.44	1.0	0.0	0.1	1.0	1.0
AGB M 05	2.62	1.01	-4.11	-5.01	-5.39	-6.60	-7.10	1.21	270	1.21	1.0	0.0	0.1	1.0	1.0
AGB M 07	1.70	0.04	-5.48	-6.45	-6.86	-8.36	-9.06	1.14	270	1.42	1.0	0.0	0.1	1.0	1.0
AGB M 09	1.20	-0.52	-6.36	-7.38	-7.82	-9.69	-10.59	0.92	250	1.55	0.8	0.1	0.1	1.0	1.0
AGB M 11	1.15	-0.73	-7.05	-8.16	-8.63	-10.90	-12.00	0.80	220	1.53	0.6	0.2	0.2	1.0	0.0
AGB M 13	1.70	-0.30	-7.50	-8.76	-9.30	-12.32	-13.62	0.90	220	1.12	0.4	0.3	0.3	1.0	0.0
AGB M 15	2.39	0.29	-7.31	-8.64	-9.21	-13.32	-14.82	0.74	160	0.45	0.2	0.4	0.4	0.0	0.0
AGB M 17	3.55	1.35	-6.65	-8.05	-8.65	-13.81	-15.51	0.62	160	-0.12	0.2	0.4	0.4	0.0	0.0
AGB M 19	4.87	2.57	-5.83	-7.30	-7.93	-14.03	-15.93	0.56	110	-0.47	0.2	0.4	0.4	0.0	0.0
AGB M 21	5.72	3.32	-5.48	-7.02	-7.68	-14.18	-16.28	0.45	110	-0.89	0.2	0.4	0.4	0.0	0.0
AGB M 23	6.72	4.22	-4.98	-6.59	-7.28	-14.28	-16.58	0.43	110	-1.46	0.2	0.4	0.4	0.0	0.0
AGB M 25	7.80	5.20	-4.40	-6.08	-6.80	-14.30	-16.80	0.24	110	-1.84	0.2	0.4	0.4	0.0	0.0
AGB C 01	1.42	-1.97	-6.02	-6.88	-7.41	-8.55	-8.65	0.84	220	0.69	1.0	0.0	0.1	1.0	1.0
AGB C 03	1.55	-1.52	-6.01	-6.88	-7.41	-8.57	-8.87	0.82	220	1.06	1.0	0.0	0.1	1.0	1.0
AGB C 05	2.42	-0.86	-5.96	-6.88	-7.45	-8.79	-9.29	0.70	220	-0.39	0.8	0.1	0.1	1.0	1.0
AGB C 07	0.08	-2.03	-6.31	-7.19	-7.64	-8.67	-9.37	0.76	220	-0.90	0.8	0.1	0.1	0.0	0.0
AGB C 09	-0.29	-2.40	-6.68	-7.56	-8.01	-9.04	-9.94	0.59	220	-1.02	0.8	0.1	0.1	0.0	0.0
AGB C 11	0.81	-2.19	-6.74	-7.64	-8.19	-9.19	-10.29	0.64	220	-1.32	0.8	0.1	0.1	0.0	0.0
AGB C 13	0.68	-2.32	-6.87	-7.77	-8.32	-9.32	-10.62	0.65	220	-1.20	0.8	0.1	0.1	0.0	0.0
AGB C 15	0.57	-2.43	-6.98	-7.88	-8.43	-9.43	-10.93	0.60	220	-1.66	0.6	0.2	0.2	0.0	0.0
AGB C 17	0.38	-2.62	-7.17	-8.07	-8.62	-9.62	-11.32	0.58	220	-1.95	0.6	0.2	0.2	0.0	0.0
AGB C 19	1.33	-1.67	-7.22	-8.12	-8.67	-9.77	-11.67	0.59	160	-1.34	0.4	0.3	0.3	0.0	0.0
AGB C 21	1.24	-1.76	-7.31	-8.21	-8.76	-9.86	-11.96	0.52	160	-1.85	0.4	0.3	0.3	0.0	0.0
AGB C 23	1.32	-1.68	-7.23	-8.13	-8.68	-9.78	-12.08	0.50	160	-2.15	0.4	0.3	0.3	0.0	0.0
AGB C 25	1.17	-1.83	-7.38	-8.28	-8.83	-9.93	-12.43	0.49	160	-2.39	0.2	0.4	0.4	0.0	0.0
AGB CI 01	5.98	2.17	-3.37	-4.66	-5.81	-8.92	-9.02	0.35	270	-0.85	1.0	0.0	0.1	1.0	1.0
AGB CI 03	4.21	1.51	-4.17	-5.27	-6.22	-9.12	-9.42	0.53	270	0.19	1.0	0.0	0.1	1.0	1.0
AGB CI 05	4.20	2.20	-3.14	-4.69	-6.09	-9.69	-10.19	0.65	220	0.33	0.8	0.1	0.1	1.0	1.0
AGB CI 07	2.71	-0.26	-5.57	-6.59	-7.25	-10.09	-10.79	1.06	220	0.36	0.8	0.1	0.1	0.0	0.0
AGB CI 09	1.34	-1.66	-6.97	-7.99	-8.65	-11.49	-12.39	2.90	220	0.31	0.6	0.2	0.2	0.0	0.0
AGB CI 11	1.69	-1.31	-6.61	-7.81	-8.81	-11.81	-12.91	2.21	220	0.16	0.6	0.2	0.2	0.0	0.0
AGB CI 13	1.29	-1.71	-7.01	-8.21	-9.21	-12.21	-13.51	0.93	220	-0.16	0.6	0.2	0.2	0.0	0.0
AGB CI 15	0.49	-2.51	-7.81	-9.01	-10.01	-13.01	-14.51	0.78	220	-1.00	0.4	0.3	0.3	0.0	0.0
AGB CI 17	2.34	-0.66	-5.96	-7.16	-8.16	-11.16	-12.86	1.10	220	-1.74	0.4	0.3	0.3	0.0	0.0
AGB CI 19	4.50	1.50	-3.80	-5.00	-6.00	-9.00	-10.90	0.60	220	-2.59	0.4	0.3	0.3	0.0	0.0
AGB CI 21	4.16	1.16	-4.14	-5.34	-6.34	-9.34	-11.44	0.60	220	-2.59	0.4	0.3	0.3	0.0	0.0

TABLE 2—*Continued*

Type	$M_B$	$M_V$	$M_J$	$M_H$	$M_K$	$M_{12}$	$M_{25}$	$\sigma$	$h_z$ pc	$\log \rho_0$ kpc $^{-3}$	disk	arms	ring	bulge	halo
AGB CI 23	3.82	0.82	-4.48	-5.68	-6.68	-9.68	-11.98	0.60	160	-2.42	0.4	0.3	0.3	0.0	0.0
AGB CI 25	3.48	0.48	-4.82	-6.02	-7.02	-10.02	-12.52	0.60	160	-2.38	0.4	0.3	0.3	0.0	0.0
AGB CI 27	3.14	0.14	-5.16	-6.36	-7.36	-10.36	-13.06	0.60	160	-1.69	0.2	0.4	0.4	0.0	0.0
AGB CI 29	2.80	-0.20	-5.50	-6.70	-7.70	-10.70	-13.60	0.60	160	-1.67	0.2	0.4	0.4	0.0	0.0
AGB CI 31	2.46	-0.54	-5.84	-7.04	-8.04	-11.04	-14.14	0.60	160	-2.22	0.2	0.4	0.4	0.0	0.0
X 1E	0.49	-1.51	-6.51	-8.31	-9.71	-14.31	-15.82	0.37	90	-0.45	0.2	0.4	0.4	0.0	0.0
X 1A	9.20	7.20	2.20	-0.30	-2.80	-14.40	-16.85	0.31	90	-0.24	0.2	0.4	0.4	0.0	0.0
X 2	4.25	2.25	-2.75	-4.65	-7.15	-15.35	-17.75	0.45	90	-0.01	0.2	0.4	0.4	0.0	0.0
X 3	9.29	7.29	2.29	-0.71	-3.71	-16.31	-18.80	0.28	90	-0.70	0.2	0.4	0.4	0.0	0.0
X 4	-1.90	-3.90	-8.90	-10.20	-11.30	-16.80	-17.77	1.41	90	-0.50	0.2	0.4	0.4	0.0	0.0
X 5	-1.18	-3.18	-8.18	-10.28	-12.38	-16.98	-18.88	0.28	90	-0.85	0.2	0.4	0.4	0.0	0.0
T TAURI	7.29	6.01	2.88	2.11	1.74	-1.86	-3.81	1.40	90	4.57	1.0	0.0	0.1	0.0	0.0
PN BLUE	-2.61	-3.32	-3.98	-3.66	-4.37	-11.00	-12.96	1.10	250	-0.02	1.0	0.0	0.1	1.0	1.0
PN RED	0.04	-0.67	-1.33	-1.01	-1.72	-8.35	-12.06	1.35	250	1.26	1.0	0.0	0.1	1.0	1.0
RN BLUE	-0.50	-0.40	-0.18	-0.78	-0.10	-4.05	-5.92	1.73	120	2.15	0.2	0.4	0.4	0.0	0.0
RN RED	-0.50	-0.40	-0.18	-1.13	-0.10	-4.54	-7.65	2.31	120	2.04	0.2	0.4	0.4	0.0	0.0
H II REG	12.53	8.53	5.53	1.53	-1.47	-8.50	-12.26	2.40	90	1.63	0.2	0.4	0.4	0.0	0.0

six classes of star (Xn in Table 2; classes X1E and X1A have an almost identical  $M_{12}$  but silicate emission and absorption features, respectively). To attain such high 12  $\mu$ m luminosities, these sources must be both of high mass (and therefore young) and shrouded by dust. We have therefore assigned them young population scale heights; they usually have very red colors. Where possible, we have assigned them near-infrared and optical colors based upon known counterparts; in other cases, the colors have been estimated. The choice of these colors is relatively unimportant because these sources are ultraluminous only at wavelengths longer than  $K$ ; these sources are rare and red, so at shorter wavelengths they are a less important part of the luminosity function. The number densities of these ultraluminous sources were chosen to match the 12  $\mu$ m luminosity function derived by Volk et al. (1992) in the magnitude range  $-17 \lesssim M_{12} \lesssim -14$ .

The fourth section of Table 2 represents the final stellar type that we consider: the T Tau stars. These are a young stellar population, originally involved in parental molecular clouds so we have assigned them the young disk scale height of 90 pc. However, the velocity dispersion of T Tau stars in the Tau-Aur clouds is 2–3 km s $^{-1}$  (Jones & Herbig 1979) so that, over the duration of their lifetimes as T Tauris ( $1\text{--}3 \times 10^7$  yr), they may drift many tens of parsecs from their birthplaces, as they clearly must if they are to become main-sequence disk stars. Consequently they diffuse out of their parental clouds to populate a much wider region than the clouds occupy (Rucinski & Krautter 1983; de la Reza et al. 1989, and references therein).

We calculated  $(B - V)_0$  and  $M_V$  for T Tau stars in the Taurus-Auriga cloud using the Herbig & Bell (1988) catalog, combining their  $B$  and  $V$  magnitudes with  $A_V$  values given by Cohen & Kuhl (1979). For  $(J - H)_0$  and  $(H - K)_0$  we followed Rydgren et al. (1984) and the unpublished T Tau data base of Cohen, Emerson, & Beichman (1989a). We similarly calculated  $M_{12}$  for the Taurus-Auriga sample discussed by Cohen et al. To assess their space densities we assumed that (1) all main-sequence stars with masses below  $3 M_\odot$  have a T Tau phase; (2) the maximum duration of this pre-main-sequence phase is  $3 \times 10^7$  yr for all stars with core mass  $\leq 1.0 M_\odot$  for which the approach to the main sequence can be quite protracted (this essentially is the maximum age for known T Tau stars, for

example, in NGC 2264: Cohen & Kuhl 1979); and (3) for stars above  $1.0 M_\odot$ , the duration of the T Tau phase is the actual time to achieve Iben's (1965) "point 8," on the zero-age main sequence. For each mass, we evaluated the space density of T Tau stars as the space density for the appropriate main-sequence star multiplied by the fraction of main-sequence lifetime (again from Iben 1965) represented by the duration of the T Tau phase. The sum of all relevant masses of the resulting densities yielded  $\phi = 3.7 \times 10^4$  kpc $^{-3}$  and we encapsulated all T Tau stars into a single category of celestial source.

### 2.2.2. Nonstellar Sources

The final section of Table 2 contains Galactic nonstellar sources. These are planetary nebulae, reflection nebulae, and H II regions. The H II regions were assumed to have a young population scale height, the reflection nebulae a slightly larger scale height (because they are associated with a population of less massive stars), and the planetary nebulae were assumed to have similar scale height to the giant stars from which they form.

For planetary nebulae, we conducted a literature search for associated distances determined by a wide variety of techniques (see, for example, Gathier 1984). Near-infrared photometry came from Whitelock (1985) and optical data from the reference catalog of planetary nebulae of Acker, Marcout, & Ochsenbein (1981). The separation into red and blue planetaries (see Walker et al. 1989) is essentially achieved by defining the "blue" category as nebulae for which  $1.0 < [12] - [25] < 2.7$  and  $0.7 < [25] - [60] < 3.5$ .

Analysis of the sets of blue and red planetary nebulae with known distances indicates that the blue nebulae are essentially all brighter than  $M_{12} = -11$  and comprise  $\sim 5\%$  of all planetary nebulae. *IRAS* detected 30 planetary nebulae within 1 kpc of the Sun. This is  $\sim 40\%$  of all known planetaries within 1 kpc (the others are too old and have faded away at *IRAS* wavelengths). Using this number, we derive a number density of 19 kpc $^{-3}$  for the 250 pc scale height that we have assumed for the planetary nebulae.

For reflection nebulae, we adopted the identifications of illuminating stars and the observed values of  $V$ ,  $B - V$ , and  $U - B$  tabulated by van den Bergh (1966), Herbst (1975), and van



den Bergh & Herbst (1975), along with standard values for intrinsic colors and  $M_V$  for these dominantly OBA stars (e.g., Cruz-Gonzalez et al. 1974). We determined distance moduli ourselves and thence individual  $M_{12}$  values. Our color-color analyses of reflection nebulae yielded estimates for the proportions of the two differently colored populations (blue and red). The division of the 12–25–60  $\mu\text{m}$  plane into these two populations of reflection nebulae is as follows: for blue reflection nebulae,  $1.10 \leq [12] - [25] < 2.30$  and  $[25] - [60] > 2.00$ ; for red nebulae,  $[12] - [25] \geq 2.30$  and  $[25] - [60] > 2.00$ .

We determined the volume out to which our total sample of reflection nebulae was complete by estimating at what distance,  $D$ , the number of nebulae detected by *IRAS* within  $D$ , divided by  $D^2$ , began to decline steeply, after allowance for Poisson statistics. This technique showed that these nebulae were completely sampled out to 500 pc. We subsequently used only this volume-limited sample to derive the 12 and 25  $\mu\text{m}$  mean absolute magnitudes, associated sample standard deviations, and space densities for the populations (by assuming that the illuminating stars had a scale height of 120 pc and using the proportions for red and blue nebulae described above).

We applied the same method to two samples of H II regions drawn from work by Reifenstein et al. (1970) and by Wilson et al. (1970), for which distances were available through radio recombination line velocities. We found that *IRAS* had sampled these completely out to 1 kpc. The resulting volume-limited complete sample provided our estimates of  $M_{12}$  and  $M_{25}$ , and of their space density with the additional assumption that the scale height for the exciting stars of these regions was 90 pc. Shorter wavelength photometry for the H II regions was taken from Gezari et al. (1987).

### 2.2.3. Synthesized Luminosity Functions

In order to compare our source tables with observed luminosity functions, we have used the absolute magnitudes, dispersions, and number densities in Table 2 to synthesize luminosity functions in the  $V$ ,  $K$ , and 12  $\mu\text{m}$  passbands, using the Gaussian representation given by equation (11). These luminosity functions are shown in Figures 1a–1c.

In Figure 1a we compare the  $V$  luminosity function with that used by Bahcall & Soneira (1980) and with that of Allen (1973). The match is good everywhere except at the brightest  $V$  magnitudes where our luminosity function has a higher number density. Our luminosity function, however, is designed to match the entire disk, whereas the other luminosity functions represent solely the solar neighborhood. Since the Sun is located in an interarm region, it is reasonable that the local luminosity function is deficient in luminous stars relative to the total luminosity function. The roll-off at very faint magnitudes is due to our not considering stars later than our “M late V” category; we also have not included white dwarfs in the model.

In Figure 1b we compare the  $K$  luminosity function with that used by Eaton et al. (1984). The two functions are essentially identical, which is not surprising since they have an almost identical origin (Jones et al. 1981). Nevertheless, this figure serves as a useful check on the effect of the formal inclusion into the  $K$  luminosity function of AGB stars, ultraluminous stars, T Tau stars, and nonstellar Galactic sources. It is

important to compare the  $K$  luminosity functions in Figure 1b with that derived by Mamon & Soneira (1982). Our luminosity function is not as steep in the high-luminosity section as that of Mamon & Soneira. We attribute this difference to the large contribution to the  $K$  luminosity function coming from the M stars. These stars are not adequately considered in Mamon & Soneira’s transformation from  $V$  to  $K$ , so their luminosity function is deficient at the brighter luminosities.

In Figure 1c we compare our synthesized 12  $\mu\text{m}$  luminosity function with that used by Volk et al. (1992). The two luminosity functions match well over most of the magnitude range. Our luminosity function extends slightly beyond  $M_{12} = -17$ , and rolls off at the faintest magnitudes (again due to the absence of very low mass dwarfs and white dwarfs in the source table).

### 2.2.4. Normalization

The normalization of the five components of the Galaxy was achieved using the factors  $f_D, f_A, f_r, f_B$ , and  $f_S$  in the five columns at the right of Table 2, the adjacent column of  $\log \rho_0$  values, and four additional factors listed below. The factors listed in the table represent our attempt to break down the *total* disk luminosity function (exponential disk + spiral arms + ring) into its components. We chose to use this *total* disk luminosity function for consistency with that used by Volk et al. (1992). The factors  $f_D, f_A$ , and  $f_r$  (for exponential disk, spiral arms, and ring, respectively) sum to 1.0 in the Volk et al. picture of the Galaxy, in which both the arms and ring are a dominantly young stellar population. In our table, we allow the ring to contain lower mass stars so, for these stars, these three columns no longer add to unity. We have preserved the Volk et al. normalization of the ratio of 1:2:2 for exponential disk:arms:ring for the total population of young stars.

For the disk star normalization, the number density  $\rho_D(S)$  in equation (4) is simply

$$\rho_D(S) = \rho_0(S)f_D(S). \quad (12)$$

The spiral arm star normalization is slightly more complex, because it involves an additional factor  $g_A$ . This factor is simply the ratio of the total surface area of the exponential disk to the area of the part populated by the arms, weighted by the radial exponential decline. We find  $g_A = 5.0$ . The spiral arm number density (see eqs. [4] and [9]) is then

$$\rho_A(S) = \rho_0(S)f_A(S)g_A. \quad (13)$$

Using this normalization, for example, the factors in Table 2 imply that there are, in total, twice as many high-mass stars located in the arms as there are in the smooth exponential disk. The ring normalization requires the factor  $g_r$ , which is the ratio of the total surface area of the disk (weighted by the exponential decline, normalized to unit surface density in the solar neighborhood) to the total surface area of the ring (weighted by its radial decline in surface density, normalized to unit density at  $R_r$ ). We find  $g_r = 25$ . The ring number density  $\rho_r(S)$  is then

$$\rho_r(S) = \rho_0(S)f_r(S)g_r. \quad (14)$$

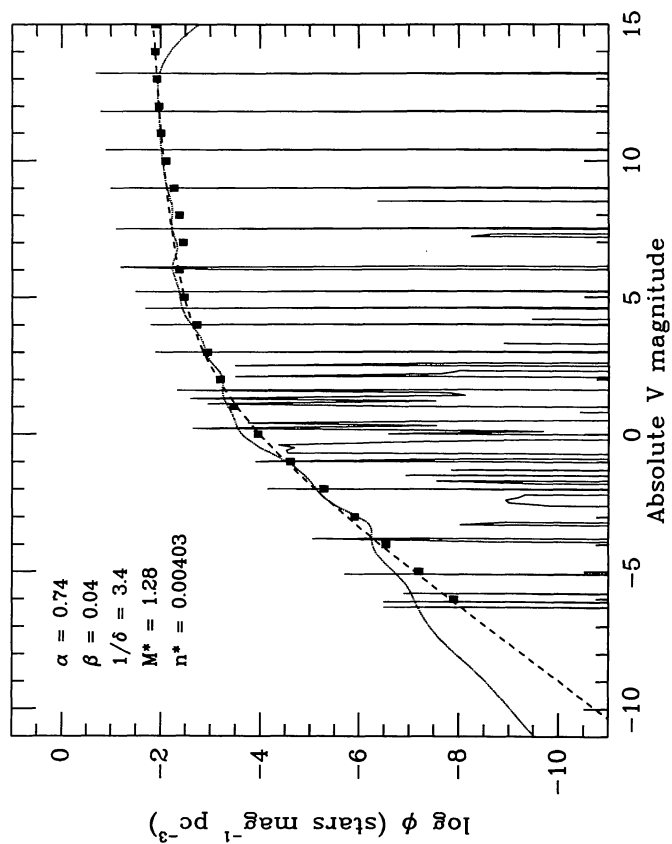


FIG. 1a

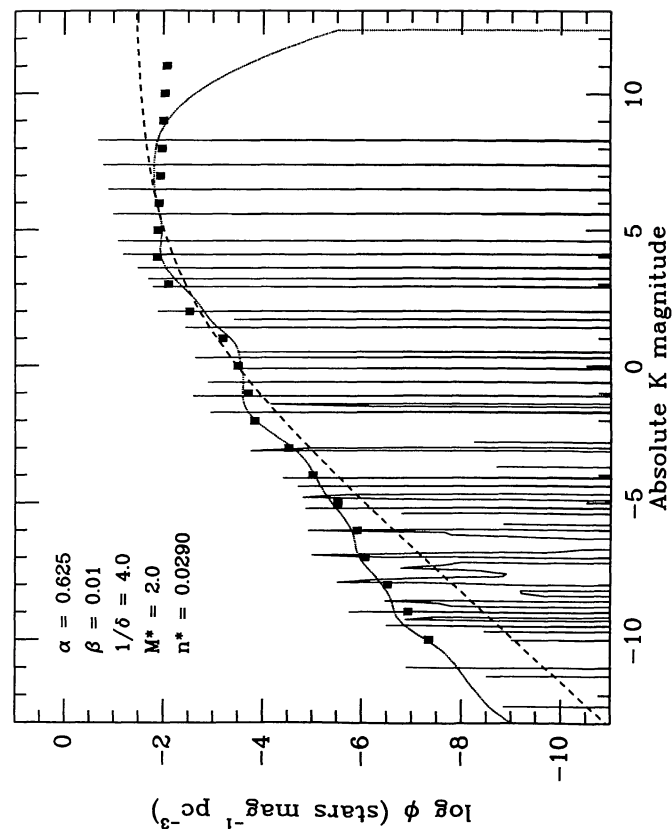


FIG. 1b

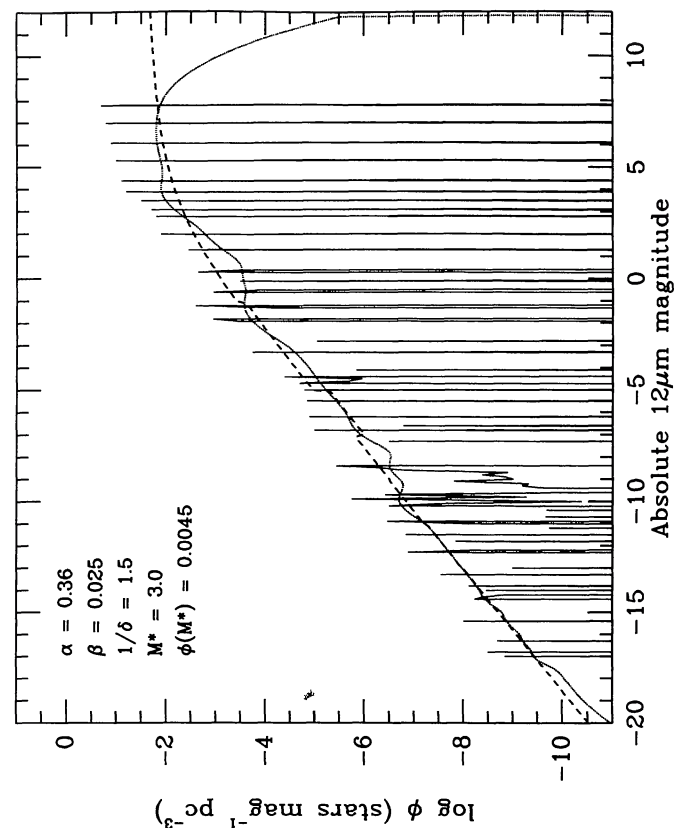


FIG. 1c

Consequently, the factors in Table 2 imply that there are, in total, twice as many high-mass stars located in the ring as there are in the smooth exponential disk. The values of the factors  $f_r(S)$  shown in Table 2 are rather uncertain. The values for the high-mass, luminous stars come from Volk et al. (1992). The values for the lower mass stars are a compromise between an attempt to match the predicted  $K$  star counts from the model to the observations of Eaton et al. (1984), while requiring that the ring does not become an important dynamical component of the Galaxy (rotation curves for the Galaxy do not require a massive ringlike component to be present).

The bulge is normalized using the constant  $g_B$  defined as the ratio of bulge star density at  $x^{-1.8}e^{-x^3} = 1$  (i.e.,  $x = 0.77338$ ) to the local solar neighborhood disk density. We used  $g_B = 3.6$ . The bulge number density  $\rho_B(S)$  (see eq. [5]) is then

$$\rho_B(S) = \rho_0(S)f_B(S)g_B. \quad (15)$$

Finally, the halo normalization is given by

$$\rho_S(S) = \rho_0(S)f_S(S)g_S, \quad (16)$$

where  $g_S = 0.002$  and  $\rho_S(S)$  is the local number density of stars of class  $S$  in the halo.

### 2.3. Low Resolution Spectrometer Spectra

For the purposes of this model we wished to accommodate any view of the point source sky through a filter whose band-pass fitted entirely within the continuous wavelength range sampled by *IRAS*, namely the LRS range (7.67–22.74  $\mu\text{m}$ ). To this end, we required that every one of our 87 classes of Galactic source be represented by an appropriate LRS spectrum.

All LRS spectra that we have used have been modified by the small calibration correction factors derived by Volk & Cohen (1989).

#### 2.3.1. Stars

LRS spectra for most types of “normal” star were available from the LRS Atlas (1986). We used the entire LRS data base to supplement the number of spectra for a particular class of star when the signal-to-noise ratio in the relevant Atlas spectrum was poor or for types under-represented in the Atlas (such as cool dwarf stars). We normalized all the LRS spectra to unity, to facilitate ready combination of several spectra to achieve an average for one source type. For our “young OB” category, we combined the spectra of HD 21389 (A0 Iae),  $\beta$  Ori (B8 Iae:),  $\zeta$  Pup (O5 Iaf), and  $\gamma^2$  Vel (WC8+O7.5e). For dwarfs later in type than M0 V, we were able to locate very few adequate LRS spectra even in the data base. However, we readily determined that our actual LRS spectra for all cool dwarf stars beyond M0 V were well matched by cool ( $T = 3500$

K) blackbodies. Consequently, we substituted these cool blackbody curves for the real but noisy LRS spectra, and for spectral types not represented in the LRS data base, to produce a complete grid of LRS stellar spectra for “normal” stars. These substitutions were employed for types M0,1 V and M4,5 V; we were able to locate a suitable real spectrum for type M2 V.

In order to provide archetypical LRS spectra largely from the LRS data base, it was necessary to smooth a number of the normalized spectral averages. Source categories whose averages were of sufficient quality to use directly (or which showed spectral lines making it undesirable to smooth the spectra) were B2–3 V; M0,1,2,3,4,5,6,7 III; M3–4 I–II; K–M2 I; blue and red reflection nebulae; red planetary nebulae; and H II regions. When smoothing, we used a Gaussian of half-width 5 channels; this was applied to all other source categories except K4–5 V, M0–1 V, M4–5 V, and M late V for which we used a 3500 K blackbody.

For cool giants and AGB stars, we subdivided the sources into different categories depending on their oxygen- or carbon-richness, and on their  $[12] - [25]$  colors, binning these into 0.2 mag intervals. We assembled two sub-data bases of *IRAS* point sources: one consisted of all sources associated either with Atlas spectra corresponding to silicate emission (LRS classes 20–29), or absorption (LRS classes 30–39), or optically known M stars in the GCVS; the second sub-data base included only those point sources whose Atlas spectra we had already inspected and validated as having SiC emission characteristic of carbon stars (after exclusion of any silicate self-absorbed spectra—see Walker & Cohen 1988).

We then extracted the Atlas spectra for all objects from the subset of 2958 oxygen-rich stars having  $0.0 < [12] - [25] < 3.2$ . These spectra were then normalized and averaged to represent AGB stars with  $[12] - [25]$  colors of 0.1, 0.3, . . . , 3.1, where, for example, we represent stars with  $1.0 < [12] - [25] \leq 1.2$  as having a single color of  $[12] - [25] = 1.1$ . The sizes of the samples that defined these average spectra are shown in Table 3. We averaged the LRS spectra for indices of 2.7 and 3.1 to interpolate a spectrum for  $[12] - [25] = 2.9$ . We show the sequence of LRS spectra for O-rich giants in Figure 2a. Table 3 also shows the breakdown by  $[12] - [25]$  color of our sub-data base of 802 Atlas spectra of carbon giants. No SiC emitting sources are known with redder broad-band colors than 1.9; we chose to use the  $[12] - [25] = 1.9$  spectrum to represent the LRS spectra of the carbon stars in our source table (Table 2) with  $[12] - [25] > 2.0$ . We show the sequence of LRS spectra for C-rich giants in Figure 2b. We used the same set of LRS spectra to represent the optically visible and the optically invisible carbon stars.

We discovered adequate LRS data base spectra for 25 of the 51 objects chosen to typify the most luminous 12  $\mu\text{m}$  objects in the Galaxy, then grouped all the objects according to their

FIG. 1.—Synthesized luminosity functions. (a) The  $V$  luminosity function. The “spikes” show the 87 categories of source in our model by assuming that they have no dispersion but instead are found in a magnitude range of width 0.10 mag. The dashed line is the  $V$  luminosity function used by Bahcall & Soneira (1980), with parameters detailed at the top left corner of the figure. The dots show the luminosity function given by Allen (1973). The dotted line is the composite derived from our 87 types of sources, using the  $M_V$  and  $\sigma$  values for each class of source given by Table 2. (b) As for (a), for  $K$ , except that the dashed line shows the  $K$  luminosity function derived by Mamon & Soneira (1982) and the dots show the luminosity function used by Eaton et al. (1984). (c) As for (a), for 12  $\mu\text{m}$ , except that the dashed line shows the 12  $\mu\text{m}$  luminosity function used by Volk et al. (1992).



TABLE 3  
NUMBERS OF LRS SPECTRA OF AGB  
STARS USED TO CONSTRUCT COMPOSITE  
LRS SPECTRA

[12] – [25]	O-rich	C-rich
0.1 .....	83	52
0.3 .....	119	190
0.5 .....	239	131
0.7 .....	370	87
0.9 .....	434	69
1.1 .....	401	55
1.3 .....	276	33
1.5 .....	123	10
1.7 .....	56	5
1.9 .....	34	1
2.1 .....	37	...
2.3 .....	27	...
2.5 .....	13	...
2.7 .....	7	...
2.9 .....	0	...
3.1 .....	1	...

values of  $M_{12}$  and LRS spectral class. Figure 2c shows the average spectra of the six classes to which we assigned the 25 ultra-luminous sources with acceptable LRS spectra.

Although several of the T Tau stars are represented in the LRS data base, too few are available to establish the frequencies of occurrence of different LRS shapes for these stars. However, ground-based 8–13  $\mu\text{m}$  spectroscopy (Cohen & Wittborn 1985) indicates that  $\sim 80\%$  of the T Tau stars studied show 10  $\mu\text{m}$  silicate emission features and 20% show silicate absorptions. We, therefore, chose to represent the T Tau category by the normalized LRS average spectrum of ( $2 \times \text{RY Tau} + 2 \times \text{GW Ori} + \text{R Mon}$ ), where RY Tau and GW Ori are silicate emission T Tau stars, and R Mon is a silicate absorption T Tau star. Figure 2d displays the resulting LRS spectrum.

### 2.3.2. Galactic Nonstellar Objects

For nebulae, we sought LRS data base spectra for every object of that particular category for which we had found an association in the PSC. In all cases we found that more than one LRS shape characterized the populations, although some of these diverse shapes corresponded to peculiar, incomplete, or noisy spectra.

H II regions presented the cleanest situation with essentially one dominant LRS spectral signature and only four frequently occurring usable shapes; planetary nebulae had seven different categories of usable spectrum (treated in more detail by Volk & Cohen 1990); reflection nebulae similarly had six categories. We excluded all unusable (incomplete or noisy) spectra and selected one object whose LRS spectrum was of good quality to represent each category for every nonstellar source. We generated normalized composite LRS spectra by combining these representatives, weighted by their actual frequencies of occurrence within the LRS data base, into a single LRS spectrum. We were careful only to combine spectra for objects with similar [12] – [25] indices so that normalizations at very different peak wavelengths would not bias the average LRS shape

improperly. In practice, our distinctions drawn from the color-color planes, between red and blue planetaries, and red and blue reflection nebulae, were sufficient to ensure that only LRS spectra for similarly colored objects were combined. Figures 2d–2e present these LRS average spectra.

### 2.3.3. Use of Nonstandard Filters

By utilizing the LRS spectra described above, our model can calculate (with a confidence level similar to that at 12 or 25  $\mu\text{m}$ ) expected source counts for any passband lying wholly within the *IRAS* LRS wavelength range of 7.67–22.74  $\mu\text{m}$ . This is achieved in the following way. First, the absolute 12  $\mu\text{m}$  magnitudes for each class of source (see Table 2) are used to calibrate absolutely the characteristic LRS spectrum for each class. Next, each calibrated spectrum is integrated over the bandpass of interest, resulting in a flux from each source (at a distance of 10 pc). A  $\lambda F_\lambda = \text{constant}$  emission profile is used to define an effective wavelength for the bandpass, and a magnitude scale is then defined using equation (VI.C.1) in the *IRAS* Explanatory Supplement (1988). (Note that this choice of magnitude scale is solely for convenience.) Finally, the observed fluxes for each class are transformed to this new magnitude scale. Computationally, the new “absolute magnitudes” are then handled in exactly the same way as for the normal broad-band filters (e.g., [12],  $K$ ). After the integration through the Galaxy and then through extragalactic space is complete (resulting in a  $[\log N, \text{mag}]$  relationship), the transformation from flux to magnitude is applied in reverse to deliver the desired quantity—in-band flux—and a  $[\log N, \log F]$  relationship.

### 2.4. Interstellar Extinction

Our model requires a representation of the interstellar extinction curve over the full LRS wavelength grid. This is used both to derive the interstellar extinction in any arbitrary filter in the LRS wavelength range and to derive the interstellar extinction in the 12  $\mu\text{m}$  filter used by *IRAS*.

Rieke & Lebofsky (1985, hereafter RL) have calculated the interstellar extinction law  $A_\lambda/A_V$  in the wavelength range 8–13  $\mu\text{m}$ , at a resolution of  $\Delta\lambda \approx 0.5 \mu\text{m}$ . Their determinations were based on a study of heavily extinguished luminous early-type stars and sources in the vicinity of the Galactic center. To define the extinction law in full-wavelength detail, we initially extracted the LRS data base spectra for VI Cyg No. 12, the canonical heavily reddened B5 Ia star. The chief attraction of this star was the prospect of simultaneously defining the spectral shape of the interstellar 18  $\mu\text{m}$  absorption feature, which has never been investigated in detail, and the well-studied 10  $\mu\text{m}$  interstellar feature (often represented by the shape of the Orion Trapezium emission spectrum; Forrest, Gillett, & Stein 1975).

We examined the average of four independent LRS spectra of VI Cyg No. 12 with varying qualities of the blue and red LRS spectral sections, but all having essentially similar spectral shapes. However, we were never able to match satisfactorily the dereddened broad-band energy distribution of this star and its LRS spectrum with any blackbody, in particular with one close to 14,000 K in temperature (corresponding to spectral type B5 I). The definition of the intervening extinction using

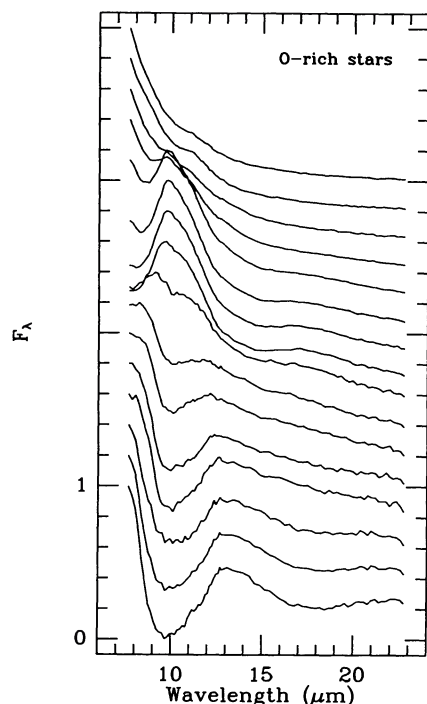


FIG. 2a

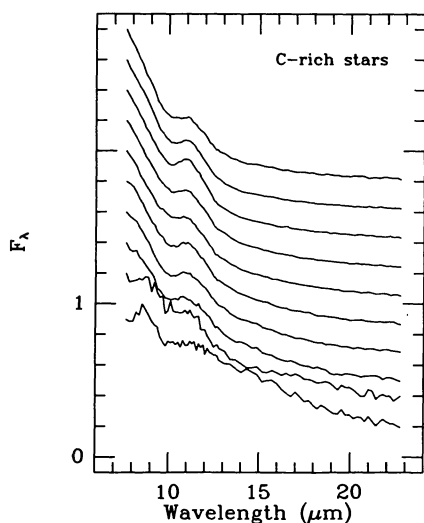


FIG. 2b

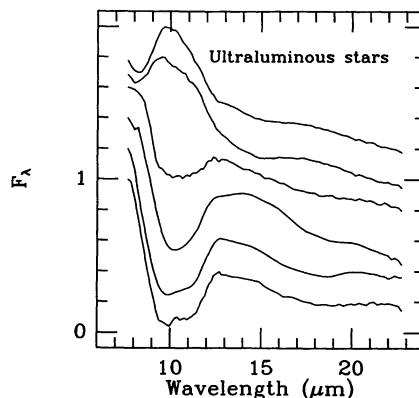


FIG. 2c

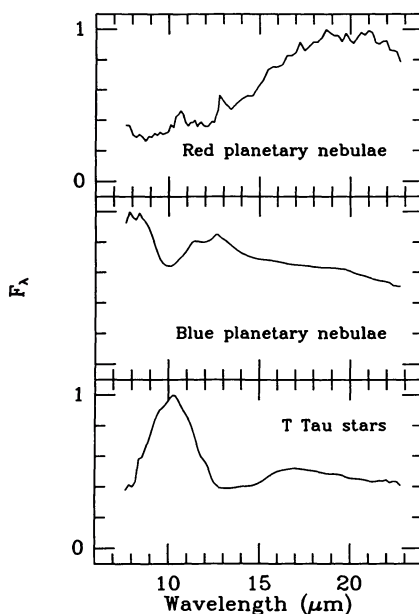


FIG. 2d

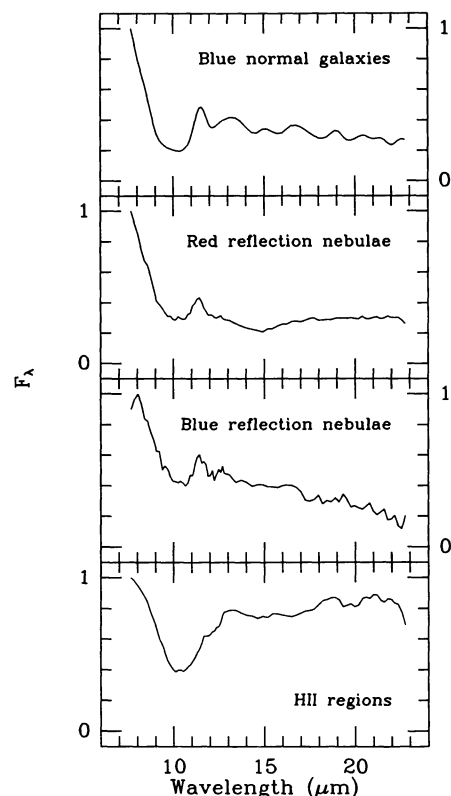


FIG. 2e

FIG. 2.—Representative LRS spectra of Galactic sources. Each spectrum is in units of  $F_\lambda$  and has been normalized to unity at its maximum. (a) O-rich giants. Each spectrum has been offset from its neighbor by 0.2 and is normalized to unity. The spectra are, from top to bottom, for characteristic  $[12] - [25]$  colors of 0.1, 0.3, ..., 3.1. (b) C-rich giants. Each spectrum has been offset from its neighbor by 0.2. The spectra are, from top to bottom, for characteristic  $[12] - [25]$  colors of 0.1, 0.3, ..., 1.9. (c) Ultraluminous stars. Each spectrum has been offset from its neighbor by 0.2. The spectra are, from bottom to top, X3, X1A, X2, X5, X1E, X4. (d) T Tau stars and planetary nebulae. (e) H II regions, reflection nebulae, and "blue normal" galaxies.

the ratio of the LRS spectrum to such a blackbody depends too critically on the accurate and simultaneous normalization of the blackbody to the dereddened broad-band photometry and to the peak of the LRS data, near  $8 \mu\text{m}$ . A further problem with VI Cyg No. 12 is its peculiarly flat energy distribution in the range  $15\text{--}23 \mu\text{m}$ . No photosphere can match this shape. Indeed, it is possible that the stellar photosphere is no longer the

primary source of emission at these long wavelengths—free-free emission from the stellar wind may dominate the energy distribution (Leitherer et al. 1984; Barlow & Cohen 1977). If so, free-free radiation may likewise contaminate the spectrum even shortward of  $15 \mu\text{m}$ .

Consequently, we abandoned our effort to use this star. Instead, we examined two normalized average LRS spectra: for

401 *IRAS* sources having  $1.05 < [12] - [25] < 1.15$  with optically thin silicate emission at 10 and 18  $\mu\text{m}$ ; and for the only *IRAS* source with  $3.0 < [12] - [25] < 3.2$  having deep silicate absorptions at both 10 and 18  $\mu\text{m}$ . In each case, we spline interpolated the underlying continuum between the two silicate features to remove the nonsilicate contributions and compared the resulting “excess emission” and “excess absorption” profiles in the 10  $\mu\text{m}$  region to that created by spline fitting the 11 calculated broad-band values of  $A_\lambda/A_V$  of RL onto the LRS set of wavelengths and normalizing. The 10  $\mu\text{m}$  “excess emission” profile was much narrower than the splined RL law, whereas the absorption data yielded a close match. We, therefore, adopted the entire normalized absorption profile defined from the source having both the silicate absorption features to represent the silicate aspect of interstellar extinction.

Outside the 10  $\mu\text{m}$  silicate band there is also extinction, and we adopted a  $\lambda^{-1}$  law for the nonresonant extinction by these grains, scaled to correspond closely at 7.67  $\mu\text{m}$  (the shortest LRS wavelength) to the RL value of  $A_\lambda/A_V = 0.020$  at  $\lambda = 8.0$   $\mu\text{m}$ . Because this component underlies the silicate features we scaled the silicate extinction profile so that the sum of the non-silicate and silicate extinctions closely matched the actual peak value in the RL data (near 9.5  $\mu\text{m}$ ). The resulting extinction law appears in Figure 3.

Rigorous treatment of extinction would require that the derived extinction law be applied at every LRS wavelength for each object. Fortunately, such a detailed treatment is not necessary; the approximation  $A_P = \int R_\lambda A_\lambda / \int R_\lambda$ , where  $R_\lambda$  is the response function of passband  $P$ , is sufficient provided that the passband is not too broad. The interstellar extinction is not high enough in the mid-infrared to warrant more detailed treatment—we have, therefore, adopted this approximation in our model. In this way, we derive  $A_{12}/A_V = 0.048$  for the *IRAS* 12  $\mu\text{m}$  filter. Since the *IRAS* 25  $\mu\text{m}$  passband lies partially outside the LRS wavelength range, we could not use this tech-

nique to derive  $A_{25}$ . We extrapolated our detailed LRS extinction law by the  $\lambda^{-1}$  and calculated  $A_{25}/A_V \approx 0.005$ .

The interstellar extinction (dust) was assumed to be located solely in the disk of the Galaxy and to have a smooth exponential distribution, similar in form to the disk stellar distribution. This is an idealized representation; we expect that the dust has a somewhat clumpy distribution and that it has concentrations in the spiral arms and molecular ring—it is difficult to represent such a distribution analytically. However, the absorption is relatively low in the mid-infrared, so our simple dust distribution should be adequate. The absorption in an interval  $D$  to  $D + \delta D$  was assumed to be

$$\delta A_\lambda(R, z) = \begin{cases} A_{\lambda 0} \exp [-(R - R_0)/h_d - |z|/h_{zd}] \delta D & R < R_{\max} \\ 0 & R > R_{\max} \end{cases}, \quad (17)$$

where  $A_{\lambda 0}$  is the absorption per unit length in the solar neighborhood,  $h_d$  is the radial scale length of the absorption,  $h_{zd}$  is the scale height of the absorption, and  $D$  is distance along the line of sight to position  $(R, z)$ . We assumed that the dust absorption in the solar neighborhood is 0.07 mag  $\text{kpc}^{-1}$  at  $K$ . This corresponds to  $A_{V0} = 0.62$  mag  $\text{kpc}^{-1}$  using the interstellar extinction law determined by RL. Jones et al. (1981) derived a radial scale length for the extinction of 4 kpc. This value is similar to values derived for the scale length of the stars in the disk (3.5 kpc; de Vaucouleurs & Pence 1978; 4.4 kpc, Lewis & Freeman 1989; 5.5 kpc, van der Kruit 1986). We, therefore, assumed that the scale length of the absorption was the same as that of the stars, so  $h_d = h$ . We used a value of  $h_{zd} = 100$  pc for the extinction scale height.

For Galactic sources, the extinction calculation was carried out in parallel with the source count calculation. At each step along the line of sight, the source numbers and magnitudes were calculated, along with the extinction due to that increment in distance. The sources were assumed to be located at the midpoint of the step: half of the extra extinction was added to the total extinction to that point along the line of sight; the sources were dimmed by that “total” extinction, then the other half of the extinction increment added to the total. When the “edge” of the Galaxy is reached, the total Galactic absorption along that line of sight has been calculated; this was used as the extinction for the extragalactic sources. Intergalactic absorption was assumed to be negligible.

### 2.5. Integration through the Galaxy

The integration through the Galaxy is performed by stepping along a ray which starts at the Earth and goes along the appropriate line of sight to infinity. Because they are the natural units for use in this work, we adopt Galactic coordinates  $(l, b)$  as the standard input. If a large area is to be studied, or the area being studied has a large number density gradient (e.g., near the Galactic center or near the Galactic plane), we arrange a grid [in  $(l, b)$  coordinates] of suitably chosen,

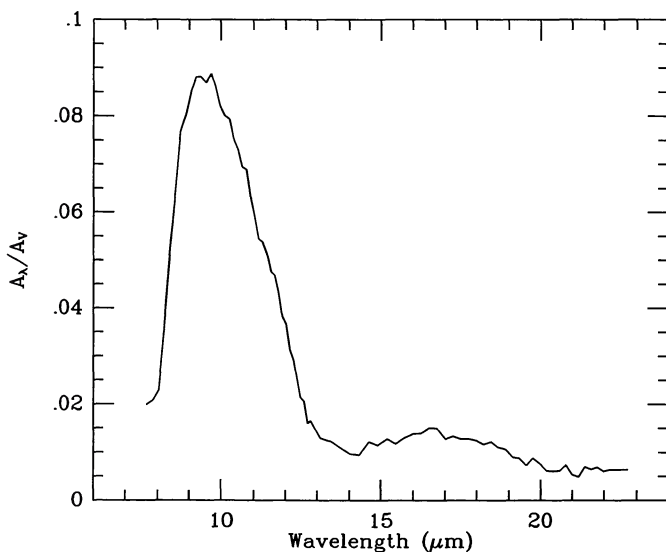


FIG. 3.—Interstellar extinction law. The interstellar extinction, expressed as  $A_\lambda/A_V$ , over the LRS spectral range.



equally spaced, rays across the area, integrate along each ray, then sum their contributions (weighted by  $\cos b$ ).

The integration along each ray is performed by regarding each ray as corresponding to a cone subtending a solid angle of  $1 \text{ deg}^2$ . (The results can be scaled to the appropriate observed area later.) The cone is split into volume elements, starting with the element  $0 < D < 2 \text{ pc}$ . The volume of the element is calculated then, for each of the five Galactic components, the contribution from each class in the source table is calculated for that position and volume. These sources are assumed to be all located at the midpoint of the cone element (this assumption is valid provided that a sufficiently small step size is chosen; step size is discussed in detail below). The extinction to that point is calculated, then the magnitudes for each class of Galactic source at that location calculated.

We have chosen a relatively simple method to represent the Gaussian distribution in magnitude of sources of a particular class. We approximate the Gaussian using the 5  $\delta$ -functions listed in Table 4. Thus, at a particular location, stars of each class are assumed to have five different magnitudes (with appropriate number weighting). In this way, we achieve a computationally simple, yet reasonably realistic representation of the Gaussian. (The Gaussian could be better represented by more  $\delta$ -functions, but a corresponding penalty in computational speed would be incurred.)

The step size that we have chosen ranges from a minimum of 2 pc to a maximum of 80 pc, and is determined from the distance,  $D$ , from the Sun or from the distance,  $xR_1$ , from equation (6). If either of these distances is less than 100 pc, the 2 pc step is used; a 4 pc step is used if  $100 \leq (D \text{ or } xR_1) < 300 \text{ pc}$ ; 8 pc if  $300 \leq (D \text{ or } xR_1) < 700 \text{ pc}$ ; 16 pc if  $700 \leq (D \text{ or } xR_1) < 1500 \text{ pc}$ ; 32 pc if  $1500 \leq (D \text{ or } xR_1) < 3100 \text{ pc}$ ; 64 pc if  $3100 \leq (D \text{ or } xR_1) < 6300 \text{ pc}$ ; and 80 pc if  $6300 \leq (D \text{ and } xR_1) \text{ pc}$ . The integration proceeds along the ray using these step sizes until a user-defined distance,  $D_{\text{max}}$ , is reached. At this point, the integration through the Galaxy is complete. For our model, we have assigned  $D_{\text{max}} = 25 \text{ kpc}$ . For comparison with deep optical star counts, this value is probably too small and could be increased.

As the integration through the Galaxy proceeds, we collect the counts for each class of star, in each of the five Galactic components, into magnitude bins. We chose to use bins of 0.25 mag. Therefore, when the integration is complete, the breakdown of the star counts among each of the Galactic components is available, as is the breakdown within each of the components into its constituent stellar classes. This will permit future direct spectroscopic and photometric tests of the detailed model predictions, as well as giving a clear picture of

what stellar classes and Galactic components are dominant. The classes and components are finally summed to yield either differential or cumulative total counts versus magnitude relations, and the familiar ( $\log N$ ,  $\log F$ ) diagrams (see § 4).

### 3. THE EXTRAGALACTIC SKY

We now discuss the methods by which we have represented extragalactic sources in our sky model, including their colors, their separation into diverse types of galaxy, and their luminosity functions. The treatment of galaxies differed from that of Galactic sources since we assumed that they have an isotropic distribution (we have ignored any effects due to individual galaxy clusters or to the supergalactic plane). Hence, there will always be the same contribution from galaxies at a given wavelength, scaled solely by the area of the sky zone chosen, except that interstellar extinction along the line of sight within the Galaxy makes the apparent distribution of galaxies anisotropic.

#### 3.1. Colors and Luminosity Functions

By their nature, nearby galaxies can subtend angles greater than the *IRAS* survey beam sizes, at least at 12 and 25  $\mu\text{m}$ , which might influence their color distributions. Walker et al. (1989) have compared PSC colors of galaxies with the spatially integrated colors from the sample of *IRAS* observations of large galaxies by Rice et al. (1988), and have found essentially no need to redefine the occupation zones for galaxies in the color-color planes. The slight differences that these authors did find were explicable in terms of the increased effective beam sizes inherent in spatially integrating the 12 and 25  $\mu\text{m}$  maps of these galaxies.

From the color-color planes one can study the distribution of colors of different galaxy types. We found it convenient to divide galaxies into “normal galaxies,” “Seyfert galaxies,” and “quasars” based on *IRAS*-related studies in the literature; “starburst” galaxies seem to overlap strongly with the luminosities and *IRAS* colors of normal galaxies (see Soifer et al. 1987) so we combined the two. When we extracted all sources from the PSC associated with extragalactic catalogs we were able to define color-color diagrams for a sample of 11,595 galaxies.

However, we decided that such an approach had two inherent problems: (1) it would show a clear bias toward optically peculiar galaxies (for example, Seyfert galaxies) that had been cataloged as of particular interest and would thereby overestimate the true incidence of Seyfert galaxies; and (2) it would not treat *IRAS* upper limits correctly by addressing the color-dependent flux thresholds at 12 and 25  $\mu\text{m}$  where most galaxies are not bright. We, therefore, used a  $4000 \text{ km s}^{-1}$  volume-limited sample to assess the colors of galaxies, drawn from the larger study by Strauss & Davis (1988). This study essentially includes only the categories of normal and starburst galaxies; it does not sample high-luminosity galaxies. However, it provides a clear quantitative estimate of the relative populations of “blue” (65%) and “red” (35%) normal galaxy types (see Walker et al. 1989) defined by the projection of the volume-limited sample onto the [12] – [25] axis. For all types, we used Gaussians to represent the color indices of galaxies in the three independent *IRAS* colors, with appropriate means and sigmas. In [25] – [60], normal galaxies show a well-defined peak

TABLE 4  
REPRESENTATION OF GAUSSIAN BY DELTA FUNCTIONS

Magnitude Range	Location ( $\sigma$ )	Fraction
$(-\infty, -1.5 \sigma)$ .....	-1.939	0.0668
$(-1.5 \sigma, -0.5 \sigma)$ .....	-0.921	0.2417
$(-0.5 \sigma, +0.5 \sigma)$ .....	0.000	0.3830
$(+0.5 \sigma, +1.5 \sigma)$ .....	0.921	0.2417
$(+1.5 \sigma, +\infty)$ .....	1.939	0.0668

which we fitted by using two Gaussians, preserving both the integrity and the proportions of the blue and red galaxies. There is also a weak blue component in the distribution, corresponding to the contribution from Seyfert galaxies (and quasars) in this color. We found that the area of this tail represents  $\sim 4\%$ – $5\%$  of the total projected color distribution and attributed this entirely to Seyfert galaxies.

For more exotic galaxies, we follow Walker et al. (1989) in using the colors of Seyfert galaxies and quasars found by Miley, Neugebauer, & Soifer (1985) and Neugebauer et al. (1986).

Since galaxies are most easily seen by *IRAS* at  $60\ \mu\text{m}$ , we sought a luminosity function defined at  $60\ \mu\text{m}$ . Two groups have discussed such a function for galaxies. After correction to a common value of  $H_0 = 75\ \text{km s}^{-1}\ \text{Mpc}^{-1}$ , we found little difference between the double power law of Soifer et al. (1987) and the smoother representation offered by Lawrence et al. (1986) except at the highest luminosities ( $M_{60} \lesssim -40$ , or  $L \gtrsim 2 \times 10^{12} L_\odot$ ). The Lawrence et al. luminosity function is steeper (slope  $-2.5$  in  $[\log_{10} L, \log_{10} \rho]$ ) than the Soifer et al. luminosity function (slope  $-2.0$ ). We chose to use the double power-law representation of Soifer et al. for the luminosity function of galaxies at  $60\ \mu\text{m}$  because it has a simpler analytical representation. We defined the luminosity function as

$$\rho(M_{60}) = \begin{cases} 0 & M_{60} < -44.0; \\ \rho_b 10^{0.80(M_{60}-M_b)} & -44.0 \leq M_{60} < M_b; \\ \rho_b 10^{0.32(M_{60}-M_b)} & M_b \leq M_{60} < -26.0; \\ 0 & -26.0 \leq M_{60}; \end{cases} \quad (18)$$

where  $\rho_b = 7.6 \times 10^{-4}\ \text{Mpc}^{-3}\ \text{mag}^{-1}$  is the number density at the break in the double power law, and  $M_b = -34.43$  is the  $60\ \mu\text{m}$  absolute magnitude at which the break occurs. These values differ slightly from the values given by Soifer et al. in the following ways. First, the luminosity function of Soifer et al. is defined for color-corrected  $F_\nu(60\ \mu\text{m})$  whereas we are interested in matching the observed quantity, in-band flux. We have crudely corrected for this by assuming that galaxies located in the flat part of the double power law (with  $M_b \leq M_{60} < -26.0$ ) have  $T < 32\ \text{K}$  and have negligible color corrections, whereas galaxies located in the steep part of the double power law (with  $-44.0 \leq M_{60} < M_b$ ) have a color correction of 0.91 (typical for warmer galaxies with  $T > 32\ \text{K}$ ). This has the effect of producing a small shift in  $M_b$  and a corresponding small change in  $\rho_b$ . Also, our value of  $\rho_b$  has been scaled by 0.96 relative to that fitted from the Soifer et al. luminosity function to compensate for the somewhat lower density of galaxies in the southern sky; the Soifer et al. sample comes primarily from the northern sky. The magnitudes of  $-26.0$  and  $-44.0$  represent the faintest and brightest sources that were considered. Our absolute magnitude is related to the luminosities defined by Soifer et al. through  $M_{60} = -9.03 - 2.5 \log_{10}(\nu L_\nu \text{ at } 60\ \mu\text{m}, \text{ in } L_\odot)$ .

It is not yet clear how the  $60\ \mu\text{m}$  galaxy luminosity function should be decomposed into normal/starburst galaxies, Seyfert galaxies, and quasars. We have chosen the following approach. First, we assumed that for  $M_{60} < -41$ , all sources were quasars or had the colors of quasars, and that in the range  $-41 < M_{60} < -33.5$ , the quasar luminosity function had the same slope

( $-0.8$ ) as the flat part of the total luminosity function, thus resulting in a fairly rapidly decreasing fraction of quasars with fainter magnitudes. Objects such as *IRAS* 09104+4109 (Kleinmann et al. 1988), have luminosities placing them in this quasar range; in spite of the fact that they are not quasars, they have similar infrared colors to quasars (for *IRAS* 09104+4109,  $[12] - [25] = 2.49$ ,  $[25] - [60] = 2.33$ ) so are consistent with our picture. Next, we assumed that Seyfert galaxies (or galaxies with the colors of Seyferts) exist in the magnitude range  $-41 < M_{60} < -29$ , and comprise a total of 4% of all galaxies at the lower luminosities, with this fraction increasing to 10% of the nonquasar population at the higher luminosities. This strategy has the merit of being consistent with the statement of Lawrence et al. (1986) that “*IRAS* galaxies are probably 10–25 times as common as all types of Seyfert galaxy” and also predicts the correct relative proportion of galaxies with Seyfert-like colors in the volume limited sample of Strauss & Davis (1988). We attribute the remainder of the luminosity function to galaxies with the colors of normal/starburst galaxies, and to the blue/red categories of these normal/starburst galaxies in the ratio 65:35. Figure 4 summarizes our breakdown of galaxy types.

Having settled upon the  $60\ \mu\text{m}$  luminosity function and the breakdown of this function into its four constituent types, we are able to calculate the luminosity function for galaxies in other passbands. We assumed that the colors had Gaussian distributions; Table 5 lists the mean and sigmas of the  $[12] - [25]$  and  $[25] - [60]$  color distributions for our four classes of galaxy. The values in this table are the same as those derived by Walker et al. (1989) except that (1) the magnitude definitions in equations (1)–(3) have been used; and (2) we have now preserved the integrity of the  $[12] - [25]$  blue and red samples in the  $[25] - [60]$  color projection.

If a wavelength shorter than  $60\ \mu\text{m}$  was to be modeled, it was necessary first to transform the  $60\ \mu\text{m}$  luminosity function to  $25\ \mu\text{m}$ . This was achieved by first separating the four classes of galaxy, then calculating the contribution at each  $M_{25}$  from

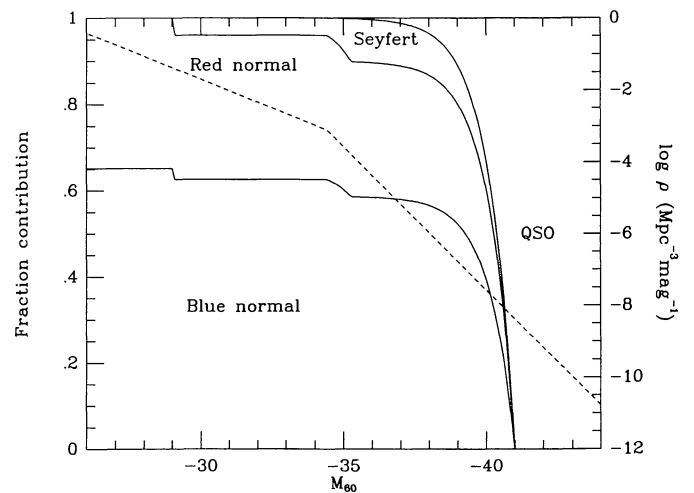


FIG. 4.—Breakdown of galaxy types. The assumed breakdown of galaxy types into “blue” and “red” “normal” galaxies (these categories include starburst galaxies), Seyfert galaxies, and quasars. The dotted line shows the double power law on the same magnitude scale.

each value of  $M_{60}$ , assuming the  $[25] - [60]$  colors had the Gaussian distributions detailed in Table 5. If  $25\ \mu\text{m}$  was the passband for modeling, the four components of the luminosity function were summed to produce the composite  $25\ \mu\text{m}$  luminosity function; otherwise, the  $12\ \mu\text{m}$  luminosity function was calculated similarly, using the  $[12] - [25]$  colors. If  $12\ \mu\text{m}$  was the passband of interest, the four components were added to yield the  $12\ \mu\text{m}$  luminosity function for extragalactic sources. If, on the other hand, a filter in the LRS wavelength range was to be modeled, characteristic LRS spectra (see § 3.2 below) for the four classes of galaxy were used, in a procedure completely analogous to that described for Galactic sources in § 2.3.3, to define four separate offsets in the magnitude scale. Finally, these four offsets were separately applied to the four components of the  $12\ \mu\text{m}$  luminosity function, and the result regridded and summed to yield the composite  $M_P$  luminosity function for passband  $P$ . Figure 5 shows the 12 and  $25\ \mu\text{m}$  luminosity functions for extragalactic sources, calculated in this way; the  $60\ \mu\text{m}$  luminosity function is shown for comparison. We have not attempted to model the extragalactic sky at wavelengths shorter than the LRS limit of  $7.7\ \mu\text{m}$ .

### 3.2. Low-Resolution Spectrometer Spectra of Galaxies

As noted above, in order to transform the luminosity function for extragalactic sources to any arbitrary filter within the LRS wavelength range, it is necessary to obtain characteristic LRS spectra for each class of extragalactic source.

The Atlas includes very few galaxies and those that are represented are peculiar (e.g., Cen A; NGC 253; M82). Therefore, we searched the LRS data base for spectra of any PSC objects associated with galaxies whose  $12\ \mu\text{m}$  fluxes promised a usable spectrum. To supplement our sample, we also sought LRS data for the 42 starburst galaxies in the sample chosen by Jackson et al. (1988) for their microwave CO survey—in particular, those nine in which CO emission was detected. Of these 42, we found LRS spectra for four galaxies (NGC 2146, NGC 2903, NGC 3504, and NGC 4490), all of which were detected in CO emission; only the spectrum for NGC 2146 had an adequate signal-to-noise ratio for our purposes.

We finally selected 13 galaxies for which reasonable LRS spectra were available and averaged their normalized shapes which were all very similar and obviously suggest the presence of PAH features in emission (Fig. 2e) (see Cohen & Volk 1989; Cohen 1992). The 13 galaxies are listed in Table 6. All these galaxies have similar  $[12] - [25]$  colors and we, therefore, adopt our LRS average as a good representation for the spectrum of galaxies with  $[12] - [25] \approx 3.0$ .

TABLE 5  
IRAS COLORS OF FOUR TYPES OF GALAXY

SOURCE TYPE	[12] – [25]		[25] – [60]	
	Mean	$\sigma$	Mean	$\sigma$
Blue galaxies .....	2.02	0.28	4.27	0.14
Red galaxies .....	2.75	0.25	3.95	0.13
Seyfert galaxies .....	2.75	0.35	3.30	0.32
Quasars .....	2.34	0.44	2.64	0.49

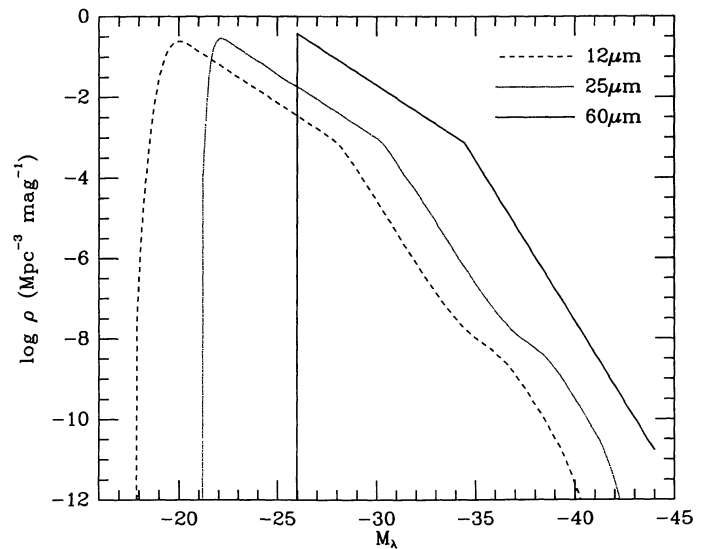


FIG. 5.—12, 25, and  $60\ \mu\text{m}$  luminosity functions for galaxies. The  $60\ \mu\text{m}$  double power-law luminosity function for galaxies of Soifer et al. (1987) is shown, along with the 12 and  $25\ \mu\text{m}$  luminosity functions for galaxies that we have derived using the breakdown into type shown in Fig. 4 and the colors shown in Table 5.

Ground-based 8–13  $\mu\text{m}$  spectra exist for  $\sim 60$  galaxies (see the recent review by Roche 1989), selected on the basis of 10  $\mu\text{m}$  brightness. Relatively few types of spectrum occur and, as for the LRS data base, spectra are available exclusively for galaxies that are both infrared-bright and physically peculiar (often Seyfert galaxies) because of the probable link between active galactic nuclei, optical emission lines, and the influence of nuclear activity on *IRAS* brightness. The starburst galaxies studied all have very similar spectra and reveal PAH emission; Seyfert galaxies tend to have featureless spectra or show what might be weak silicate absorptions (or possibly PAH emission again) and occasionally even weak silicate emission (Roche 1989). In spite of the absence of actual spectra, it is believed that normal galaxies should have spectra very similar to the composite we have created. In support of this belief, we note that the spatially integrated *IRAS* broad-band energy distribu-

TABLE 6  
GALAXIES WITH USABLE LRS SPECTRA

IRAS Name	Common Name
00450–2936 .....	NGC 253
02401–0013 .....	NGC 1068
03317–3618 .....	NGC 1365
03419+6756 .....	IC 342
05059–3734 .....	NGC 1808
06106+7822 .....	NGC 2146
09517+6954 .....	NGC 3034=M82
10257–4338 .....	NGC 3256
11257+5850 .....	NGC 3690/IC 694
13025–4911 .....	NGC 4945
13225–4245 .....	NGC 5128=Cen A
13341–2936 .....	NGC 5236
14092–6506 .....	in A1409–65



tion of M31 (Walterbos 1986) is consistent with that from individual dark clouds in our Galaxy as if we saw a “typical” interstellar medium in M31. From a distance, we see the interstellar media very clearly in external galaxies and PAH molecules are probably ubiquitous in these media too.

Consequently, we have chosen to represent our four types of galaxy by the same LRS composite but have linearly tilted this composite by appropriate amounts to match the observed mean [12] – [25] colors for the four categories of galaxy. We did this by extrapolating the LRS shape slightly shortward of 7.7  $\mu\text{m}$ , based on real astrophysical PAH spectra, and longward of 23  $\mu\text{m}$ , essentially by a power law, then convolved this spectrum with real *IRAS* filter profiles at 12 and 25  $\mu\text{m}$  to derive the color indices. The extrapolations were necessary to match the *IRAS* bandpasses as defined in the *IRAS* Explanatory Supplement.

### 3.3. Integration of Galaxies through Space

Having derived a luminosity function for the passband of interest, we then integrated this luminosity function along a ray through space. The resulting count/luminosity relation was subsequently scaled to the number of square degrees in the area of interest. Our integration through space includes cosmological effects, but no evolution. We assumed that  $H_0 = 75 \text{ km s}^{-1}$ ,  $\Lambda_0 = 0$  and  $\Omega_0 = 1$ , so  $q_0 = 0.5$ . The choice of cosmology only becomes important for  $[60] \gtrsim 10$ , [i.e.,  $F_\nu(60 \mu\text{m}) \lesssim 0.15 \text{ mJy}$ ]; the effects of evolution (Hacking, Condon, & Houck 1987) are likely to be much greater. We have chosen to ignore evolution because more work is required to confirm that any evolution is seen (as opposed to clustering) and to distinguish between the various evolutionary models proposed.

Below, we choose to use the symbol  $z = \Delta\lambda/\lambda_0$  to denote redshift, to distinguish it from  $z$  which we have used above for distance from the Galactic plane. The integration through space was performed using (see Chokshi & Wright 1988)

$$dN = n_0(1+z)^3 dV, \quad (19)$$

where

$$dV = s^2 \frac{c}{H_0} \times \frac{dz}{(1+z)\sqrt{1+2(q_0+1)z+(1+q_0+1.5\Omega_0)z^2+\Omega_0z^3}}, \quad (20)$$

and  $n_0$  is the number density in the rest frame,  $s = \vartheta r_A$  is the side of the cone over which the integration is being performed,  $\vartheta$  is the angular extent and  $r_A$ , the angular size distance, is

$$r_A = \frac{r_L}{(1+z)^2}, \quad (21)$$

where

$$r_L = \frac{cz}{H_0} \frac{2\sqrt{1+z}}{1+\sqrt{1+z}} \quad \text{for } \Omega_0 = 1; \quad (22)$$

$r_L$  is the luminosity distance. This integration was performed from  $z = 5 \times 10^{-6}$  ( $D = 20 \text{ kpc}$ ) to  $z = 5.0$ , with a multiplicative step size of  $dz = 0.001z$ .

In Figure 6, we compare model predictions with *IRAS* observations for several areas of the sky. We show areas near the Galactic poles in Figures 6a–6d, for which appropriate color criteria were used to select the galaxies from the PSC. The fits to the data are generally good, becoming somewhat worse at the shorter wavelengths; this is exactly what would be expected from consideration of the smaller detector size and the lower flux density of the galaxies at the shorter wavelengths. In Figure 6e we show a comparison with the bright galaxy sample of Soifer et al. (1988) from which the luminosity function was derived, and in Figure 6f, we show a comparison with the deep *IRAS* survey data from Hacking & Houck (1987). The deviation of the model from the data at the higher luminosities in some of the areas is due to local clustering. The north-south asymmetry mentioned above is also evident.

## 4. COMPARISON WITH OBSERVATIONS AND DISCUSSION

We now compare the results of the model with observations. There are five independent methods that will be discussed, the first four at 12 and 25  $\mu\text{m}$ , and the fifth at 2.2  $\mu\text{m}$ . These are: (1) the entire sky covered by the *IRAS* PSC; (2) the point sources extracted from the portion of the high-latitude sky ( $|b| > 50^\circ$ ) now available as part of the newly released *IRAS* Faint Source Survey, and extending to flux densities up to several times fainter than the PSC; (3) a high-latitude subset selected from the *IRAS* Serendipitous Survey and extending down to flux levels several times fainter than the PSC; (4) the deep *IRAS* survey from Hacking & Houck (1987); and (5) the 2  $\mu\text{m}$  source counts of Eaton et al. (1984) in the Galactic plane which cover a few small regions of the inner Galaxy. We also show that our model is consistent with star counts in the  $V$  passband at the north Galactic pole.

### 4.1. Comparison with the PSC

We have divided the sky into 238 zones, each containing of order 1000 *IRAS* “high-quality” 12  $\mu\text{m}$  sources, and have compared the 12 and 25  $\mu\text{m}$  source counts with the model in each of these zones. The zones involve a gridding into latitude bands as follows:  $-0.5^\circ < b < 0.5^\circ$ ;  $0.5^\circ \leq b < 2.0^\circ$ ;  $2^\circ \leq b < 5^\circ$ ;  $5^\circ \leq b < 10^\circ$ ;  $10^\circ \leq b < 20^\circ$ ;  $20^\circ \leq b < 40^\circ$ ;  $40^\circ \leq b \leq 90^\circ$  and a symmetric set like the latter six bands but for southern latitudes. Table 7 shows how we subdivided each of these latitude bands in longitude. Within each of these 238 zones, we ran the model on an evenly spaced  $5 \times 5$  grid in  $[l, b]$  of rays to overcome any density gradient that may be present across the

FIG. 6.—Comparison of model galaxy counts with *IRAS* data. The plots show the cumulative (log  $N$ , mag) relationship for galaxies in selected areas. The model predictions are shown as lines, with the 60  $\mu\text{m}$  prediction represented by the solid line, 25  $\mu\text{m}$  by the dotted line, and 12  $\mu\text{m}$  by the dashed line. The 60  $\mu\text{m}$  data are shown by plus signs, the 25  $\mu\text{m}$  data by crosses, and the 12  $\mu\text{m}$  data by the three pointed symbols. (a)  $b > 70^\circ$ . A correction to the area has been applied to compensate for the gap in *IRAS* coverage. (b) As for Fig. 6a, but for  $50^\circ < b < 70^\circ$ . (c) As for Fig. 6a, but for  $-70^\circ < b < -50^\circ$ . (d) As for Fig. 6a, but for  $b < -70^\circ$ . (e) The large flux limited sample of Soifer et al. (1987), at 60  $\mu\text{m}$ . (f) As for Fig. 6a, except that the data points come from the deep *IRAS* survey of Hacking & Houck (1987). The counts in each passband have been scaled to a common area of  $1.0 \text{ deg}^2$ . The “poor” quality fluxes measured by Hacking & Houck have been included in the data shown in this figure.

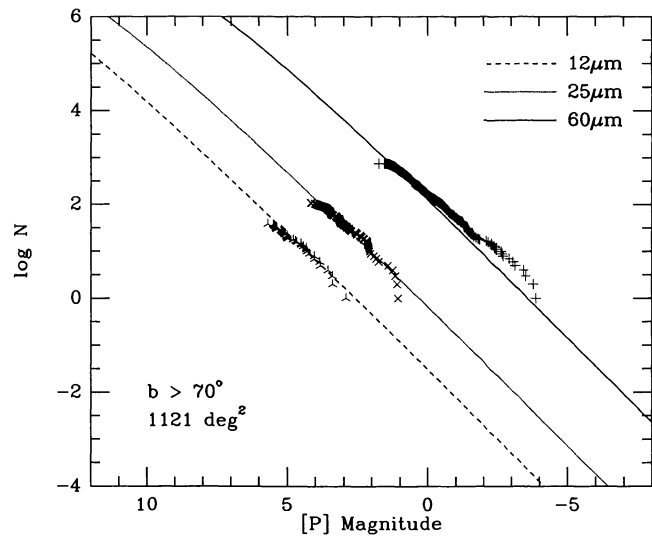


FIG. 6a

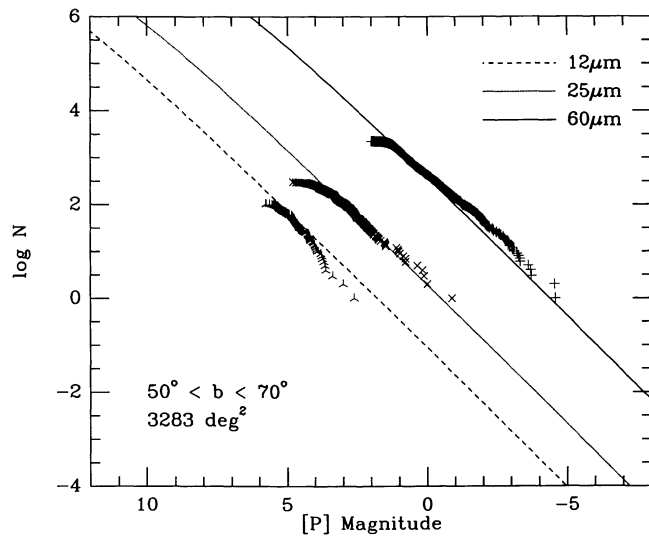


FIG. 6b

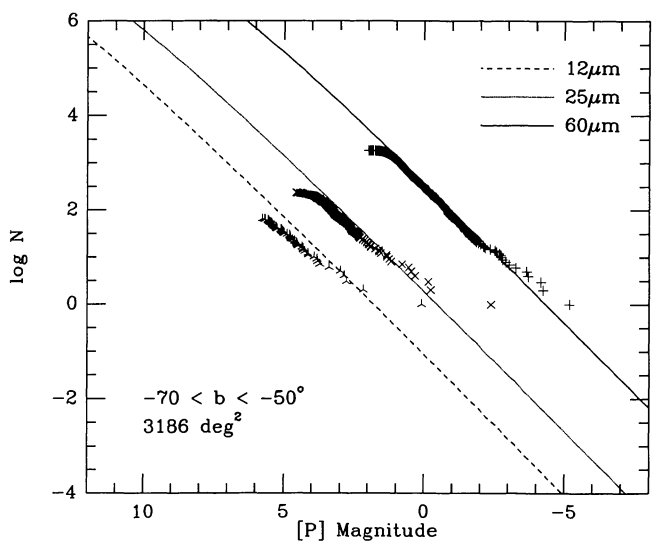


FIG. 6c

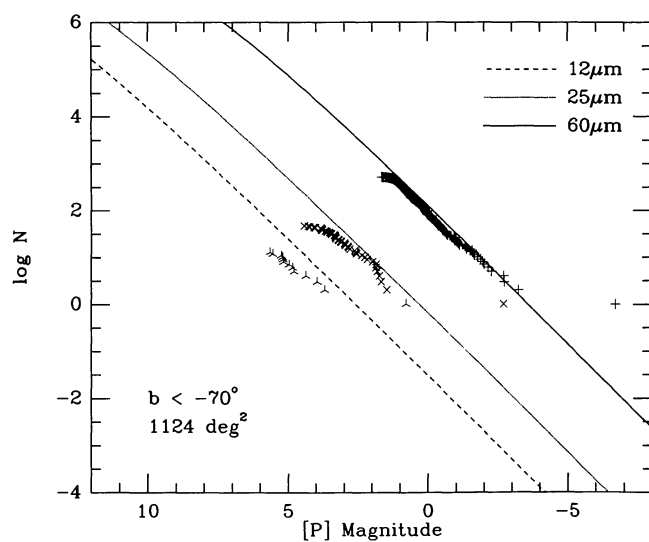


FIG. 6d

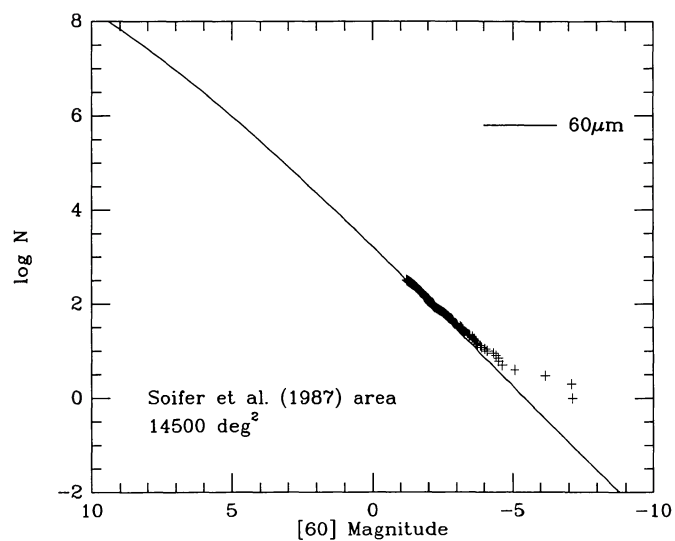


FIG. 6e

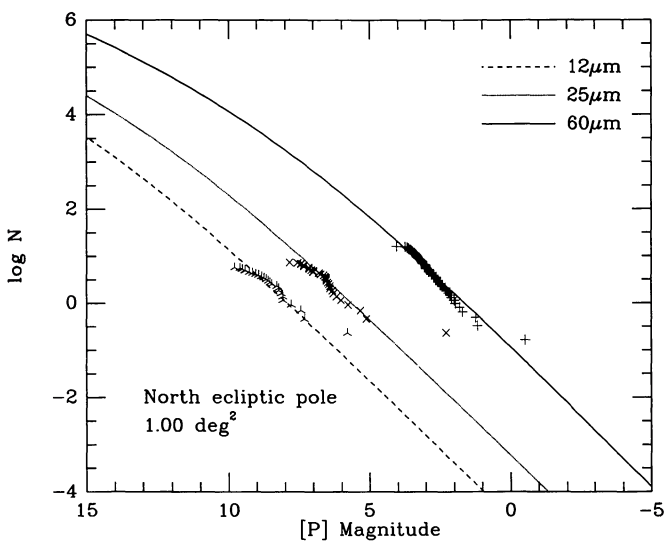


FIG. 6f

TABLE 7  
GRID OF AREAS OVER WHICH COMPARISONS OF THE MODEL WITH THE PSC DATA WERE MADE

<i>b</i> Limits		<i>l</i> Limits
40.0	90.0	0 45 90 135 180 225 270 315 360
20.0	40.0	0 45 90 135 180 225 270 315 360
10.0	20.0	-10 10 30 60 90 120 160 200 240 270 300 330 350
5.0	10.0	-5 5 15 25 35 45 55 65 75 85 100 115 135 160 200 225 245 260 275 285 295 305 315 325 335 345 355
2.0	5.0	-5 5 15 25 35 45 55 65 75 85 100 115 135 160 200 225 245 260 275 285 295 305 315 325 335 345 355
0.5	2.0	-5 5 15 25 35 45 55 65 75 85 100 115 135 160 200 225 245 260 275 285 295 305 315 325 335 345 355
-0.5	0.5	-5 5 15 25 35 45 55 65 75 85 100 115 135 160 200 225 245 260 275 285 295 305 315 325 335 345 355
-2.0	-0.5	-5 5 15 25 35 45 55 65 75 85 100 115 135 160 200 225 245 260 275 285 295 305 315 325 335 345 355
-5.0	-2.0	-5 5 15 25 35 45 55 65 75 85 100 115 135 160 200 225 245 260 275 285 295 305 315 325 335 345 355
-10.0	-5.0	-5 5 15 25 35 45 55 65 75 85 100 115 135 160 200 225 245 260 275 285 295 305 315 325 335 345 355
-20.0	-10.0	-10 10 30 60 90 120 160 200 240 270 300 330 350
-40.0	-20.0	0 45 90 135 180 225 270 315 360
-90.0	-40.0	0 45 90 135 180 225 270 315 360

zone. We further searched the whole sky for holes in *IRAS* PSC coverage and, for the 31 zones where holes were found, we measured the fractional area *A* of the hole in coverage. We then boosted the observed counts for that zone by the factor  $\frac{1}{1-A}$  (appropriate to the assumption of local uniform source density) before comparing the source counts with the model predictions. The match between model and data is excellent in many zones, and satisfactory in almost all zones except in circumstances to be described below. To give an impression of the quality of fits, and of the character and magnitude of discrepancies where these arise, we present a series of figures, showing both 12 and 25  $\mu\text{m}$  model predictions for several zones, overlaid by the cumulative (log number, log flux) source counts from the PSC.

Figures 7*a*–7*b* represent the innermost latitude band. This zone is chosen as an example that critically tests the absolute and relative contributions of three independent components, namely, the disk, the arms, and the molecular ring. It samples an area in which arms and ring are almost equal in their contributions, and each dominates the disk at the brighter magnitudes. The match is excellent at 12  $\mu\text{m}$  (Fig. 7*a*) from the *IRAS* limit near  $[12] = 4.0$  (this is quite bright due to *IRAS* problems with confusion arising from the high source density in this inner Galaxy region) to the effective bright limit of the PSC data ( $[12] \approx -1.5$ ). The corresponding predictions at 25  $\mu\text{m}$  (Fig. 7*b*) are also very good, almost from the faint to the bright limit. Only a handful ( $\sim 10$ ) of very bright objects are not represented by the model.

In Figures 7*c*–7*d* we show a less demanding region in the plane, further from the Galactic center, but one in which the “local arm” is important. This region is disk dominated at the lower fluxes but has a large contribution from the spiral arms at the higher fluxes. The model fit to the data is very good at both 12 and 25  $\mu\text{m}$ .

Figures 7*e*–7*f* essentially sample the bulge although, at the bright end, the bulge contribution is negligible and the disk, arms, and ring are almost equal in their contributions. The match is excellent at 25  $\mu\text{m}$ , and quite acceptable at 12  $\mu\text{m}$  although the PSC counts fall below the model over a 2 mag span at intermediate brightness. This is most likely due to our source tables not representing the bulge stars properly in this magnitude range. Our source tables do not include stars

unique to the bulge—rather we have tried to represent the bulge stars as best we can using the disk stars. Table 2 shows that the brightest bulge stars in our model have  $[25] \approx -13.6$  and  $[12] - [25] \approx 1.3$ . This 25  $\mu\text{m}$  limiting absolute magnitude is realistic, but the color of these stars is not—the bulge stars are metal-rich compared with the disk stars, so a bulge star of a particular mass can attain a larger  $[12] - [25]$  color than can an otherwise similar disk star. Therefore, when these stars are included at 12  $\mu\text{m}$  they are too bright, thus explaining the surplus in the model prediction. Our source table does include stars with  $[12] - [25] > 1.3$ , but these (disk) stars are higher mass so it is inappropriate to include them for the bulge. It is important to note that in this zone the source density is very high. In any zone in which high source density processing of the PSC was applied (near the Galactic center and close to the Galactic plane in the inner Galaxy), it is unclear to what extent this confusion processing has been able to approximate reality. Therefore, in such regions, the *IRAS* source counts may not be a very accurate representation of the true source counts. Consequently, an effect such as the roll-off of the source counts relative to the model prediction such as that seen in Figure 7*e* for  $[12] > 3$  may be more representative of incompleteness in the *IRAS* source counts than of some specific inadequacy in the model.

Our representation of the spiral arms as a symmetric, four-armed, homogeneous structure, everywhere coplanar with the disk must clearly be simplistic. Substantial departures of the arms from the mean Galactic plane are well established from the neutral hydrogen distribution. To test whether the model is indeed limited by its representation of the arms we offer the regions whose 12  $\mu\text{m}$  source counts are shown in Figure 7*g*–7*h*, for  $55^\circ \leq l < 65^\circ$ , and  $2^\circ \leq |b| < 5^\circ$ . The 12  $\mu\text{m}$  model predictions are disk dominated but one can clearly recognize that the arms’ contribution must be much larger in reality than our model would suggest at northern latitudes, but this is conspicuously not the case at southern. This north-south asymmetry is surely a direct consequence of the way in which the neutral hydrogen in the outer spiral arm in this direction lies high above the Galactic plane (see Weaver 1974; his Fig. 11). There is a large amount of gas lying between 0.5 and 1.0 kpc above the plane between longitudes  $50^\circ$  and  $90^\circ$  in northern latitudes that is not matched by any corresponding feature to the south. Gas and stars must be well mixed in this region so



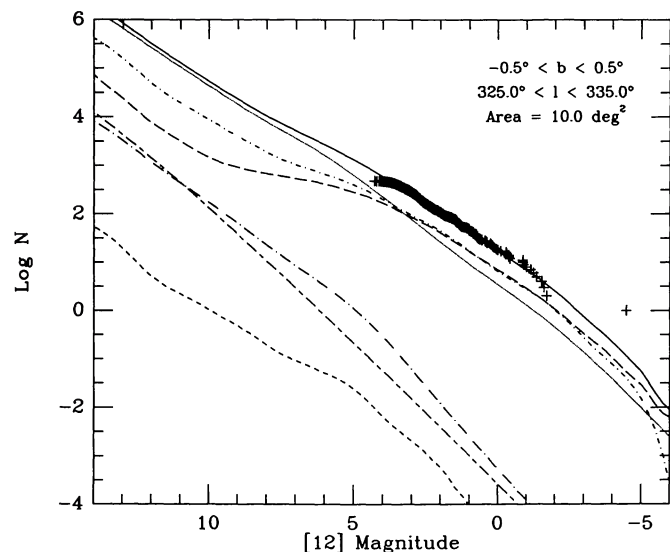


FIG. 7a

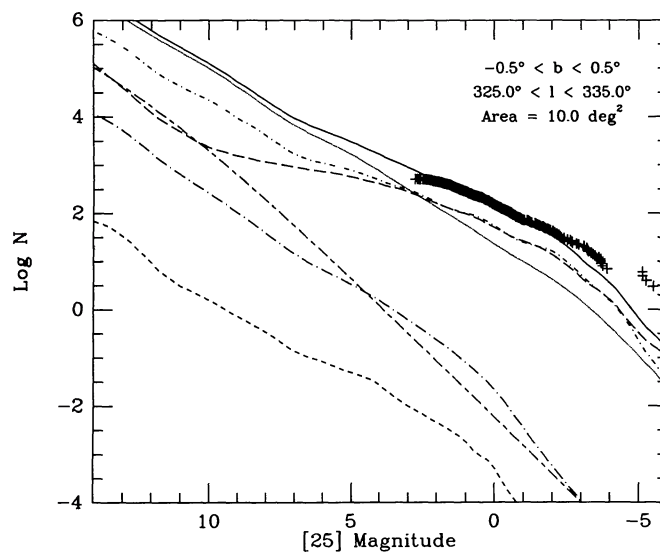


FIG. 7b

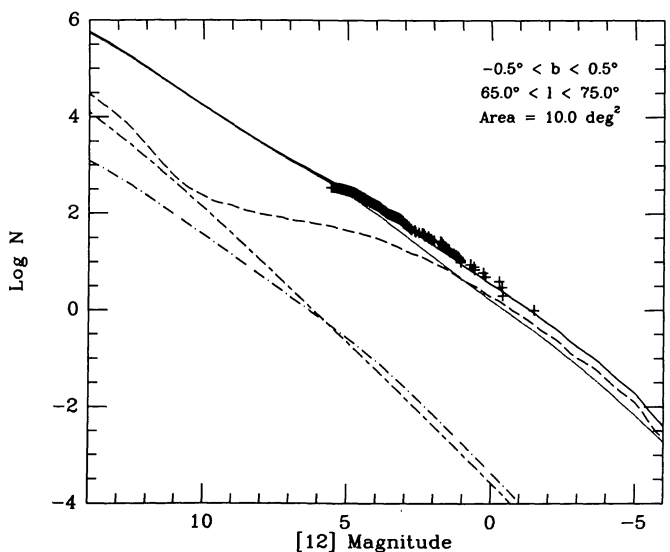


FIG. 7c

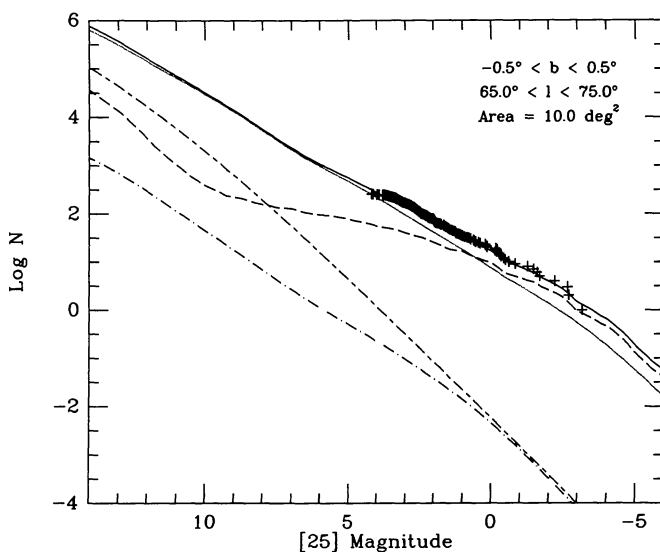


FIG. 7d

FIG. 7.—Comparison of model predictions with *IRAS* PSC data. (a) The plot shows the cumulative ( $\log N$ , mag) relationship for the *IRAS* 12  $\mu\text{m}$  bandpass, for the region  $-0.5^\circ < b < 0.5^\circ$ ,  $325.0^\circ < l < 335.0^\circ$ . The solid line shows the total counts predicted, the dotted line shows the contribution from the exponential disk, the long-dashed line shows the spiral arms, the short-dashed-dotted line shows the molecular ring, the short-dashed line shows the bulge, the long-dashed-dotted line shows the stellar halo, and the long-dashed-short dashed line shows the contribution from external galaxies. The plus signs are the data points. (b) As for (a), but for 25  $\mu\text{m}$ . (c) As for (a), but for the region  $-0.5^\circ < b < 0.5^\circ$ ,  $65.0^\circ < l < 75.0^\circ$ . (d) As for (c), but for 25  $\mu\text{m}$ . (e) As for (a), but for the region  $-5^\circ < b < -2^\circ$ ,  $-5^\circ < l < 5^\circ$ , specially chosen to emphasize the bulge. (f) As for (e), but for 25  $\mu\text{m}$ . (g) As for (a), but for the region  $2^\circ < b < 5^\circ$ ,  $55^\circ < l < 65^\circ$ . (h) As for (a), but for the region  $-5^\circ < b < -2^\circ$ ,  $55^\circ < l < 65^\circ$ . (i) As for (a), but for the region  $0.5^\circ < b < 2^\circ$ ,  $245^\circ < l < 260^\circ$ . (j) As for (a), but for the region  $-2^\circ < b < -0.5^\circ$ ,  $245^\circ < l < 260^\circ$ . (k) As for (a), but for the region  $-40^\circ < b < -20^\circ$ ,  $225^\circ < l < 270^\circ$ . (l) As for (k) but for 25  $\mu\text{m}$ .

that our model, which treats the young stars that must have formed from this displaced gas, fails to mimic the non-coplanar character of the spiral arms in this region.

That we are susceptible to inhomogeneities in the real Galaxy is obvious, and their effects can be seen in Figures 7i–7j where we compare north and south zones for  $0.5 \leq |b| < 2^\circ$  and  $245^\circ \leq l < 260^\circ$  at 12  $\mu\text{m}$ . The model matches the PSC data well over most of the southern zone (note that when departures from the model prediction occur, at the bright end, these represent the influence of only a small number of

sources). However, in the corresponding northern zone, the PSC data are deficient compared with what we expect from both disk and arms. An explanation for this north-south asymmetry can be gleaned from an examination of both the neutral hydrogen (Weaver 1974, his Fig. 1) and the CO (Dame et al. 1987) in this direction. The arms lose their integrity here, and even the disk is poorly represented in the gas distribution, leading to a model prediction in excess of the PSC source counts.

As a final example of a specific comparison zone, Figures 7k–7l show an intermediate latitude zone, heavily dominated

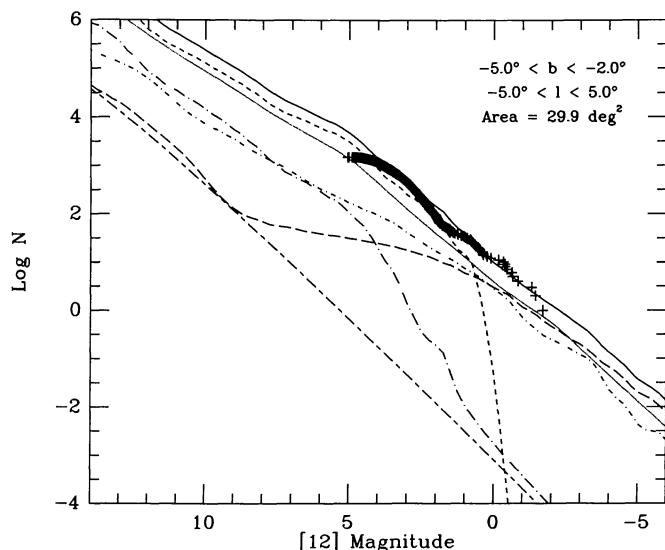


FIG. 7e

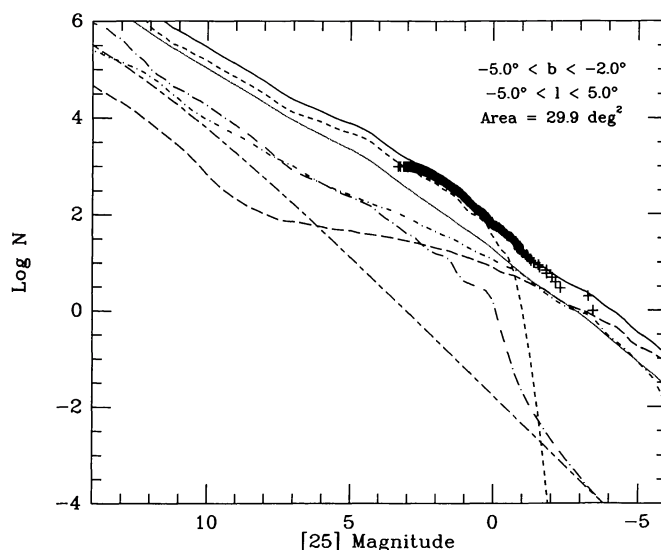


FIG. 7f

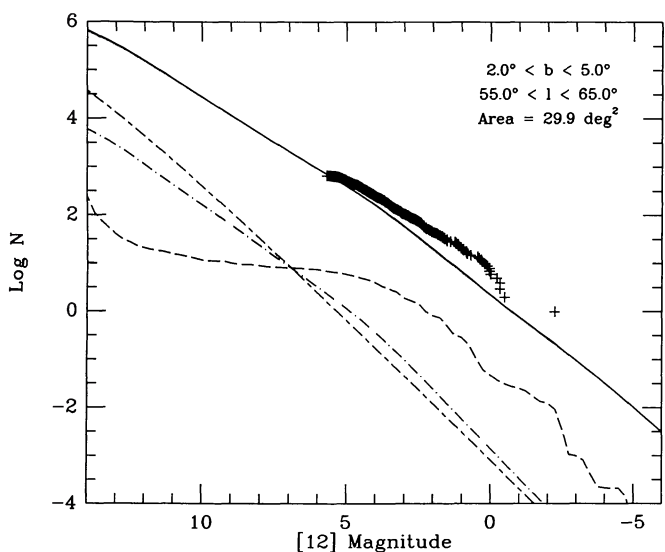


FIG. 7g

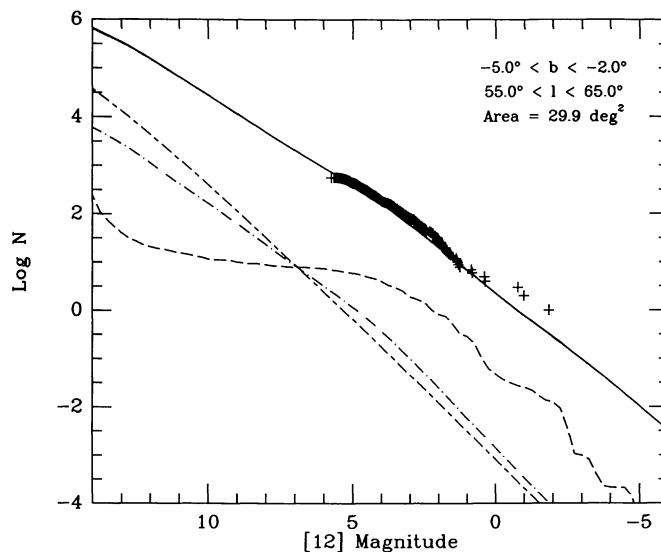


FIG. 7h

by the disk. The match is excellent at both wavelengths, over the whole the range of the PSC data until the *IRAS* counts begin to roll-off through incompleteness at the faintest flux levels.

Figure 8 provides a synoptic view of the quality of the model by displaying the degree to which the predictions match the PSC data for all the 238 zones, and at both wavelengths. In Figures 8a–8b we show the whole sky in an Aitoff projection and in Figures 8c–8d we show the Galactic plane region ( $|b| < 10^\circ$ ) magnified. We distinguish those zones in which the model falls below the data by a factor of 2 or more (no model zone fails by more than a factor of 3), and by a factor of 1.5–2. In essentially every other zone in which the model prediction is below the observations, the model prediction lies within 20% of the PSC source counts. Also shown are those zones in which the observations fall below the model predic-

tions by a factor of 1.3 or more. There can be several reasons for this latter type of discrepancy: (1) PSC confusion processing has still underrepresented the real sky; (2) the spiral arms depart from our homogeneous and simple geometrical representation; and (3) there are truly warps in the Galactic plane itself. All the zones around the Galactic center in which the model lies above the data fall in zones where high source density processing was used to create the PSC. Consequently, we cannot determine, for example, whether we should alter our representation of the Galactic bulge or perhaps include the northerly displacement ( $\sim 12$  pc; see, e.g., Volk et al. 1992) of the Sun from the Galactic plane to account for discrepancies in the central regions. Cause 2 was discussed above in connection with non-coplanar arms and disk, and cause 3 is likewise established from neutral hydrogen studies; indeed, systematic warps in the Galactic plane of up to several hundred pc are common

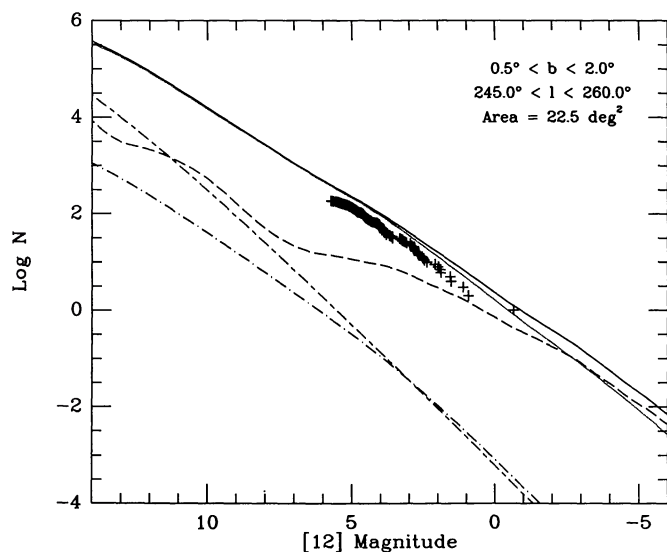


FIG. 7i

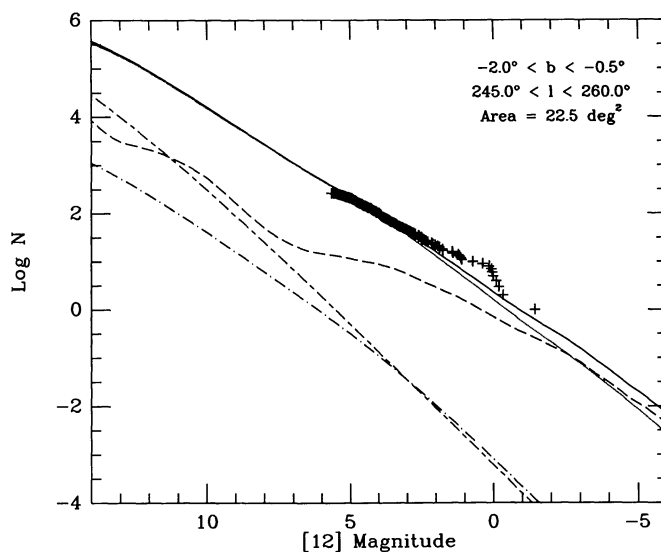


FIG. 7j

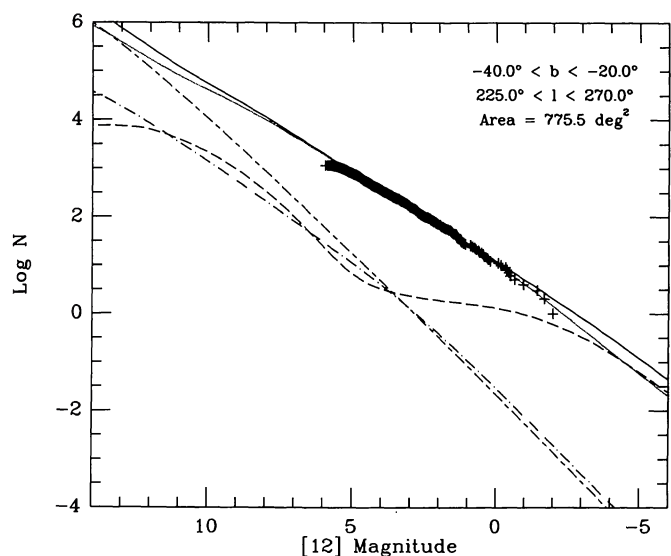


FIG. 7k

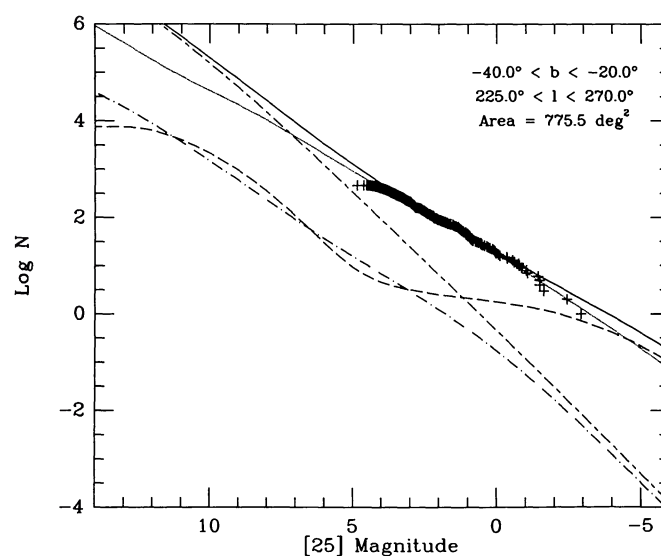


FIG. 7l

(see, e.g., Kerr & Westerhout 1965, their Fig. 11). We note that the worst discrepancies in Figure 8 are close to the latitudinal peaks found by Djorgovski & Sosin (1989) which these authors attribute to a warp of the stellar disk.

Local effects are also apparent in these figures. All the discrepancies at 25  $\mu$ m that occur for latitudes  $|b| > 10^\circ$  are attributable to the Taurus and Orion molecular clouds, and the Large Magellanic Cloud. In spite of these caveats, we note that (1) apart from Orion, Taurus, and the LMC, *every zone with  $|b| > 10^\circ$  is well represented by our model, at both 12 and 25  $\mu$ m*; (2) within the  $|b| < 10^\circ$  band, there are 182 zones—at 25  $\mu$ m we find only 17 where the model falls below the PSC counts by more than a factor of 2, and 37 where the shortfall is between 1.5 and 2—at 12  $\mu$ m the corresponding numbers are only 6 and 23, respectively. Many of these poor matches correspond to regions of active star formation in which gross inho-

mogeneities from our idealized Galaxy occur (e.g., Cygnus, Carina). However, we conclude that, insofar as the PSC represents the broad-band 12 and 25  $\mu$ m sky, the model is quite satisfactory.

#### 4.2. Comparison with the Faint Source Survey

The *IRAS* Faint Source Survey (Moshir et al. 1989, hereafter FSS) represents the result of co-addition of the various passes that *IRAS* made across the sky, resulting in the ability to recognize point sources fainter than those in the PSC. We have compared our model with the area  $|b| > 50^\circ$  which was released on tape in 1989. The number of independent passes across the sky can readily attain six to eight, yielding, in principle, a gain of a factor of 2–3 in sensitivity. It is clearly important to test our model against the deeper results of the FSS,



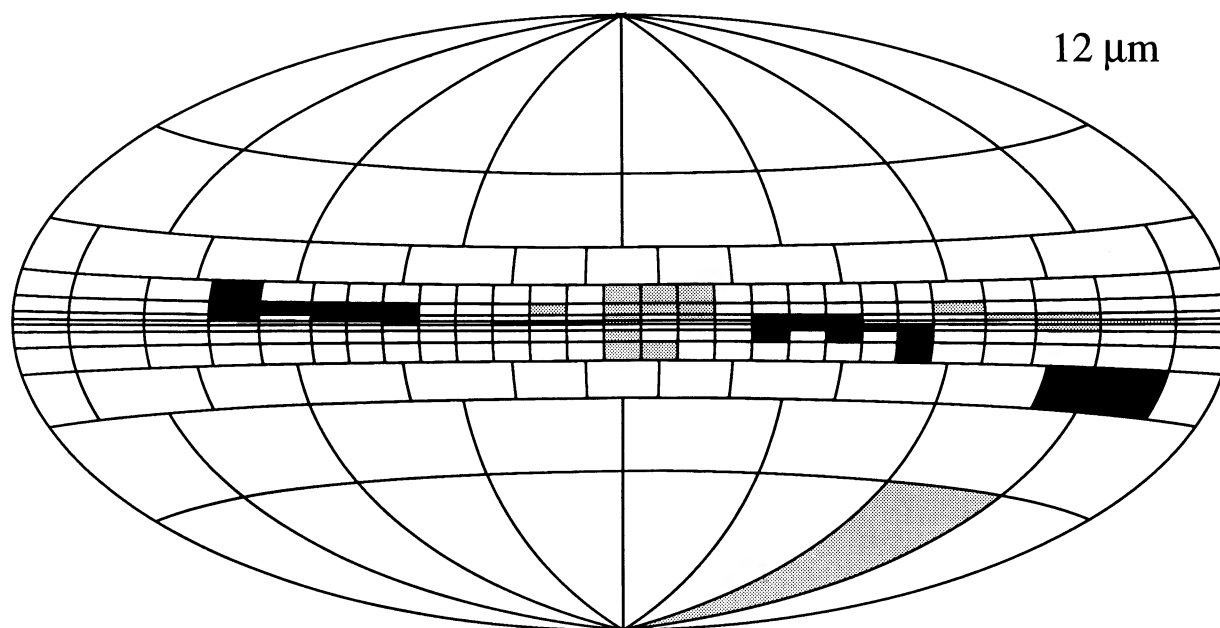


FIG. 8a

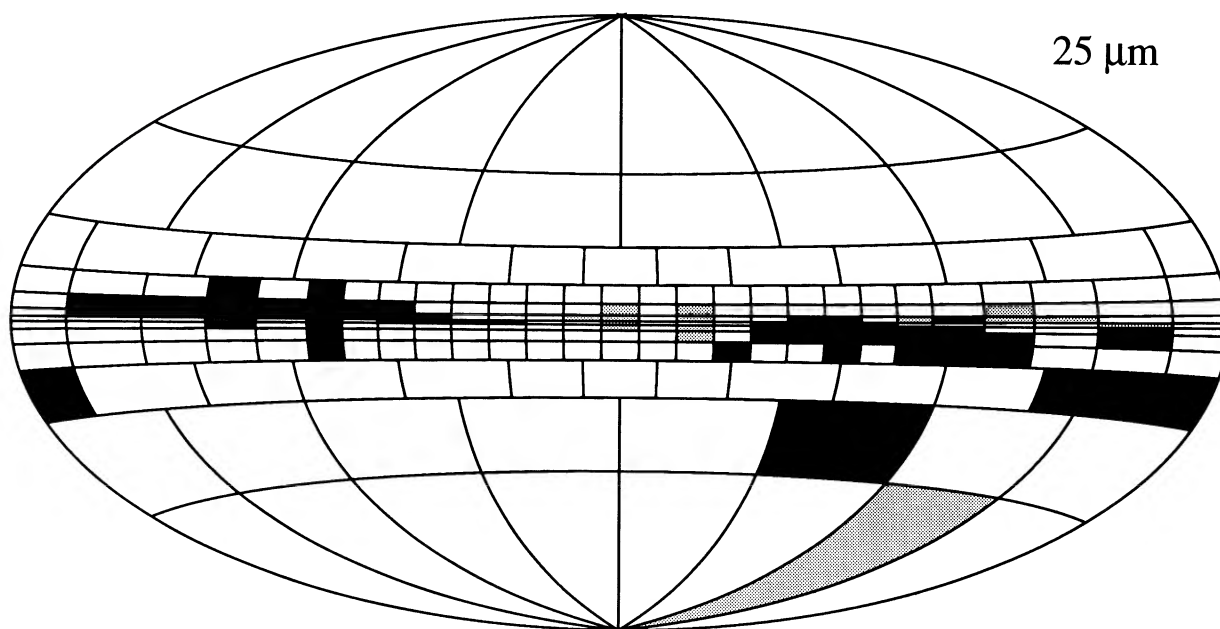


FIG. 8b

FIG. 8.—All-sky comparison of model predictions with the PSC. The Aitoff projection shows the 238 regions for which we compared model prediction with the *IRAS* PSC source counts, using cumulative ( $\log N$ , mag) plots of the type shown in Fig. 7. Galactic coordinates were used for the projection, with the Galactic center at the center, and Galactic longitude increasing to the left. The light shading indicates regions in which the model prediction exceeds the observed *IRAS* counts by a factor of 1.3 or more over a significant range of magnitude (i.e., not at the high brightness end where number counts are not statistically significant, and not near the lower brightness limit where incompleteness in the *IRAS* data becomes important). The dark shading indicates regions in which the *IRAS* counts exceed the model prediction over a significant magnitude range by a factor of 1.5–2. The black shading indicates regions in which the *IRAS* counts exceed the model prediction over a significant magnitude range by a factor of 2 or more. (a) 12  $\mu\text{m}$ . (b) 25  $\mu\text{m}$ . (c) A magnified view of the region  $|b| < 10^\circ$ , at 12  $\mu\text{m}$ . (d) A magnified view of the region  $|b| < 10^\circ$ , at 25  $\mu\text{m}$ .

even if only the high-latitude (disk-dominated sky) can be checked. However, there is one major problem with the FSS that militates against generally achieving a true factor of 2–3 gain in sensitivity in these source counts over the PSC, namely, the fact that not all of the high-latitude sky is covered to a

uniform sensitivity (see FSS, their Figs. III.C.5 and III.C.6). Nevertheless, we have made comparisons with the FSS in 18 separate zones, at each wavelength, broken down as follows: the north and south Galactic caps ( $0 \leq l < 360$ ;  $b > 70^\circ$ ,  $b < -70^\circ$ ); for  $50^\circ < b \leq 70^\circ$ , every  $45^\circ$  in longitude around the

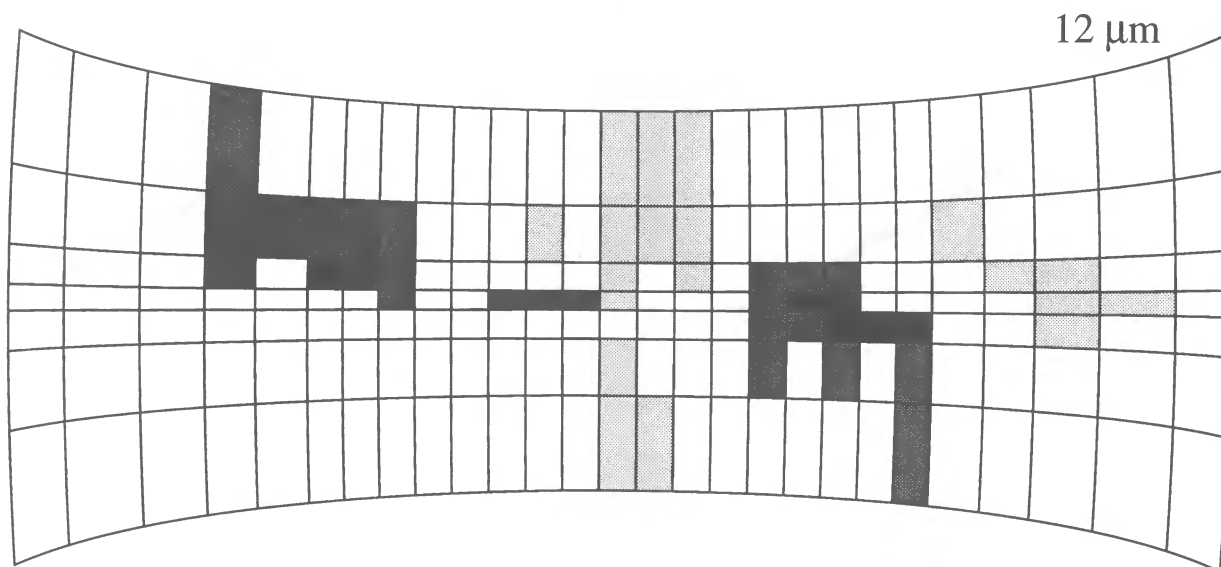


FIG. 8c

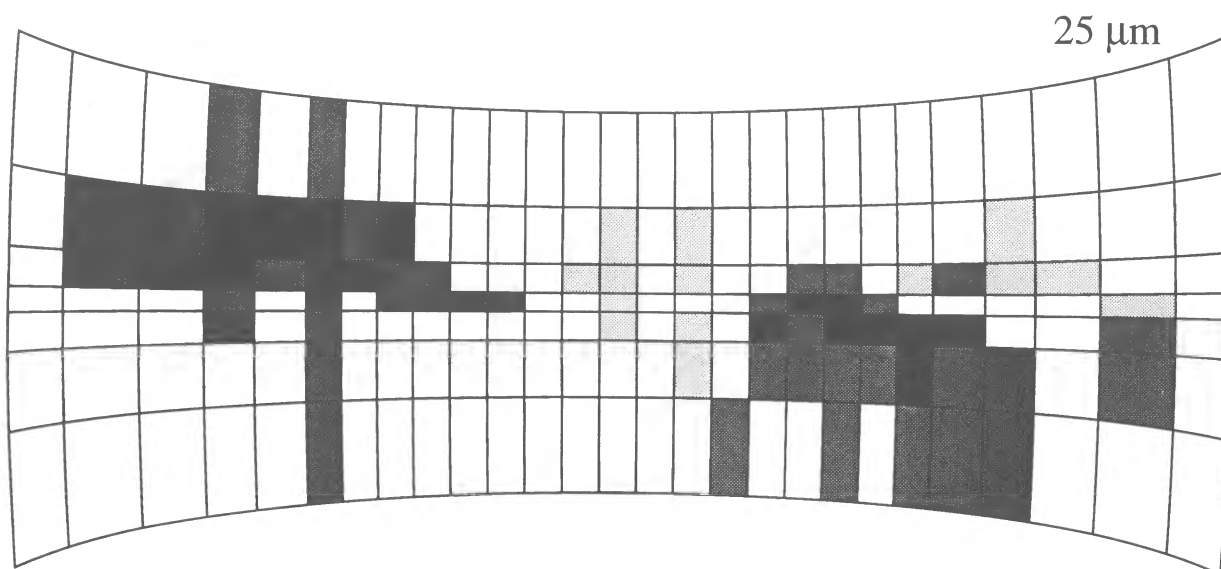


FIG. 8d

sky starting with the zone  $0^\circ \leq l < 45^\circ$ , and similarly for  $-70^\circ \leq b < -50^\circ$ .

In Figures 9a-9b we present both 12 and 25  $\mu\text{m}$  comparisons between the model and the FSS for an area of the sky in which the FSS coverage is most complete (see FSS, Figs. III.C.5 and 6). The 12  $\mu\text{m}$  match is highly satisfactory (again, discrepancies arise only from a handful of bright sources), and that at 25  $\mu\text{m}$  quite satisfactory (deviating only at the bright end, where the source counts are very small). The faint end of the FSS data shows excellent slope and level agreement with the model's prediction, all the way until the FSS data turn over through incompleteness ( $[12] \approx 5.8$ , or  $S_{12} \approx 180$  mJy;  $[25] \approx 4.2$ , or  $S_{25} \approx 200$  mJy). We note that our estimates of roll-off in the FSS data, based on comparison with the model,

are in very good agreement with those given in the FSS Explanatory Supplement (Moshir et al. 1989) for the selected zone, namely, 90% complete above 180 mJy at 12  $\mu\text{m}$ , and above 210 mJy at 25  $\mu\text{m}$ . Of further interest in Figure 9b is the fact that the FSS counts at 25  $\mu\text{m}$  appear slightly above the model's prediction for the disk alone (between magnitudes 3 and 4.5, above the roll-off). According to the model, it is the extragalactic component at 25  $\mu\text{m}$  that elevates the predicted source count above that from the disk in this direction. It is tantalizing to note that were a survey to be undertaken from space at this wavelength, with a flux threshold for completeness only 1 mag below the FSS, one could critically assess the importance of the extragalactic component.

We show one more pair of comparisons with the FSS that is

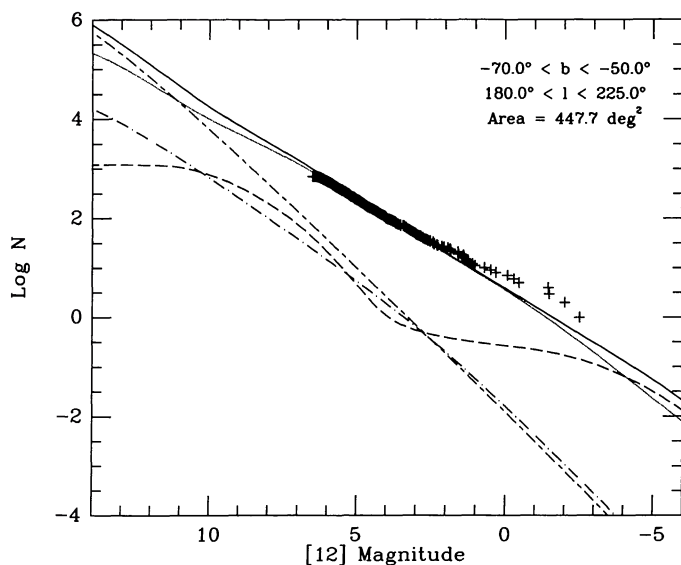


FIG. 9a

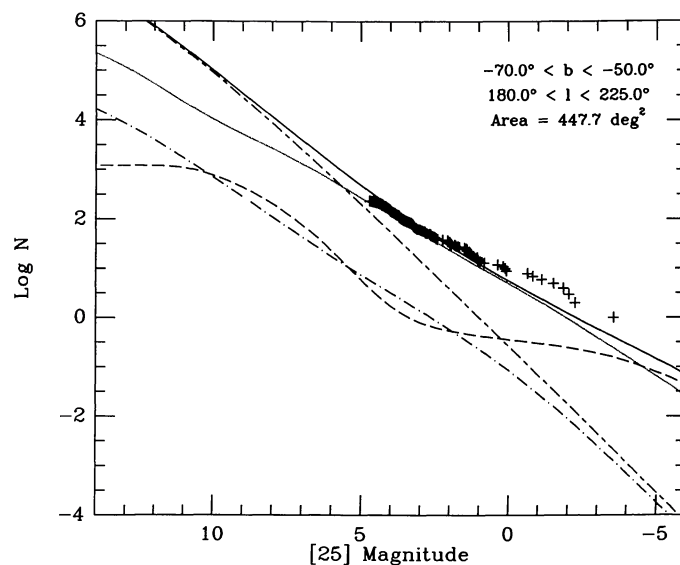


FIG. 9b

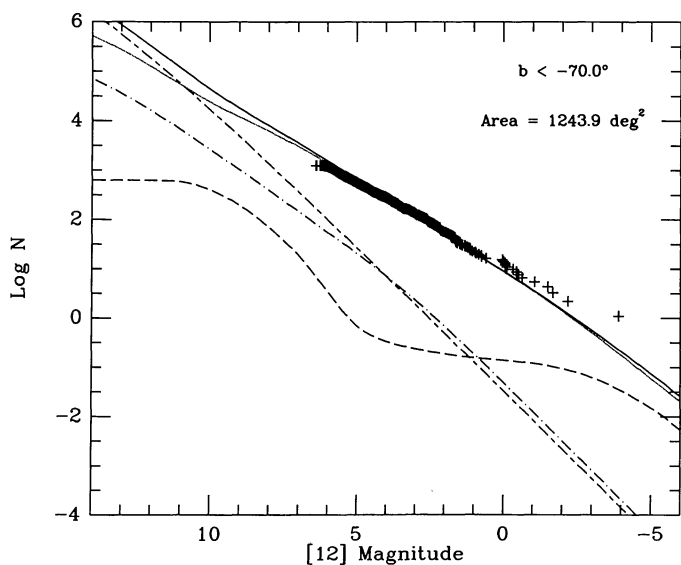


FIG. 9c

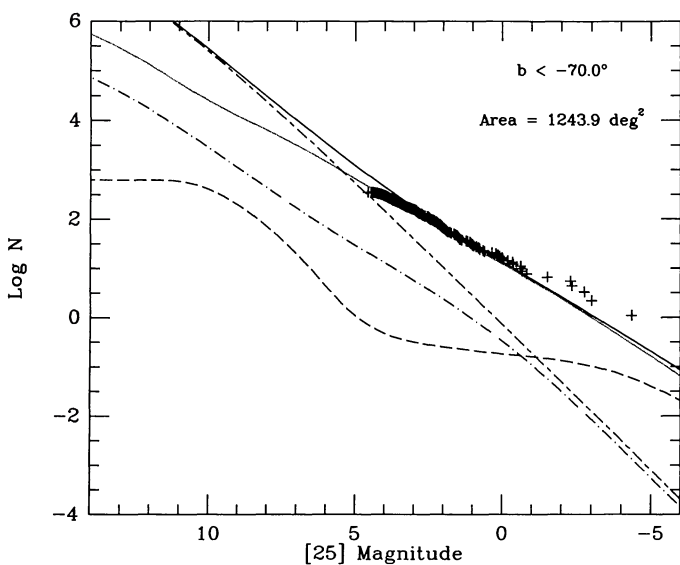


FIG. 9d

FIG. 9.—Comparison of model predictions with *IRAS* FSS data. Cumulative ( $\log N$ , mag) plots are shown, with the same line coding as in Fig. 7. (a) The region  $-70^\circ < b < -50^\circ$ ,  $180^\circ < l < 225^\circ$ , at  $12\ \mu\text{m}$ . (b) As for (a) but at  $25\ \mu\text{m}$ . (c) The region  $b < -70^\circ$ , at  $12\ \mu\text{m}$ . Source counts were boosted by a factor of 1.10 to compensate for a hole in the *IRAS* sky coverage in this area. (d) As for (c) but at  $25\ \mu\text{m}$ .

representative of the other zones in which we have tested the model but whose FSS coverage is far less complete than that portrayed in Figures 9a–9b. Figures 9c–9d select the south Galactic polar cap, only  $\sim 20\%$  of whose area has good completeness in the FSS deep coverage, while most is covered only to flux levels brighter than those described above. The body of FSS data match the model well. However, at both wavelengths one readily sees the gradual departure of the FSS source counts from the model's predictions. A distinct break and change of slope near  $[12] = 5.0$  and  $[25] = 3.5$  is apparent, beyond which the FSS data lie increasingly far from the model's predictions. The magnitudes at these breaks represent the completeness limits in the PSC (see Figs. 7k–7l). The slope changes and

steady drooping of the FSS source counts surely indicate the fact that the completeness threshold of the FSS is variable across the zone.

We conclude that, while the FSS is not, in general, an ideal product for challenging the model further than the PSC, careful choice of regions of the sky best-sampled by the FSS do lead to excellent agreement between reality and our model, at flux levels appreciably below the completeness limits of the PSC.

#### 4.3. Comparison with the Serendipitous Survey

The *IRAS* Serendipitous Survey Catalog (Kleinmann et al. 1986, hereafter SSC) is culled from the abundant pointed ob-



servations made by *IRAS* during which small portions of the sky were scanned slowly and repeatedly, yielding substantially fainter flux density limits than attained in the PSC. Indeed, it is estimated that the 90% completeness limits for the SSC are 120 mJy at 12  $\mu$ m ( $[12] \approx 6.3$ ) and 150 mJy at 25  $\mu$ m ( $[25] \approx 4.5$ ) (SSC, p. IV-11). One particularly valuable aspect of the SSC was the creation of a high-latitude subset of its point sources. The criteria for inclusion in this subset were (1)  $|b| > 30^\circ$ ; (2) each pointed observation should correspond to a field containing fewer than 20 60  $\mu$ m sources per square degree. Removal of sources detected more than once in overlapping zones and these criteria sufficed to exclude the LMC and general effects of confusion. Recent application of these same criteria with almost identical software for eliminating sources in overlapping grids yields a data base containing 1158 12  $\mu$ m sources and 561 25  $\mu$ m sources, and kindly supplied to us electronically by R. Cutri (1989, private communication). The effective area of this high-latitude subset is 259.33 square degrees.

In Figure 10 we compare the differential source counts from this subset of the SSC with two typical model predictions that essentially bracket the range of model predictions for total source counts in the rather uniform high-latitude sky. When one makes allowance for the dominantly intermediate and bright targets of these pointed observations, it is clear that there is excellent agreement between the model and the SSC at 12  $\mu$ m, while the 25  $\mu$ m comparison is adequate.

A comparison with the SSC at lower Galactic latitude would suffer from confusion problems, so we have not attempted such a comparison here.

#### 4.4. Comparison with the Deep *IRAS* Survey

The deep *IRAS* survey area at  $l = 97^\circ$ ,  $b = 30^\circ$  (Hacking & Houck 1987), contains the deepest observations obtained by *IRAS*. It was produced by repeated scans by *IRAS* over an area

of 4–6  $\text{deg}^2$  at the north ecliptic pole, and reaching to a depth of up to 100 times fainter than the PSC at 12 and 25  $\mu$ m. Like the FSS, some parts of the field were observed more often than others, so the completeness limit varies across the field.

In Figure 6 we showed that there was a good fit between the predicted and observed galaxy counts in each of the 12, 25, and 60  $\mu$ m passbands in the deep survey area. In Figure 11a we show a comparison between the model predicted source counts at 12  $\mu$ m and the observed source counts. The figure shows only Galactic sources—extragalactic sources were suppressed from the observed counts on the basis of color (as was the planetary nebula NGC 6543) leaving a total of 41 stars in this field; extragalactic sources were also suppressed from the model prediction. The model fits the data very well and suggests that virtually all of the stars in this region are disk stars. The source counts appear to roll-off below  $[12] \approx 7$ . This probably represents the completeness limit of the data in this field.

In Figure 11b we compare the 36 high-quality 25  $\mu$ m sources (excluding NGC 6543) with the model prediction. The fit is again satisfactory, although it is less clear where the rolloff occurs in the 25  $\mu$ m counts. The counts are certainly incomplete below  $[25] \approx 6.5$ . The model suggests that disk stars and extragalactic sources should make an equal contribution to the total source counts at a flux limit of  $S_{25} = 11$  mJy.

The SSC objects, along with the deep *IRAS* survey, currently provide the deepest 12 and 25  $\mu$ m comparison fields for the model, and we, therefore, regard the basic structure and details of our model as vindicated.

#### 4.5. Comparison with 2.2 Micron Source Counts

Eaton et al. (1984) provide deep near-infrared source counts for seven small fields along the Galactic plane in the inner Galaxy. We have compared our model with these, although

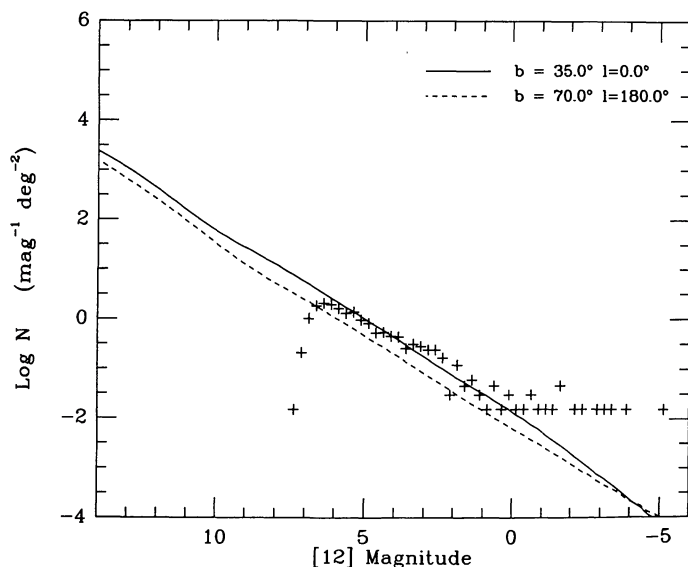


FIG. 10a

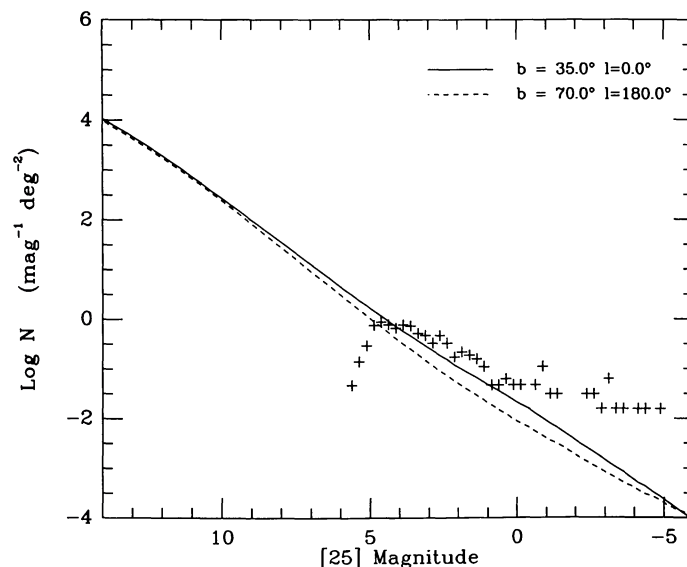


FIG. 10b

FIG. 10.—Comparison of model predictions with *IRAS* SSC data. Differential (log  $N$ , mag) plots are shown, with two representative model predictions. The solid line shows the total model prediction for  $b = 35^\circ$ ,  $l = 0^\circ$ , and the dashed line shows the total model prediction for  $b = 70^\circ$ ,  $l = 180^\circ$ . The differential source counts were calculated for intervals of 0.25 mag. (a) 12  $\mu$ m. (b) 25  $\mu$ m.

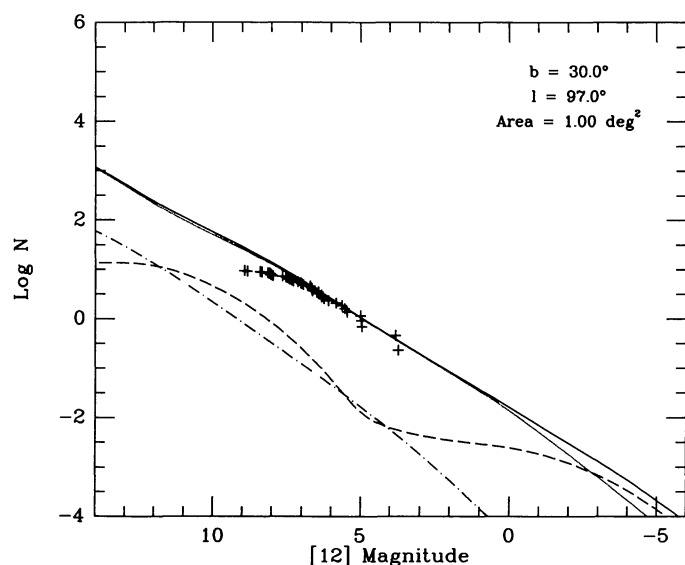


FIG. 11a

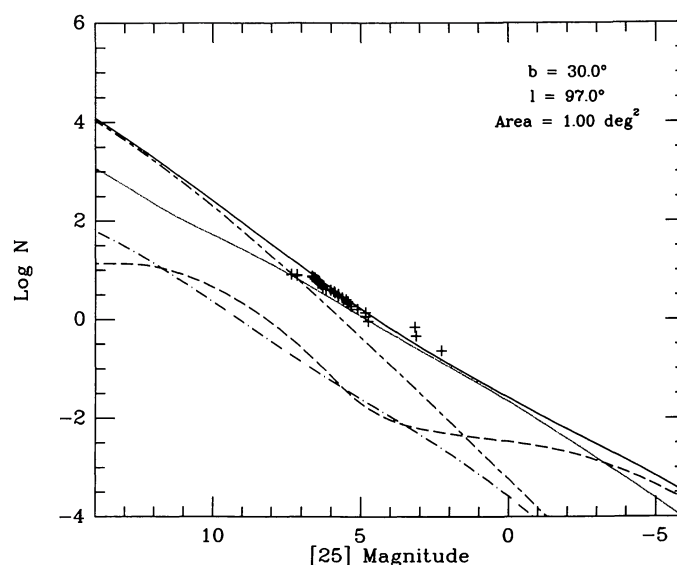


FIG. 11b

FIG. 11.—Comparison of model predictions with the deep *IRAS* survey data. Cumulative ( $\log N$ , mag) plots are shown, with the same line coding as in Fig. 7. The source counts have been scaled to an area of  $1.00 \text{ deg}^2$ . (a) Galactic sources only at  $12 \mu\text{m}$ . Extragalactic sources have been suppressed from both the observations and model prediction. (b) All sources at  $25 \mu\text{m}$ .

the model was not originally intended to operate with precision at such short wavelengths. Figure 12 compares Eaton et al.'s data with the model for their field near  $l = 40^\circ$ ,  $b = 0^\circ$ . The comparison is highly satisfactory. The six other fields observed by these authors also show good matches to our model predictions in the *K* band, with the exception of the  $l = 30^\circ$ ,  $b = 0^\circ$  zone, where the observations exceed the model by a factor of  $\sim 1.7$ . However, we note that many factors militate against a good comparison in this zone. First, we have represented the

molecular ring by a circular structure, coplanar with the disk, yet it may resemble an oval, tilted with respect to the Galactic plane, and with major axis not aligned with the  $l = 0^\circ$  direction. The molecular ring's contribution in this direction is significant and our oversimplified geometry may cause problems at  $2 \mu\text{m}$ . Second, it is currently impossible to distinguish between an enhanced stellar density and a diminished stellar extinction at *K* in this zone (or anywhere); either would produce a source count above the model's prediction. Further, one does

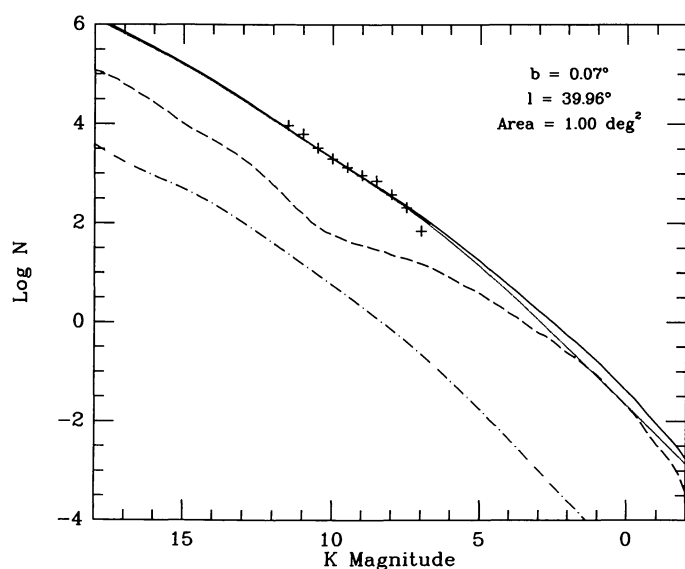


FIG. 12.—Comparison of model predictions with *K* star counts. The model predictions are shown using the same line coding as used in Fig. 7. The model prediction for the position  $b = 0^\circ 07'$ ,  $l = 39^\circ 96'$  is compared to the star counts of Eaton et al. (1984) at this position. The star counts and model predictions have been scaled to an area of  $1.00 \text{ deg}^2$ .

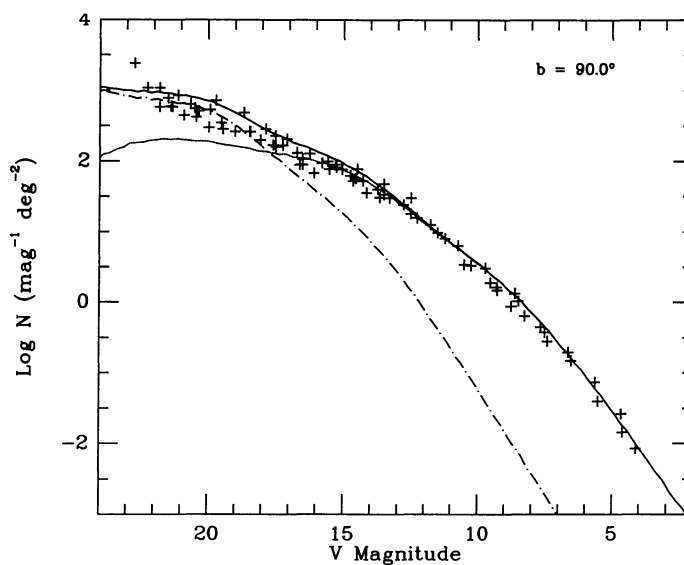


FIG. 13.—Comparison of model predictions with *V* star counts at the north Galactic pole. The model predictions are shown using the same line coding as used in Fig. 7. Star count data are shown as plus signs and are taken from Bahcall & Soneira (1984).

not expect the extinction to be as simply characterizable and as uniform as is the representation in our model.

We also compared the model prediction with the 2.2  $\mu\text{m}$  star counts at the north Galactic pole (NGP) of Elias (1978b), and found good agreement.

We conclude that the model does extremely well even at 2.2  $\mu\text{m}$  in spite of its fundamental purpose, namely to represent the point source sky at much longer wavelengths.

#### 4.6. Comparison with *V* Star Counts at the North Galactic Pole

Figure 13 shows a comparison of the model prediction with the *V* star count data assembled by Bahcall & Soneira (1984). The agreement is satisfactory, with the model prediction falling close to the standard (original) Bahcall & Soneira model. Figure 13 can be directly compared with Figure 21 of Bahcall & Soneira, which also includes the prediction of their model incorporating the globular cluster feature. The globular cluster feature is discussed by Bahcall et al. (1985); it is not explicitly included in the halo luminosity function used in our model.

#### 5. CONCLUSIONS

We have constructed a detailed model of the infrared point source sky. This model can operate using any arbitrary filter lying in the LRS wavelength range (7.7–22.7  $\mu\text{m}$ ), as well as with a selection of broad-band filters. We represent the Galactic sources by means of a large source table rather than by a luminosity function. The model includes the extragalactic sky at the mid-infrared wavelengths. The model predicts cumulative or differential source counts for a range of magnitudes (or fluxes).

Five Galactic components are necessary: the exponential disk, the bulge, the spiral arms, the molecular ring, and the stellar halo. The halo is the least important component of the Galaxy at mid-infrared wavelengths. We have represented each of these components with as much physical realism as possible, by deriving as many of their parameters as possible from independent studies at other wavelengths.

Superficially one could argue that the model offers a vast number of degrees of freedom through the 87 categories of source in its sky, the five geometrical Galactic components, and the many colors and distributional parameters for each of

TABLE 8  
PREDICTED DIFFERENTIAL SOURCE COUNTS IN SELECTED DIRECTIONS<sup>a,b</sup>

A. 2.2 MICRONS					
<i>K</i>	Galactic Sources Only				
	1	2	3	4	5
< 00 .....	-2.32	-2.08	-1.81	-1.37	-1.36
00-01 .....	-2.10	-1.80	-1.50	-1.05	-0.91
01-02 .....	-1.72	-1.39	-1.03	-0.60	-0.31
02-03 .....	-1.34	-1.01	-0.58	-0.13	0.27
03-04 .....	-0.96	-0.64	-0.17	0.33	0.83
04-05 .....	-0.59	-0.26	0.22	0.79	1.31
05-06 .....	-0.22	0.12	0.59	1.21	1.74
06-07 .....	0.10	0.50	0.97	1.59	2.13
07-08 .....	0.39	0.86	1.36	1.96	2.48
08-09 .....	0.65	1.17	1.74	2.33	2.83
09-10 .....	0.97	1.44	2.10	2.72	3.20
10-11 .....	1.34	1.70	2.40	3.13	3.58
11-12 .....	1.71	2.03	2.67	3.53	3.98
12-13 .....	2.02	2.40	2.92	3.89	4.40
13-14 .....	2.26	2.74	3.24	4.21	4.79
14-15 .....	2.41	3.01	3.60	4.44	5.13

B. 12 MICRONS										
[12]	Galactic Sources Only					All Sources				
	1	2	3	4	5	1	2	3	4	5
< 00 .....	-2.15	-1.78	-1.28	-0.49	0.37	-2.15	-1.78	-1.28	-0.49	0.37
00-01 .....	-2.03	-1.66	-1.17	-0.35	0.54	-2.02	-1.66	-1.17	-0.35	0.54
01-02 .....	-1.66	-1.31	-0.80	-0.01	0.96	-1.65	-1.31	-0.80	-0.01	0.96
02-03 .....	-1.28	-0.95	-0.43	0.36	1.28	-1.27	-0.94	-0.43	0.36	1.28
03-04 .....	-0.90	-0.57	-0.08	0.71	1.62	-0.89	-0.56	-0.08	0.71	1.62
04-05 .....	-0.54	-0.20	0.28	1.07	1.95	-0.52	-0.19	0.28	1.07	1.95
05-06 .....	-0.19	0.18	0.66	1.35	2.19	-0.15	0.19	0.66	1.35	2.19
06-07 .....	0.13	0.54	1.04	1.69	2.44	0.20	0.57	1.05	1.69	2.44
07-08 .....	0.42	0.89	1.42	2.08	2.75	0.53	0.93	1.43	2.08	2.75
08-09 .....	0.70	1.20	1.79	2.48	3.12	0.90	1.27	1.81	2.49	3.12
09-10 .....	1.03	1.47	2.13	2.88	3.50	1.31	1.59	2.16	2.88	3.50
10-11 .....	1.42	1.77	2.44	3.28	3.90	1.77	1.96	2.49	3.29	3.90
11-12 .....	1.80	2.12	2.70	3.66	4.31	2.21	2.36	2.78	3.67	4.31
12-13 .....	2.10	2.49	2.97	4.01	4.74	2.63	2.78	3.09	4.02	4.74
13-14 .....	2.32	2.82	3.32	4.29	5.10	3.01	3.17	3.46	4.30	5.11
14-15 .....	2.46	3.08	3.70	4.50	5.41	3.38	3.52	3.85	4.53	5.42

C. 25 MICRONS										
[25]	Galactic Sources Only					All Sources				
	1	2	3	4	5	1	2	3	4	5
< 00 .....	-2.01	-1.58	-0.99	0.06	1.29	-1.98	-1.57	-0.99	0.06	1.29
00-01 .....	-1.93	-1.53	-0.97	0.08	1.29	-1.88	-1.51	-0.97	0.08	1.29
01-02 .....	-1.58	-1.21	-0.62	0.32	1.44	-1.49	-1.16	-0.61	0.32	1.44
02-03 .....	-1.23	-0.87	-0.30	0.65	1.81	-1.09	-0.80	-0.28	0.65	1.81
03-04 .....	-0.87	-0.52	0.02	0.95	1.97	-0.66	-0.41	0.06	0.95	1.97
04-05 .....	-0.52	-0.16	0.36	1.22	2.24	-0.21	0.00	0.42	1.23	2.24
05-06 .....	-0.17	0.20	0.72	1.54	2.41	0.26	0.44	0.80	1.55	2.41
06-07 .....	0.15	0.56	1.08	1.94	2.68	0.74	0.89	1.20	1.96	2.69
07-08 .....	0.43	0.91	1.44	2.37	3.16	1.21	1.34	1.62	2.40	3.16
08-09 .....	0.72	1.21	1.81	2.75	3.58	1.70	1.78	2.04	2.79	3.59
09-10 .....	1.05	1.48	2.15	3.07	3.96	2.17	2.22	2.44	3.12	3.96
10-11 .....	1.45	1.78	2.45	3.40	4.26	2.63	2.66	2.83	3.46	4.27
11-12 .....	1.82	2.14	2.72	3.74	4.60	3.05	3.08	3.20	3.81	4.61
12-13 .....	2.12	2.51	3.00	4.06	5.00	3.45	3.48	3.57	4.15	5.01
13-14 .....	2.34	2.85	3.35	4.30	5.30	3.82	3.85	3.94	4.42	5.32
14-15 .....	2.48	3.10	3.73	4.53	5.55	4.17	4.20	4.30	4.68	5.56

<sup>a</sup> Log<sub>10</sub> sources per deg<sup>2</sup> in the indicated magnitude range for each of five fields.

<sup>b</sup> 1: *b* = 90°; 2: *b* = 30°, *l* = 90°; 3: *b* = 10°, *l* = 90°; 4: *b* = 0°, *l* = 90°; 5: *b* = 0°, *l* = 330°.



the 87 categories. However, this is an extreme point of view because the existence of each “free” parameter is astrophysically justified, and most are already constrained by a wealth of observations in different spectral regimes. We specifically make no claims for the uniqueness of this model: we can assert only that the number of parameters it incorporates are sufficient for the quality of match to the real sky that is achieved; we do not know if all are strictly necessary.

The model produces a good fit for nearly all areas for the sky located at  $|b| > 5^\circ$ . The model gives deficient predictions in some zones of the Galactic plane. We attribute these deficiencies to local structure, inhomogeneity, and other possible inadequacies in our representation of the spiral arms.

To provide some practical information for the design of future infrared survey experiments, we tabulate in Table 8 the model’s predictions for differential source counts (summed over all components), in five directions: the Galactic poles; an intermediate latitude ( $b = 30^\circ$ ,  $l = 90^\circ$ ); a low-latitude ( $b = 10^\circ$ ,  $l = 90^\circ$ ); and two locations within the Galactic plane ( $b =$

$0^\circ$ ,  $l = 90^\circ$ ;  $b = 30^\circ$ ,  $l = 330^\circ$ ). These tables incorporate predictions to 15th magnitude at  $K$ , [12], and [25]. The 12 and  $25\ \mu\text{m}$  source counts are dominated by extragalactic sources at the higher latitudes. We have therefore included predictions for Galactic sources alone for these passbands.

Many people contributed vital support, valuable discussions, information, or encouragement during the 3 yr spanned by this study. In particular, we thank David Goorvitch, Gary Villere, Russell Walker, Harold Weaver, Alex Ruelas, Roc Cutri, and Tom Chester. We are especially grateful to the referee, Stephan Price, for his critical reading of this paper and for his substantive recommendations. This effort was supported by NASA Ames Research Center through contract NAS2-12515 with Jamieson Science & Engineering, Inc., and cooperative agreement NCC 2-407 with the SETI Institute. M.C. also thanks NASA Ames Research Center for partial support under cooperative agreement NCC 2-142 with UC Berkeley.

## APPENDIX A MODELING THE ASYMPTOTIC GIANT BRANCH STARS

Many of the stars observed by *IRAS* are asymptotic giant branch (AGB) stars: carbon stars and most of the stars with silicate dust features, which represent at least 50% of the bright  $12\ \mu\text{m}$  sources observed by *IRAS* based upon the features seen in the LRS spectra (also see Walker & Cohen 1988). These stars represent the final stage of evolution of stars of intermediate main sequence mass (from  $\sim 1.25\ M_\odot$  up to  $\sim 8.0\ M_\odot$ ). Such stars are relatively uncommon compared to main-sequence stars and have reliable distances in only a small number of cases, particularly for carbon stars. Further, the types of AGB stars that are easily detected by *IRAS* are generally not easily observable at optical wavelengths. Carbon stars with thick dust shells, such as IRC +10° 216, and their oxygen-rich counterparts, such as the OH/IR stars, have either very faint optical counterparts or no optical counterpart at all, but are extremely bright in the infrared and can be observed by *IRAS* anywhere in the Galaxy.

Under these circumstances, the absolute properties of AGB stars cannot be observationally determined, so we have attempted to derive the space densities and absolute magnitudes for these stars from a model of the overall AGB evolution. A number of assumptions which are poorly constrained by the observations must be made in the model. In this Appendix, we describe this model and discuss the assumptions that were used to derive the properties of AGB stars observed by *IRAS*.

### A1. PARAMETERS FROM STELLAR EVOLUTION MODELS

Models of AGB stellar evolution are available for a wide range of main-sequence masses, but there are indications that these models are not yet good enough to be matched with observations. There is a long-standing problem in producing AGB models for carbon stars, the “carbon star mystery,” because the models uniformly predict that all carbon stars should be massive and luminous while the observations indicate that most carbon stars are of low mass. This problem with the AGB stellar models is a serious drawback in understanding general AGB evolution. Also, few of the AGB evolution models allow for mass loss, which is observed to be an important property of most of these stars. Recent models have included mass loss using the Reimers (1977) formula, but generally such models need to invoke a “superwind” late in the evolution to adjust the final stellar mass to the desired value (see Weidemann & Koester 1983). This is an undesirable characteristic because we know of no physical mechanism to produce a superwind. Thus, while the stellar evolution models serve as a guide to the AGB evolution, at this time they should not be overemphasized.

There are some useful results from the AGB evolution models. The model results of Boothroyd & Sackmann (1988a–d) were used as prototypes, because these models are for low masses ( $1.2$  and  $3\ M_\odot$ ), from which the bulk of carbon stars are probably derived, and because mass loss was included in the models. One well-established result of all the AGB stellar models is that, to a good approximation, the stellar luminosity is determined by the mass of the stellar core, which is almost completely de-coupled from the envelope. Boothroyd & Sackmann (1988b) give approximations to the stellar luminosity,  $L_*$ , as a function of the core mass,  $M_c$ , in the form

$$L_* = L_0(M_c - M_0)L_\odot, \quad (\text{A1})$$

where  $L_0$  and  $M_0$  are constants for various ranges of  $M_c$ . The actual luminosity is predicted to deviate from the values from the equation due to interactions within the stellar core, which produce helium shell flashes at intervals during the evolution. We assumed that the stellar luminosity was always given by equation (A1) with the constants from Boothroyd & Sackmann.

The models are also important in setting the initial AGB core mass as a function of the main-sequence mass. For low-mass stars we used the results from Boothroyd & Sackmann (1988c) while for the highest mass AGB stars we used results from the review by Iben & Renzini (1983). Combined with equation (A1), these determine the AGB luminosity evolution. The initial AGB core mass was assumed to be linear between the 1.2 and 3.0  $M_{\odot}$  values from Boothroyd & Sackmann and a quadratic between 3.0 and 8.0  $M_{\odot}$ . The initial core mass for an 8  $M_{\odot}$  star was taken to be 1.075  $M_{\odot}$ . There is some mass loss before the stars reach the AGB; for the low-mass stars, the values from Boothroyd & Sackmann were used and, for the more massive stars, the previous mass loss was assumed to be negligible.

Stellar models also give a relation between stellar mass, luminosity, and effective temperature (Wood & Cahn 1977),

$$\log_{10}(T_{*}) = [101.35 - 2.5 \log_{10}(L_{*}/L_{\odot}) + 0.533 M_{*}/M_{\odot}]/26.423, \quad (\text{A2})$$

whence the stellar radius,  $R_{*}$ , can be calculated assuming that the star is a blackbody.

The other major constraint on the AGB models is the value of the minimum supernova progenitor mass, normally denoted as  $M_{\text{up}}$ . This determines the upper mass limit for the AGB. The value of  $M_{\text{up}}$  is not well determined but is generally thought to be between 5 and 8  $M_{\odot}$ . We used  $M_{\text{up}} = 8 M_{\odot}$ , from Weidemann & Koester (1983).

#### A2. THE MASS-LOSS FORMULA

At present there is no satisfactory theory for the cause and the magnitude of stellar mass loss in AGB stars. The mass loss is critical in determining the AGB lifetime as a function of mass and is the most important factor for *IRAS* observations. We are forced to use empirical results because there is no basic theory predicting the mass-loss rate. The most widely used parameterization of the mass-loss rate is the Reimers formula

$$\dot{M} = 4 \times 10^{-13} \eta (L_{*}/L_{\odot}) (R_{*}/R_{\odot}) / (M_{*}/M_{\odot}) M_{\odot} \text{ yr}^{-1}, \quad (\text{A3})$$

where the constant  $\eta$  is usually presumed to be in the range  $\frac{1}{3} \lesssim \eta \lesssim 3$ . On the basis of studies of globular cluster stars, the value for Population II red giants must be near the lower limit of  $\frac{1}{3}$  (see the references given by Iben & Renzini 1983). We assume that  $\eta$  is a function of the stellar mass and that only low-mass stars need  $\eta$  of order 0.4.

Observational determination of mass-loss rates is notoriously difficult and absolute luminosities are also difficult to determine for stars with high mass-loss rates; therefore, the  $\dot{M}$  values in the literature cannot determine  $\eta$ . The strongest observational constraint on  $\eta$  is the “initial-final mass relation” (Weidemann & Koester 1983; Weidemann 1984) which tells us how soon the star must lose its envelope and leave the AGB. The observations indicate that the final mass changes only slightly for main-sequence masses between  $\sim 1.25 M_{\odot}$  and  $\sim 3 M_{\odot}$ . A star of main-sequence mass  $M_{\text{up}}$  must leave the AGB by the time the core mass reaches 1.41  $M_{\odot}$ , or possibly sooner depending upon conditions for core stability.

For our assumed initial AGB core mass we found that  $\eta = 3.0$  is required to make  $M_{\text{up}} = 8 M_{\odot}$ . We assumed that for a 1.2  $M_{\odot}$  star,  $\eta \approx 0.4$  as determined from the globular cluster stars. At intermediate mass,  $\eta$  was assumed to be a quadratic function of the initial

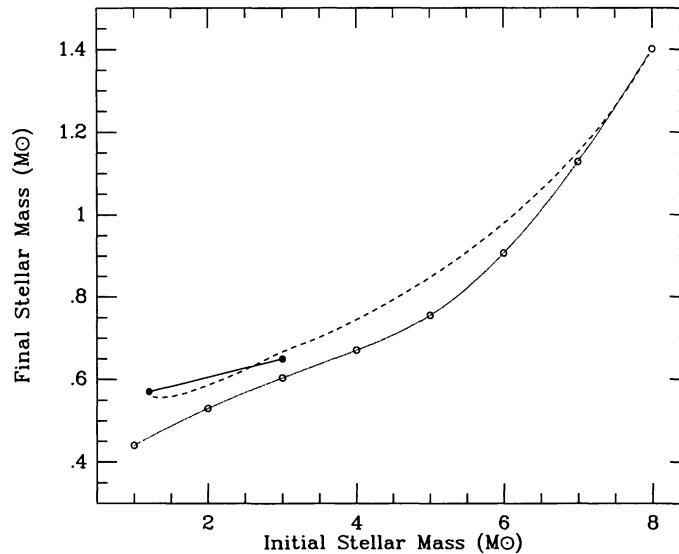


FIG. 14.—The initial-final mass relation predicted from the AGB models (*dashed curve*) compared with the observational values of Weidemann (1984) for 1.2 and 3.0  $M_{\odot}$  from masses of central stars of planetary nebulae (*filled circles*) and the values of Weidemann & Koester (1983) from white dwarf masses (*open circles*). To produce the very flat final mass curve the mass-loss efficiency must be increased for stars of initial masses near 3.0  $M_{\odot}$  as in eq. (A4).

mass. A linear relation was first tried, but it was unable to reproduce the initial-final mass relation. After a series of trials we adopted a formula for  $\eta$ :

$$\eta(M_{\text{ms}}) = -0.059 + 0.382M_{\text{ms}} + 0.288(M_{\text{ms}} - 1.20 M_{\odot})(8.0 M_{\odot} - M_{\text{ms}}). \quad (\text{A4})$$

This formula has the linear term and a quadratic term that boosts the mass-loss rate for stars of  $\sim 3 M_{\odot}$  main-sequence mass. We varied the amplitude of the quadratic term until a reasonable initial-final mass relation was obtained.

The initial-final mass relation predicted from the models using these  $\eta$  values is shown in Figure 14. From 1.25 to  $3.0 M_{\odot}$  the models match the observed values from planetary nebulae central star masses (Weidemann 1984) reasonably well. The relation from white dwarf mass determinations (Weidemann & Koester 1983) is similar in form to the model curve but has somewhat lower final masses. In our models it is not possible to match the Weidemann & Koester values because the model initial AGB mass from Boothroyd & Sackmann (1988c) for a  $1.2 M_{\odot}$  star is less than the corresponding Weidemann & Koester final AGB mass.

### A3. OTHER OBSERVATIONAL CONSTRAINTS

There are other observations which must be considered in creating an AGB model. Generally it is estimated that there are 10% as many carbon stars as oxygen-rich AGB stars, while abundance studies of planetary nebulae indicate that  $\geq 50\%$  of planetary nebulae are carbon rich and thus presumably had carbon star progenitors (Zuckerman & Aller 1986). If there is no change in AGB lifetime when a star becomes a carbon star, this implies that, on average, a star which becomes a carbon star spends 20% of its AGB lifetime as a carbon star.

The *IRAS* observations of carbon stars are also important to the model, as a test of the mass-loss rates for carbon stars. For comparison with the models, we used all optically identified carbon stars (Stephenson 1973) with *IRAS* observations at 12, 25, and  $60 \mu\text{m}$  and all the *IRAS* objects with classes 40–49 LRS spectra, excluding sources which appeared to be misclassified silicate feature sources. This resulted in a sample of 825 *IRAS* sources for comparison with the models.

The color-color distribution of the carbon stars is unusual compared to the silicate feature sources because there are many optically identified carbon stars with  $60 \mu\text{m}$  excesses (see Fig. 15). Willems (1987) and Chan & Kwok (1988) interpret this as the result of an interruption of the stellar mass loss when the star becomes carbon rich. However, as discussed by Claussen et al. (1987), this scenario for carbon star evolution does not produce the proper number of optically visible carbon stars if the mass loss is only interrupted once, because the remnant shell disperses quickly compared to the estimated mean lifetime of carbon stars. In our models we used the concept of interrupted mass loss, which gives a good fit to the colors of many carbon stars (see Chan & Kwok 1988), but assumed that mass loss was interrupted several times during the life of a carbon star, in addition to when the star first becomes carbon rich.

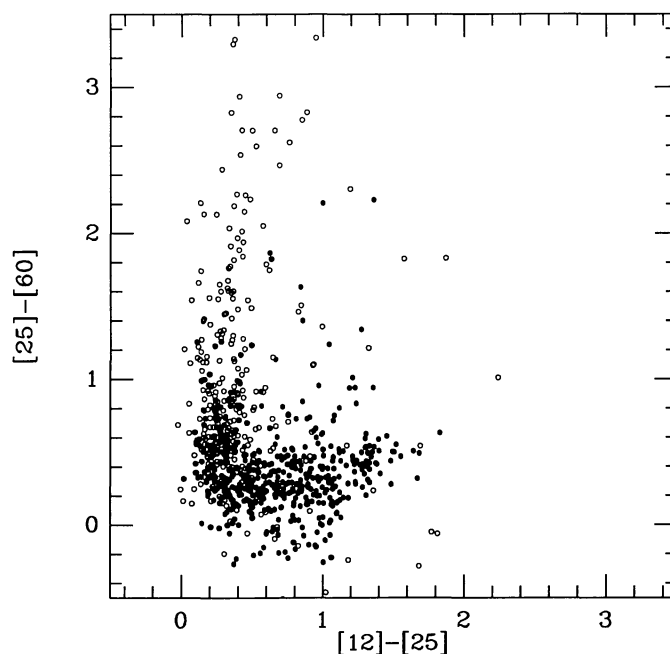


FIG. 15.—The observed *IRAS* colors for sources associated with carbon stars in the General Catalogue Of Cool Carbon Stars (Stephenson 1973), the “optical carbon stars” (open circles), and the *IRAS* sources with classes 40–49 LRS spectra, the “infrared carbon stars” (filled circles). These groups are not exclusive; however, the infrared carbon stars are redder in  $[12] - [25]$  than the optical carbon stars and the optical carbon stars often have  $60 \mu\text{m}$  excesses.

## A4. PARAMETERS OF THE MODELS

A set of radiative transfer models for AGB stars, both oxygen-rich, and carbon-rich, with dust shells of optical depths from  $\sim 0.1$  to  $\sim 30$  (at 9.7 or 11.3  $\mu\text{m}$ , depending upon the type of dust used) was run to produce a grid of model colors. Dust condensation temperatures of 1500, 1000, and 750 K were used in the models. Radiative transfer models for stars which have suffered an interruption of mass loss were provided by S. J. Chan for 12 different initial optical depths and some new, detached dust shell, radiative transfer models were run to extend the range of parameters to higher initial optical depths. These model colors were used to simulate the color evolution of AGB stars of different masses. The mass-loss rate and optical depth were assumed to be related by

$$\dot{M} = [0.00602 M_{\odot} \text{ yr}^{-1} \text{ pc}^{-1} (\text{km s}^{-1})^{-1}] \tau_{11.3\mu\text{m}} r_0 v, \quad (\text{A5})$$

$$\dot{M} = [0.00303 M_{\odot} \text{ yr}^{-1} \text{ pc}^{-1} (\text{km s}^{-1})^{-1}] \tau_{9.7\mu\text{m}} r_0 v, \quad (\text{A6})$$

for carbon dust and silicate dust, respectively (see Chan & Kwok 1988, eq. [12]) where  $r_0$  is the inner dust shell radius,  $v$  is the stellar wind velocity,  $\dot{M}$  is the stellar mass-loss rate, and  $\tau$  is the optical depth. The  $r_0$  value was assumed to be independent of the stellar temperature and proportional to  $\sqrt{L_{\star}}$ , and  $v$  was taken as 10  $\text{km s}^{-1}$  for all the model stars.

In the models, the AGB evolution was followed by numerical integration of the mass loss as a function of time, using a predictor-corrector method, and the colors were calculated at each time step. If the mass loss was interrupted, the star was followed through the detached shell phase until the mass loss resumed. A set of 200 stars with mass distribution randomly assigned, but consistent with a Salpeter initial mass function, was used. For any star with initial mass less than  $4 M_{\odot}$  there was a 60% chance that the star would become a carbon star over some fraction  $f_1$  of its AGB lifetime;  $f_1$  was a free parameter in the models, which affected the carbon star to oxygen-rich star ratio. The transition time was chosen at random within a time period

$$t_c = f_1 t_{\text{agb}} [1 - (M_{\text{ms}} - 1.25 M_{\odot}) / 2.75 M_{\odot}], \quad (\text{A7})$$

where  $t_{\text{agb}}$  is the nominal AGB lifetime for an oxygen-rich star of the same initial mass. The transition was assumed to occur later in more massive stars because a larger amount of carbon-rich material must be dredged up from the stellar core to transform the star into a carbon star.

At the time of transition, the mass loss was assumed to cease. After a period of time without mass loss, a new stellar wind was assumed to begin at a lower mass loss rate than that given by the Reimers formula with the set  $\eta$  value, and to build up exponentially to the full (Reimers) mass-loss rate over a set period. The models had free parameters for how long the mass loss is disrupted, how long the recovery of the mass-loss rate takes, and the time between the resumption of mass loss and the next disruption. These were the major free parameters used in looking for a fit to the *IRAS* observations.

The *IRAS* carbon stars have a wide range of infrared colors, so the sensitivity of *IRAS* to these stars is a function of the phase of evolution. The sample was required to have a 60  $\mu\text{m}$  observation so carbon stars with thick dust shells and redder colors are favored over the optical carbon stars. This is partially offset by the requirement of an LRS spectrum for the redder sources because sources had to be relatively bright to be accepted into the published set of LRS spectra. To allow for the different conditions for acceptance into the sample for sources with different colors, the model sources were assigned weights as a function of color. For each area of the color-color diagram, the model absolute magnitudes for the three *IRAS* bands were compared with the sample minimum flux densities. This comparison gave an estimate of the distance to which the stars could be observed in each wavelength band. The minimum of these three distances determined the limiting distance at which the model source would be observable. This distance was used to weight the model points. For model sources whose limiting distance was less than 1 kpc the weight was the square of the limiting distance. For sources that could be observed to greater distances, the weight was proportional to the distance. This weighting allows for the effects of incompleteness of the *IRAS* observations of distant sources near the Galactic plane. Confusion for LRS sources is a more serious problem than for the PSC sources because the *IRAS* scan direction on the sky was also the direction of LRS spectral dispersion.

## A5. RESULTS OF THE MODELS

Models were run for various combinations of mass-loss recovery and mass-loss disruption times. The best-fit model had the following parameters:

1. Silicate dust condensation temperature distribution: equally divided between 1500, 1000, and 750 K;
2. SiC dust condensation temperature distribution: 80% with 1500 K and 20% with 750 K;
3. Carbon star transition occurring at random in the last 10% of the oxygen-rich AGB lifetime, for 60% of all stars up to  $4.0 M_{\odot}$ ;
4. Dust mass-loss disruption time: until the shell reaches 8000 times the initial inner radius ( $\sim 4 \times 10^4$  yr);
5. Mass-loss recovery time: 1.24 times the period of no mass loss (exponential time constant 0.25 times the period of no mass loss);
6. Subsequent disruption of mass loss after 1.09 times the period of no mass loss.

These parameters, along with the colors from the models, gave a  $\chi^2$  fit to Figure 15 of 53, for 31 degrees of freedom, or 1.77 per bin, which is marginally acceptable. As well as calculating the weighted color distribution, the model program tabulated the relative



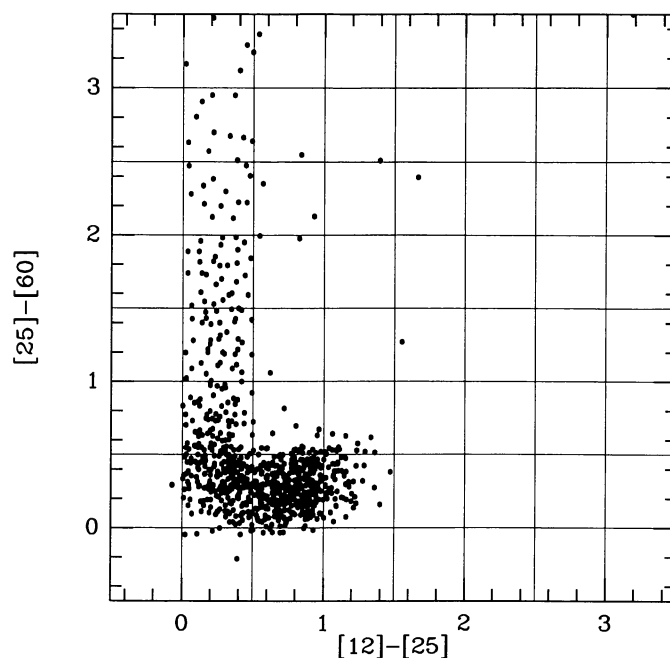


FIG. 16.—A subset of sources from the best-fit carbon star evolution model. The points were chosen at random from the full set of calculated points for comparison with Fig. 15. Each grid square was one element for the  $\chi^2$  fit.

luminosity function for the AGB sources, which was used to derive space density values by scaling to match the empirical  $12\ \mu\text{m}$  luminosity function determined from Monte Carlo simulations (Volk et al. 1992). Figure 16 shows a subset of the model points for comparison with Figure 15. The scatter of points near a particular color value is smaller in the models than in the actual data. The models lack the sources with  $[25] - [60] < 0$ . Radiative transfer models suggest that these sources could be stars with a particularly sudden increase in the mass-loss rate, producing a steeper density profile in the circumstellar shell than for steady mass loss, thereby reducing the  $60\ \mu\text{m}$  flux density because there is comparatively little dust at low temperatures.

The carbon stars in this model end up with higher core masses than a star of the same initial mass which stays oxygen rich because the periods of mass-loss disruption lengthen the AGB lifetime, so the core grows larger before the envelope is exhausted. Carbon stars in this model are generally more luminous than oxygen-rich stars of the same initial mass because the transition occurs late in the AGB lifetime and the core mass can become larger than the values used in Figure 14.

The model predicts intrinsic number ratios of 1.65:1:13.52 for optically visible carbon stars, infrared bright carbon stars, and oxygen-rich AGB stars, respectively. The overall carbon star to oxygen-rich AGB star ratio is predicted to be 1:5.1. The optical carbon stars are fairly common among AGB stars but, at least with *IRAS*, are observed only locally.

The model also predicts that generally carbon stars should have lower mass-loss rates than oxygen-rich stars of the same luminosity. This result is somewhat dependent upon the assumptions about the dust grain properties used to derive the constant in equation (A6). The fundamental result is that the dust shells of carbon stars in this model is generally of lower optical depth than for an equivalent oxygen-rich star, which appears to be generally consistent with the observations. In the models the carbon stars spend roughly the same amount of time as optical carbon stars and as infrared carbon stars.

The model program tabulates the relative numbers of carbon stars and oxygen-rich stars as a function of color. These values, unweighted, are proportional to the true space density values if the model is correct. There is a question of uniqueness in the model, especially given the number of assumptions required. Where possible, the  $V - [12]$  and  $K - [12]$  colors were obtained from the literature while the model  $M_{12}$  values were adopted for the table of sources. The model also yields values for the magnitude dispersion,  $\sigma$ , as a function of color. The overall space density of AGB stars was set by scaling the contribution to the luminosity function until a match to the empirical luminosity function of Volk et al. (1992) was obtained.

#### REFERENCES

- Acker, A., Marcout, J., & Ochsenbein, F. 1981, *A&AS*, 43, 265  
 Allen, C. W. 1973, *Astrophysical Quantities* (3d ed.; London: Athlone)  
 Bahcall, J. N. 1986, *ARA&A*, 24, 577  
 Bahcall, J. N., Ratnatunga, K. U., Buser, R., Fenkart, R. P., & Spaenhauer, A. 1985, *ApJ*, 299, 616  
 Bahcall, J. N., & Soneira, R. M. 1980, *ApJS*, 44, 73  
 ———. 1984, *ApJS*, 55, 67  
 Barlow, M. J., & Cohen, M. 1977, *ApJ*, 213, 737  
 Becker, W., & Fenkart, R. 1970, in *IAU Symp. 38, The Spiral Structure of Our Galaxy*, ed. W. Becker & G. Contopoulos (Dordrecht: Reidel), 205  
 Blaauw, A. 1963, in *Basic Astronomical Data*, ed. K. Aa. Strand (Univ. of Chicago Press), 383  
 ———. 1985, in *IAU Symp. 106, The Milky Way Galaxy*, ed. H. van Woerden, R. J. Allen, & W. B. Burton (Dordrecht: Reidel), 335  
 Boothroyd, A. I., & Sackmann, I.-J. 1988a, *ApJ*, 328, 632  
 ———. 1988b, *ApJ*, 328, 641

- Boothroyd, A. I., & Sackman, I.-J. 1988c, *ApJ*, 328, 653  
 ———. 1988d, *ApJ*, 328, 671  
 Buta, R. 1986, *ApJS*, 61, 609  
 ———. 1987, *ApJS*, 64, 1  
 Carney, B. W., Latham, D. W., & Laird, J. B. 1989, *AJ*, 97, 423  
 Catchpole, R. M., Whitelock, P. A., & Glass, I. S. 1990, *MNRAS*, 247, 479  
 Chan, S. J., & Kwok, S. 1988, *ApJ*, 334, 362  
 Chokshi, A., & Wright, E. L. 1988, *ApJ*, 333, 491  
 Claussen, M. J., Kleinmann, S. G., Joyce, R. R., & Jura, M. 1987, *ApJS*, 65, 385  
 Clemens, D. P., Sanders, D. B., & Scoville, N. Z. 1988, *ApJ*, 327, 139  
 Cohen, M. 1992, *AJ*, 103, 1734  
 Cohen, M., Emerson, J. P., & Beichman, C. A. 1989a, *ApJ*, 339, 455  
 Cohen, M., & Kuhi, L. V. 1976, *PASP*, 88, 535  
 ———. 1977, *PASP*, 89, 829  
 ———. 1979, *ApJS*, 41, 743  
 Cohen, M., Schwartz, D. E., Chokshi, A., & Walker, R. G. 1987, *AJ*, 93, 1199  
 Cohen, M., & Volk, K. 1989, *AJ*, 98, 1563  
 Cohen, M., Wainscoat, R. J., Walker, H. J., Volk, K., & Schwartz, D. E. 1989b, *AJ*, 97, 1759  
 Cohen, M., Walker, R., Wainscoat, R., Volk, K., Walker, H., & Schwartz, D. 1990, *An Infrared Sky Model Based on the IRAS Point Source Data*, NASA CR-177526  
 Cohen, M., & Witteborn, F. C. 1985, *ApJ*, 294, 345  
 Cohen, R. S., Cong, H., Dame, T. M., & Thaddeus, P. 1980, *ApJ*, 239, L53  
 Cruz-Gonzalez, C., Recillas-Cruz, E., Costero, R., Peimbert, M., & Torres-Peimbert, S. 1974, *Rev. Mexicana Astron. Af.*, 1, 211  
 Dame, T. M., Ungerechts, H., Cohen, R. S., de Geus, E. J., Grenier, I. A., May, J., Murphy, D. C., Nyman, L.-Å., & Thaddeus, P. 1987, *ApJ*, 327, 706  
 de la Reza, R., Torres, C. A. O., Quast, G., Castilho, B. V., & Vieira, G. L. 1989, *ApJ*, 343, L61  
 de Vaucouleurs, G. 1959, in *Handbuch der Physik*, Vol. 53, ed. S. Flügge (Berlin: Springer), 311  
 ———. 1977, *AJ*, 82, 456  
 de Vaucouleurs, G., & Buta, R. J. 1978, *AJ*, 83, 1383  
 de Vaucouleurs, G., & Pence, W. 1978, *AJ*, 83, 1163  
 Djorgovski, S., & Sosin, C. 1989, *ApJ*, 341, L13  
 Eaton, N., Adams, D. J., & Giles, A. B. 1984, *MNRAS*, 208, 241  
 Elias, J. H. 1978a, *ApJ*, 223, 859  
 ———. 1978b, *AJ*, 83, 791  
 Elmegreen, D. M. 1985, in *IAU Symp. 106, The Milky Way Galaxy*, ed. H. van Woerden, R. J. Allen, & W. B. Burton (Dordrecht: Reidel), 255  
 Fenkart, R. 1989a, *A&AS*, 78, 217  
 ———. 1989b, *A&AS*, 79, 51  
 ———. 1989c, *A&AS*, 80, 89  
 ———. 1989d, *A&AS*, 81, 187  
 Forrest, W. J., Gillett, F. C., & Stein, W. A. 1975, *ApJ*, 195, 423  
 Freeman, K. C. 1970, *ApJ*, 160, 811  
 Garwood, R., & Jones, T. J. 1987, *PASP*, 99, 453  
 Gathier, R. 1984, Ph.D. thesis, University of Groningen  
 Georgelin, Y. M., & Georgelin, Y. P. 1976, *A&A*, 49, 57  
 Gezari, D. Y., Schmitz, M., & Mead, J. M. 1987, *Catalog of Infrared Observations*, NASA RP-1196  
 Gilmore, G., & Reid, N. 1983, *MNRAS*, 202, 1025  
 Gilmore, G., Wyse, R. F. G., & Kuijken, K. 1989, *ARA&A*, 27, 555  
 Habing, H. 1986, in *Light on Dark Matter*, ed. F. P. Israel (Dordrecht: Reidel), 329  
 ———. 1988, *A&A*, 200, 40  
 Hacking, P., Condon, J. J., & Houck, J. R. 1987, *ApJ*, 316, L15  
 Hacking, P., & Houck, J. R. 1987, *ApJS*, 63, 311  
 Hacking, P., et al. 1985, *PASP*, 97, 616  
 Herbig, G. H., & Bell, K. R. 1988, *Lick Obs. Bull.*, No. 1111  
 Herbst, W. 1975, *AJ*, 80, 212  
 Hoffleit, D., & Jaschek, C. 1982, *The Bright Star Catalogue*, 4th revised ed. (New Haven: Yale Univ. Obs.) (BSC)  
 Iben, I., Jr., 1965, *ApJ*, 141, 993  
 Iben, I., Jr., & Renzini, A. 1983, *ARA&A*, 21, 271  
*IRAS Catalogs and Atlases*, Vol. 1, Explanatory Supplement. 1988, ed. C. A. Beichman, G. Neugebauer, H. J. Habing, P. E. Clegg, & T. J. Chester (Washington, DC: GPO)  
*IRAS Catalogs and Atlases*, Vols. 2–6, The Point Source Catalog. 1988, Joint *IRAS* Science Working Group (Washington, DC: GPO) (PSC)  
*IRAS Catalogs and Atlases*, Vol. 7, The Small-Scale Structure Catalog. 1988, ed. G. Helou, & D. W. Walker (Washington, DC: GPO)  
*IRAS Science Team*. 1986, *A&AS*, 65, 607 (*IRAS Catalogs and Atlases*, Atlas of Low-Resolution Spectra) (The Atlas)  
 Jackson, J. M., Snell, R. L., Ho, P. T. P., & Barrett, A. H. 1989, *ApJ*, 337, 680  
 Johnson, H. L. 1966, *ARA&A*, 4, 193  
 Jones, B. F., & Herbig, G. H. 1979, *AJ*, 84, 1872  
 Jones, T. J., Ashley, M., Hyland, A. R., & Ruelas-Mayorga, A. 1981, *MNRAS*, 197, 413  
 Kawara, K., Kozasa, T., Sato, S., Kobayashi, Y., Okuda, H., & Jugaku, J. 1982, *PASJ*, 34, 389  
 Keenan, P. 1963, in *Basic Astronomical Data*, ed. K. Aa. Strand (Univers. of Chicago Press), 78  
 Kent, S. M., Dame, T. M., & Fazio, G. 1991, *ApJ*, 378, 131  
 Kerr, F. J., & Westerhout, G. 1965, in *Galactic Structure*, ed. A. Blaauw & M. Schmidt (Univers. of Chicago Press), 167  
 Kleinmann, S. G., Cutri, R. M., Young, E. T., Low, F. J., & Gillett, F. C. 1986, *Explanatory Supplement to the IRAS Serendipitous Survey Catalog*, (Pasadena: JPL) (SSC)  
 Kleinmann, S. G., Hamilton, D., Keel, W. C., Wynn-Williams, C. G., Eales, S. A., Becklin, E. E., & Kuntz, K. D. 1988, *ApJ*, 328, 161  
 Koornneef, J. 1983, *A&A*, 128, 84  
 Kormendy, J. 1977, *ApJ*, 217, 406  
 Kukarkin, B. V., et al. 1970, *General Catalogue of Variable Stars* (Moscow: Nauka) (GCVS)  
 Lawrence, A., Walker, D., Rowan-Robinson, M., Leech, K. J., & Penston, M. V. 1986, *MNRAS*, 219, 687  
 Leitherer, C., Bertout, C., Stahl, O., & Wolf, B. 1984, *A&A*, 140, 199  
 Lewis, J. R., & Freeman, K. C. 1989, *AJ*, 97, 139  
 Maihara, T., Oda, N., Sugiyama, T., & Okuda, H. 1978, *PASJ*, 30, 1  
 Mamon, G. A., & Soneira, R. M. 1982, *ApJ*, 255, 181  
 Mikami, T., & Ishida, K. 1981, *PASJ*, 33, 135  
 Mikami, T., Ishida, K., Hamajima, K., & Kawara, K. 1982, *PASJ*, 34, 223  
 Miley, G. K., Neugebauer, G., & Soifer, B. T. 1985, *ApJ*, 293, L11  
 Moshir, M., et al. 1989, *Explanatory Supplement to the IRAS Faint Source Survey* (Pasadena: JPL) (FSS)  
 Neugebauer, G., Miley, G. K., Soifer, B. T., & Clegg, P. E. 1986, *ApJ*, 308, 815  
 Neugebauer, G., & Leighton, R. B. 1969, *Two Micron Sky Survey*, NASA SP-3047 (TMSS)  
 Okuda, H. 1981, in *IAU Symp. 96, Infrared Astronomy*, ed. C. G. Wynn-Williams, & D. L. Cruikshank (Dordrecht: Reidel), 247  
 Price, S. D., & Walker, R. G. 1976, *The AFGL Four-Color Infrared Sky Survey: Catalog of Observations at 4.2, 11.0, 19.8, and 27.4 Microns*, AFGL-TR-76-0208  
 Reifenstein, E. C., Wilson, T. L., Burke, B. F., Mezger, P. G., & Altenhoff, W. J. 1970, *A&A*, 4, 357  
 Reimers, D. 1977, *A&A*, 61, 217  
 Rice, W., Lonsdale, C. J., Soifer, B. T., Neugebauer, G., Kopan, E. L., Lloyd, L. A., de Jong, T., & Habing, H. J. 1988, *ApJS*, 68, 91  
 Rieke, G. H., & Lebofsky, M. J. 1985, *ApJ*, 288, 618 (RL)  
 Roche, P. F. 1989, in *Proc. 22d ESLAB Symp. Infrared Spectroscopy in Astronomy*, ed. M. F. Kessler & A. Glasse (Dordrecht: Kluwer)  
 Rucinski, S. M., & Krautter, J. 1983, *A&A*, 121, 217  
 Ruelas-Mayorga, R. A. 1986, Ph.D. thesis, Australian National University  
 Rydgren, A. E., Schmelz, J. T., Zak, D. S., & Vrba, F. J. 1984, *Publ. USNO*, XXV, Pt. I  
 Sanders, R. H., & Lowinger, T. 1972, *AJ*, 77, 292  
 Seiden, P. E., Schulman, L. S., & Elmegreen, B. G. 1984, *ApJ*, 282, 95  
 Smithsonian Astrophysical Observatory 1966, *Smithsonian Astrophysical Observatory Star Catalog*, (Washington, DC: Smithsonian Institution) (SAOC)  
 Soifer, B. T., Sanders, D. B., Madore, B. F., Neugebauer, G., Danielson, G. E., Elias, J. H., Lonsdale, C. J., & Rice, W. L. 1987, *ApJ*, 320, 238  
 Stephenson, C. B. 1973, *Publ. Warner & Swasey Obs.*, 1, No. 4  
 Strauss, M. A., & Davis, M. 1988, in *IAU Symp. 130, Large-Scale Structure of the Universe*, ed. J. Adouze et al. (Dordrecht: Reidel), 191  
 van den Bergh, S. 1966, *AJ*, 71, 990  
 van den Bergh, S., & Herbst, W. 1975, *AJ*, 80, 208

- van der Kruit, P. C., & Searle, L. 1981a, A&A, 95, 105  
———. 1981b, A&A, 95, 116  
———. 1982, A&A, 110, 61  
———. 1986, A&A, 157, 230  
Volk, K., & Cohen, M. 1989, AJ, 98, 1918  
———. 1990, AJ, 100, 485  
Volk, K., Wainscoat, R. J., Cohen, M., Walker, H. J., & Schwartz, D. E. 1992, AJ, submitted  
Wainscoat, R. J. 1992, in preparation  
Wainscoat, R. J., Freeman, K. C., & Hyland, A. R. 1989, ApJ, 337, 163  
Walker, H. J., & Cohen, M. 1988, AJ, 95, 1801  
Walker, H. J., Cohen, M., Volk, K., Wainscoat, R. J., & Schwartz, D. E. 1989, AJ, 98, 2163  
Walterbos, R. A. M. 1986, Ph.D. thesis, University of Leiden  
Weaver, H. 1974, in *Highlights Astron.*, 3, 423  
———. 1989, private communication  
Weidemann, V. 1984, A&A, 143, L1  
Weidemann, V., & Koester, D. 1983, A&A, 121, 77  
Whitelock, P. A. 1985, MNRAS, 213, 59  
Willems, F. 1987, Ph.D. thesis, University of Amsterdam  
Wilson, T. L., Mezger, P. G., Gardner, F. F., & Milne, D. K. 1970, A&A, 6, 364  
Wolf B., & Stahl, O. 1985, A&A, 148, 412  
Wood, P. R., & Cahn, J. H. 1977, ApJ, 211, 499  
Zuckerman, B., & Aller, L. H. 1986, ApJ, 301, 772